# Integrated free radical sensor systems for the investigation of cellular models of disease

SarahJayne Boulton

BSc. (hons)

January 2010

Thesis submitted for the degree of Doctor of Philosophy in the institute of Cellular Medicine, Newcastle University

# i. Abstract

Reactive oxygen species (ROS) including superoxide ($O_2^{\bar{}}$), nitric oxide ($NO^{\bullet}$) and hydrogen peroxide ($H_2O_2$) are thought to play a central role in many disease processes. This thesis details the development of novel optical and electrochemical sensor platforms for the analysis of ROS. These technologies were established in response to the current limitations of existing techniques to enable greater understanding of the role of ROS in cellular pathology.

The overproduction of $O_2^{\bar{}}$ by mitochondria has been linked to the initiation of disease processes. Specifically, defects in the mitochondrial electron transport chain (mETC) can result in electron leakage and subsequent ROS generation. Using a gold electrode, surface-modified with cytochrome *c*, the amperometric detection of real-time $O_2^{\bar{}}$ production from isolated mitochondria was enabled. Specific transport proteins within the mETC were chemically inhibited and the change in $O_2^{\bar{}}$ flux was observed, allowing the contribution to ROS production of inhibition of mETC Complex I and Complex III to be observed.

ROS-sensitive nanosensors, based on the entrapment of the fluorophore dihydrorhodamine-123 (DHR123) in a porous polyacrylamide shell, were developed. These sensors were successfully introduced into the macrophage cell line NR8383, which facilitated the analysis of intracellular ROS fluctuations following stimulation with phorbol-12-myristate 13-acetate (PMA). Nanosensors containing the pH responsive fluorophore fluorescein isothiocyanate (FITC) were also used to measure intracellular pH ($pH_i$) in primary myoblasts derived from patients with Chronic Fatigue Syndrome (CFS). These sensors have provided new insight into the role of intracellular acidosis in this disease.

Intracellular ROS-sensitive nanosensor technology was combined with custom fabricated gold microelectrode arrays to produce a novel integrated cell monitoring platform capable of reporting real-time ROS flux in both the intra- and extracellular environment. Rat macrophage cells loaded with ROS-sensitive nanosensors were seeded into wells containing functionalised, ROS-responsive, gold ring electrodes. Following stimulation of the cells with PMA it was possible to measure intracellular ROS generation using fluorescence spectroscopy. External ROS flux as a consequence of PMA stimulation was simultaneously measured amperometrically.

# ii. Declaration

The work in this thesis was carried out in the Diagnostic and Therapeutic Technologies research unit of the Institute of Cellular Medicine, Newcastle University between October 2008 and October 2011. Unless acknowledged by reference, all of the work reported is original.

No part of this work has been submitted for a degree, diploma or other qualification at this University.

# iii. Acknowledgements

I would firstly like to thank my supervisors Prof. Calum McNeil and Dr Philip Manning for their continued support and mentorship over the past 3 years. You were always on hand with the red pen and some good advice, and I am eternally grateful for the guidance you've both given me. Many thanks also to the debonair and benevolent members of the Diagnostic and Therapeutic Technologies Research Group past and present without whom I would have floundered substantially, never had endured a fat-ball class and consumed far less than my glutton's share of coffee.

I am thankful to have worked with so many inspirational people within the University who, without fail, have always found time to sit down and discuss the finer points of muscle gyms, climbing, holiday skincare and snowshoeing as well as bestowing their mountainous technical knowledge upon me. I am grateful to each and every one of you.

To my friends, especially to Pennington, Jack Block, Dr. Wright, Callum and Rhona, I express my heartfelt gratitude for providing an exquisite soundtrack to this work and reminding me that there is life beyond science.

Huge love and stuff to my Mammy, for my life before science.

And finally, thank you Rory for making the good stuff better, the bad stuff matter less and for being the one that's right next to me when it all kicks off. Now let's go find ourselves a rain void.

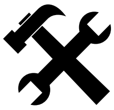

This thesis is dedicated to the memory of my Pa;
the first to show me just how much could be accomplished
with a roll of gaffer tape,
some 2-part epoxy
and a decent first aid kit.

# iv. Table of Contents

# v. List of Figures and Tables

*Figures:*

*Tables:*

# vi. List of Abbreviations

| | |
|---|---|
| ALS | Amylotrophic lateral sclerosis |
| ATP | Adenosine triphosphate |
| CFS | Chronic Fatigue Syndrome |
| CM | Complete medium |
| CNS | Central nervous system |
| CoQ | Coenzyme Q (also called ‘ubiquinone’) |
| CV | Cyclic voltammetry |
| DA | Dopamine |
| DAF-FM | 4-Amino-5-methylamino-2,7-difluorofluorescein |
| DAT | Dopamine transporter |
| DCA | Dichloroacetate |
| DCF-DA | Dichlorodihydrofluorescein diacetate |
| DHE | Dihydroethidium |
| DHR123 | Dihydrorhodamine-123 |
| DMEM | Dulbecco’s modified Eagle’s medium |
| DNA | Deoxyribonucleic acid |
| DTSSP | 3,3'-Dithiobis(sulphosuccinimidyl)propionate |
| FACS | Fluorescence assisted cell sorting |
| $FADH_2$ | Flavin adenine dinucleotide phosphate |
| FCS | Foetal calf serum |
| FI | Fluorescence intensity |
| FITC | Fluorescein isothiocyanate |
| FMN | Flavin mononucleotide |
| fMRI | Functional Magnetic Resonance Spectroscopy |
| GFP | Green fluorescent protein |
| HD | Huntington’s disease |
| mETC | Mitochondrial electron transport chain |
| MRS | Magnetic Resonance Spectroscopy |
| mtDNA | Mitochondrial deoxyribonucleic acid |

| | |
|---|---|
| NADPH | Nicotinamide adenine dinucleotide phosphate |
| $NO^{\bullet}$ | Nitric oxide |
| $O_2^-$ | Superoxide |
| PBS | Phosphate buffered saline |
| PD | Parkinson’s disease |
| PDC | Pyruvate dyhydrogenase complex |
| PDK | Pyruvate dehydrogenase kinase |
| PEBBLE | Probes encapsulated by biologically localised embedding |
| PI | Propidium iodide |
| PKC | Protein Kinase C |
| PM | Plain medium |
| PMA | Phorbol 12-myristate-13-acetate |
| R123 | Rhodamine-123 |
| ROS | Reactive oxygen species |
| SOD | Superoxide dismutase |
| TaClo | 1-Trichloromethyl-1,2,3,4-tetrahydro-beta-carboline |
| TCA | Tricarboxylic acid |
| UVA | Ultraviolet A radiation (300-420nm) |
| UVR | Ultraviolet radiation |
| XOD | Xanthine oxidase |
| YFP | Yellow fluorescent protein |

# Chapter 1. General Introduction

## 1.1 Reactive oxygen and nitrogen species in biological systems

Reactive oxygen species (ROS) have long been the subject of many investigations, due to their prominent involvement in a variety of high profile disease states including but not limited to melanoma, Parkinson's disease, Alzheimer's disease, amyotrophic lateral sclerosis (Cookson *et al*. 2002), diabetes mellitus and cardiomyopathies (Awad *et al*. 2010). Although most research concerning ROS has focused heavily upon the molecules' ability to cause cell harm, ROS are unavoidable products of normal cell metabolism generally through spontaneous or enzyme mediated electron transfer reactions (Cheeseman and Slater 1993). The progression of disease states as a result of oxidative cell harm only occurs only when a cell's antioxidant capacity becomes overwhelmed or fails (Van Lente 1993). ROS are important cell signalling molecules with several distinguished roles including pathogen detoxification (Carsillo *et al*. 2009), apoptosis (Hartley *et al*. 1994; Langer *et al*. 2008), signal mediation (Newland *et al*. 2008; Sarti *et al*. 2002) and proliferation (Oh *et al*. 2008). ROS such as superoxide ($O_2^-$), nitric oxide ($NO^\bullet$) and hydrogen peroxide ($H_2O_2$) have been most frequently investigated as their uncontrolled production can lead to a wide range of pathologies such as ischemia (Hallstrom *et al*. 2008; Urakami *et al*. 2007), muscular dysfunction (Gillespie *et al*. 2004; Massion *et al*. 2005; Ozgocmen *et al*. 2006) atherosclerosis (Liu *et al*. 2009) and migraine (Read *et al*. 1999). Conversely, ROS have also been cited as conferring neuroprotection (Di Matteo *et al*. 2009; Kurauchi *et al*. 2009). The need for more specific and dynamic monitoring tools for different ROS has become apparent as the varied roles for these molecules have emerged.

## 1.2 Mechanisms of reactive oxygen species generation

The generation of ROS has been purported as an unavoidable consequence of aerobic metabolism (Halliwell 1991). ROS are specifically produced as signalling molecules and are reported to play important roles in signal transduction (Yin *et al*. 2010) as well as being known to cause massive cellular damage when overproduced as a consequence of disease or prior cell distress (Birch-Machin 2006). This section introduces three major ROS producing factors that are of huge importance to this project.

### 1.2.1 Ultraviolet radiation

Oxidative damage by ultraviolet radiation (UVR) has been extensively investigated both *in vivo* (Fisher *et al*. 2009) and *in vitro* (Aitken *et al*. 2007; Mahns *et al*. 2003), with many different pathways to ROS generation and interactions elucidated, that are induced by exposure. Some endogenous intracellular photosensitive chemicals have been shown to generate $O_2^-$ by reducing molecular oxygen with high energy electrons propagated by UVR (Baier *et al*. 2006). Both urocainic acid (Menon and Morrison 2002) and riboflavin (Mahns *et al*. 2003) were reported to absorb energy in the form of incident radiation whilst in their low energy ground state. Once in a high energy excited state the chemical became unstable, and released energy to nearby acceptors upon returning to a more stable ground state (Baier *et al*. 2006). The formation of the $O_2^-$ radical occurred when energy was discharged by the transfer of an electron to $O_2$ (Wondrak *et al*. 2006). It is known that $O_2^-$ will react with $NO^\bullet$ to form the peroxynitrite ion ($ONOO^-$) (Kourie 1998; Patel *et al*. 2000), undergo dismutation to $H_2O_2$ catalysed by superoxide dismutase (SOD) (Craig *et al*. 2009). SOD has the highest efficacy for $O_2^-$ of any enzyme for its substrate. The resultant high dismutation rate constant is reported to outcompete the ability of $O_2^-$ to interact with other biomolecules, thus limiting the cellular damage $O_2^-$ can cause directly.

### 1.2.2 NADPH oxidase and protein kinase C

Reduced nicotinamide adenine dinucleotide phosphate (NADPH) oxidase is a complex enzyme found in plasma membranes of many types of mammalian cells, although it is most commonly described in professional phagocytic cells where the complex plays an important role in host pathogen interaction (Babior 2004). NADPH oxidase is a complex membrane associated enzyme consisting of either a rac 1 or rac 2 G-protein, two membrane bound proteins and three cytosolic components (Babior 1999). NADPH oxidase is reported to generate $O_2^-$ extracellularly by feeding high energy electrons removed from NAPDH through the plasma membrane (Babior 2004). Upon initiation of phagocytosis, an oxygen-dependent degradation process of the ingested matter can be triggered which relies heavily on the production of $O_2^-$. Stimulation of protein kinase C (PKC) on macrophage cells with phorbol-12-myristate-13-acetate (PMA) initiates the assembly of the cytosolic components of NADPH oxidase which then translocate to the cell membrane and assemble with the membrane embedded g-protein components, induce phagocytosis and triggering the associated 'superoxide burst' (Henderson 2009). PKC-stimulated $O_2^-$ production has been exploited throughout this project to induce $O_2^-$ flux from monitored rat alveolar macrophage cell line NR8383, and is more fully described in Chapters 4 and 7.

### 1.2.3 Mitochondrial dysfunction

There are many routes described by which the mitochondrial electron transport chain (mETC) generates $O_2^-$ (Birch-Machin 2006). The mitochondria are a major site of $O_2^-$ production within eukaryotic cells. The high turnover and spatial density of reduction reactions involved in ATP generation inevitably leads to the leakage of high energy electrons from the different enzymatic complexes of the mETC, both to the interior and exterior of the mitochondrial membrane. The generation of $O_2^-$ by Complexes I and III of the mETC is discussed more fully in Chapters 5 and 6. Briefly, NADH and $FADH_2$ from the tricarboxylic acid cycle (TCA) are coenzymes for electron transport through the mETC. The movement of electrons and sites of $O_2^-$ generation are summarised in Figure 1.1.

NADH feeds electrons into the chain only through the NADH:ubiquinone reductase (Complex I). This enzyme couples the reduction of NADH to the oxidation of a flavin mononucleotide (FMN), simultaneously driving the translocation of protons from the matrix across the inner membrane to the inter-membranal space. Electrons then pass from FMN to redox active iron-sulphur (Fe-S) proteins before being used to reduce Coenzyme Q (CoQ, also known as 'ubiquinone'). Electron transfer from $FADH_2$ to CoQ is catalysed by succinate dehydrogenase (Complex II). CoQ is a lipid soluble electron transporter that freely diffuses through the inner membrane, shuttling electrons from

Complexes I and II to Complex III. Complex I has been identified as a major site of $O_2^{-}$ generation, with electron leaks reported as originating from the reduction of CoQ by the Fe-S protein cluster (Genova *et al*. 2001; Herrero and Barja 1997; Lambert and Brand 2004).

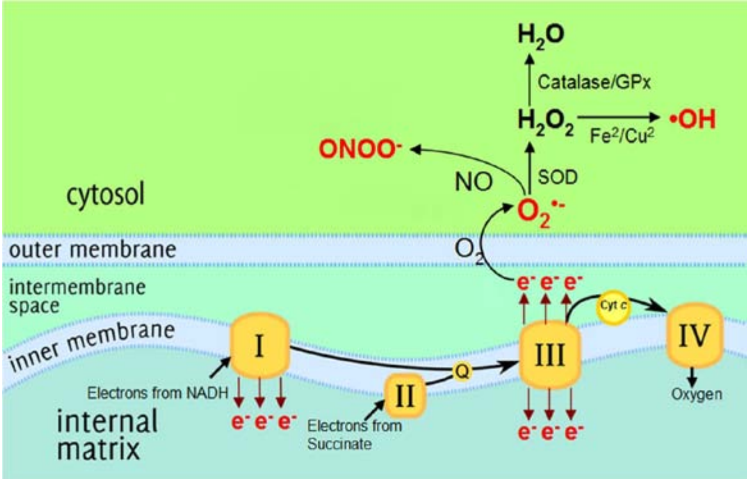

**Figure 1.1:** Both Complex I and III have been recognised as major sites of electron leakage and subsequent $O_2^{-}$ generation. $O_2^{-}$ that reaches the cytosol can further react with $NO^{\bullet}$ and redox capable metal ions to form new ROS such as $H_2O_2$ and $OONO^{-}$.

Complex II accepts electrons transferred from both Complexes I and II and is reported as being extremely active in terms of $O_2^{-}$ generation (Han *et al*. 2001; Henderson 2009; Muller *et al*. 2004; Zmijewski *et al*. 2009) CoQ binds to the cytochrome $bc_1$ Complex (Complex III) to progress electrons from Complexes I and II though the mETC. This site, due to the high turnover of reduction reactions occurring, has been identified as the major point of electron leakage from Complex III (Lambert and Brand 2004).

## 1.3 Reactive oxygen species in human disease

### 1.3.1 Dermatological disease states

By providing an effective protective boundary and interface between a body's internal organs and the external environment, the skin is constantly exposed to a range of damaging chemical and physical stimuli. UVR exposure is known to cause an array of cytotoxic effects in skin cells including DNA strand breaks (Aitken *et al*. 2007), mutagenesis (Petersen *et al*. 2000) and disruption of protein-DNA interaction (Aitken *et al*. 2007; Maresca *et al*. 2008; Petersen *et al*. 2000; Sachi *et al*. 1995). One 3895 base pair mitochondrial DNA (mtDNA) deletion is reported as so common in sun damaged skin it can be used as a marker of solar overexposure (Krishnan *et al*. 2004). Strand break damage to mtDNA has been most regularly attributed to the action of $H_2O_2$ (Macdonald *et al*, 1993). Strand break damage, cumulative mutations and the deficiency of repair pathways for mtDNA formed the basis of the 'defective powerhouse model' of dermatological photo-ageing (Krutmann and Schroeder, 2009), which attempted to reconcile corroborating current literature into a cohesive theory of mitochondrial involvement in premature skin aging and the progression of age related skin diseases (Berneburg *et al*. 2004; Krutmann, 2000; Krutmann and Schroeder 2009). Based on the well established understanding that mtDNA accumulates mutations with age, the model suggested that UVR, in particular the deeper penetrating ultraviolet A radiation (UVA, $_{\lambda}$300-420nm), was a major cause of large scale mtDNA deletions and strand breaks associated with gene mutation. This in turn was linked to progressive reductions in mitochondrial efficiency. This chronic result of long-term over-production of ROS has been shown to exacerbate oxidative cell harm (Birch-Machin and Swalwell 2010). As mutations accumulated in the mtDNA, the incidence of key metabolic protein deficiency and mis-folding increased (Mott *et al*. 2005; Wei and Lee 2002). As electron transport became progressively more disrupted due to mETC leakage and uncoupling, the more $O_2^-$ was generated as a result of spontaneous reduction of $O_2^-$ (Wei and Lee 2002). The real-time monitoring of $O_2^-$ from isolated mitochondria as a result of mETC inhibition has been reported (Henderson 2009) and is discussed fully in Chapters 5 and 6 of this thesis.

### 1.3.2 Neurodegenerative disorders

One of the defining characteristics of Parkinson's disease (PD) is a loss of dopaminergic neurons in the *substantia nigra pars compacta* (Rinne *et al*. 1989). Neurones in this area of the brain do not proliferate, and as a consequence, damage sustained by the cells is cumulative (Zeng *et al*. 2006) Spontaneous auto-oxidation of the catecholamine and neurotransmitter dopamine (DA) both intra and extracellularly is known to generate ROS and has been shown to cause substantial cell death in populations exposed to high DA concentrations (Masserano *et al*. 1996; McLaughlin *et al*. 1998). DA is also metabolised intracellularly by monoamine oxidase (MAO), which has been shown to result in the intermediate generation of $H_2O_2$ and other downstream ROS (Fahn and Cohen 1992). MAO activity in the midbrain is known to increase with age. This is indicative of increased DA oxidation, resulting in reduced concentrations of DA in the midbrain and inherently leading to increased oxidative cell damage and progression of neurological pathologies (Nicotra *et al*. 2004).

Oxidative damage intracellularly in the *nigra stratum* caused by the dysfunction of the mitochondria is thought to be another route to the development of PD (Lin and Beal 2006). Many mitochondria linked proteins have been shown to contribute to the regulation of cell death and proliferation (Danial and Korsmeyer 2004). Disruption of these proteins and their signalling pathways has been shown to be a causal factor in PD, amyotrophic lateral sclerosis (ALS), Huntington's disease (HD) and Alzheimer's disease (AD) (Lin and Beal 2006). Inhibition of the mETC leads to an increase in electron leakage at the point of blockage the result of which has been demonstrated as an increase in $O_2^{-}$ flux from the mitochondria (Henderson 2009). Long term exposure to exogenous chemicals and their metabolites capable of increasing oxidative damage to the mtDNA such as 1-trichloromethyl-1,2,3,4-tetrahydro-beta-carboline (TaClo) (Bringmann *et al*. 1995) have been linked to aging and the exacerbation of age related disease (Bringmann *et al*. 1996). This is discussed as being related to the accumulation of mtDNA mutations and the increase in mistranslation of genes and eventually proteins leading to cell death and disease progression (Corral-Debrinski *et al*. 1992). Coupled to the previously discussed fact that dopaminergic neurons do not divide or proliferate, it is clear that such cells are prone to accumulated DNA damage through oxidative stress.

## 1.4 pH in disease states

### 1.4.1 Metabolic disorders

Due to heavy energy dependency, skeletal muscle tissue is evolved to exert tight control of cellular processes, including $pH_i$. Lactic acidosis is a key clinical symptom of many metabolic disorders and can be indicative of many different dysfunctions within the oxidative phosphorylation pathway (Mizock and Falk 1992). To briefly introduce oxidative glucose metabolism, glucose undergoes glycolysis to generate two pyruvate molecules per glucose molecule. Pyruvate is actively transported into the mitochondria and is immediately decarboxylised by pyruvate dehydrogenase complex (PDC) to produce acetyl coenzyme A. Acetyl coenzyme A is then fed in to the citric acid cycle and undergoes a series of oxidation reactions to produce NADH and $FADH_2$. These two cofactors generate one final molecule of ATP by driving electrons through the mETC through the maintenance of the mitochondrial proton gradient.

Fatigue and lactic acidosis are definitive symptoms in patients with metabolic disorders involving a deficiency of PDC function (Fouque *et al*. 2003). In healthy non-symptomatic patients, adequate oxygen perfusion allows almost all available pyruvate to be metabolised aerobically, resulting in a very low resting blood lactic acid concentration of 1-2 mM (Robergs *et al*. 2004). As a result of reduced PDC function pyruvate accumulates within the cells and is reduced by NADH to lactic acid. This regenerates NAD, which can be recycled through the glycolysis process to generate further pyruvate. Without reinstatement of PDC function, lactic acid accumulates in the myoblasts, reducing the pH and causing widespread disruption to pH- sensitive intracellular proteins. If left untreated lactic acidosis can be fatal (Robergs *et al*. 2004). PDC function is tightly controlled by pyruvate dehydrogenase kinase (PDK) and pyruvate dehydrogenase phosphatase, which are responsible for PDC inactivation and reactivation respectively. Once phosphorylated, PDC becomes inactive. Investigative treatments to alleviate lactic acidosis have focussed upon PDK as a potential therapeutic target. Dichloroacetate (DCA), an analogue of pyruvate, has been investigated *in vitro* as an inhibitor of PDK function (Fouque *et al*. 2003; Henderson *et al*. 1997). By inhibiting phosphorylation, PDC spent more time in an active conformation, allowing the clearance of accumulated lactic acid an an increase in $pH_i$. Unfortunately the long term toxicity issues surrounding DCA administration including liver failure and oncogenesis prevent the clinical implementation of a treatment regimen (Felitsyn *et al*. 2007; Stacpoole *et al*. 1979). This will be discussed in more detail in Chapter 4 which focuses on the application of pH sensitive nanosensors to disease state and normal cultured primary muscle for monitoring changes in the $pH_i$ in response to DCA.

## 1.5 Tools for real time intracellular monitoring

### 1.5.1 Established techniques for reactive oxygen species monitoring

There are vast arrays of protocols and commercially available kits that had been developed and produced to facilitate the investigation of intracellular ROS mediated effects. Such techniques include the commercially available catalase assay, the reduced glutathione assay, strand break quantification through conformational analysis of supercoiled DNA (Srinivasan *et al*. 2001) or agarose gel electrophoresis (Laurent *et al*. 2005). Proteins reported to sustain ROS induced damage have been investigated using immunoprecipition and western blotting (Rinna *et al*. 2006). These tools have been used to provide insight regarding the effects of proposed ROS inducing treatments, allowing endpoint assessment of increasing peroxidation (Cheeseman 1993), reduction or up-regulation of antioxidant protein as a consequence of an altered internal oxidative state. Endpoint testing does not monitor ROS generation or flux directly and as such gave an incomplete representation of the mode and timescale of ROS production.

Many fluorescent dyes have been designed for the detection of ROS (Soh and Soh 2006) and have given detailed insight regarding the temporal and spatial characteristics of these molecules. These dyes have been employed in conjunction with a variety of fluorescence monitoring methods including fluorescence microscopy, confocal microscopy, fluorimetry, and FACS analysis. Multiple fluorescent probes have been employed simultaneously to provide independent corroboration of each individual dye's data sets (Deng *et al*. 2008). MitoTracker Orange, 4-amino-5-methylamino-2,7-difluorofluorescein (DAF-FM) and Dihydroethidium (DHE) dyes were developed to selectively interact with ROS intracellularly. The MitoTracker range of dyes was developed to localize to the mitochondria using engineered inherent zeta charge properties. DAF-FM has been marketed as a sensor specifically for $NO^{\bullet}$, however it has been suggested that the dye's specificity is not absolute (Balcerczyk *et* *al*. 2005). DHE is reported to have a particular affinity to $O_2^-$ compared to other ROS (Soh and Soh 2006). DHE is also reported to require intercalation with DNA in order to fully fluoresce (Negre-Salvayre *et al*. 2002).

Luminescent dyes are reported to confer much higher levels of specificity to particular ROS. Luminol and lucinigen are reported to luminesce only in response to $O_2^-$ (Faulkner and Fridovich 1993). However, contradicting literature suggests the dyes are oxidised nonspecifically by hypochlorite, $H_2O_2$ (Gross *et al*. 2009) and peroxynitrite (Radi *et al*. 1993).

Photo-bleaching has been identified as a major challenge when using fluorescent dyes to monitor ROS production in real-time. Many optimisation methods have been purported to overcome this issue (Afzal *et al*. 2003), however, the long exposure times sometimes required during fluorescence and confocal microscopy have skewing effects upon observed intensity. Dyes such as dihydrorhodamine-123 (DHR123) and 2',7'-dichlorodihydrofluorescein diacetate (DCF-DA) have been reported to display disparate emission fluorescence intensity (FI) responses when used to monitor ROS production induced by UVA (Boulton *et al*. 2011). Optimisation of dye employment and identification of ROS generation mechanisms outside of cellular processes formed the basis of much of the work discussed in Chapter 2. Due to the intrinsic photosensitivity of these compounds, DHR123 and DCF-DA have been reported as difficult to use and unreliable without properly controlled experimentation (Boulton *et al*. 2011; Chen *et al*. 2010).

### 1.5.2 Established techniques of intracellular pH measurement

Fluorescent dyes have long been implemented to estimate changes in pH *in vitro* and like those used for sensing ROS, a variety of monitoring techniques have been used to measure the resulting fluorescence. FITC has been extensively employed in monitoring changes in $pH_i$ *in vitro* (Lanz *et al*. 1997; Liu *et al*. 2007; Savina *et al*. 2006), however as the free dye was prone to uneven loading, leaching and sequestration, calibration difficulties reduced the confidence in data reported (Chen *et al*. 2010; Lanz *et al*. 1997). Dextran conjugation of pH-sensitive fluorescent dyes has been used to reduce the amount of dye leached from the cell once introduced (Geisow 1984). More recently this dye anchoring method has been exploited to prevent the leaching of dye from polymer nanoparticles for intracellular analysis (Webster *et al*. 2005). Although marked improvement in terms of leaching has been observed, the inherent membrane impermeability of the conjugated dye means intracellular delivery relies upon the very time consuming, difficult and cell perturbing technique of microinjection.

True pH-sensitive microelectrodes have been used for the voltammetric analysis of the pH within individual cells since first described in 1974 by R.C. Thomas (Thomas 1974) The electrodes require the subject cells to be tethered and impaled to facilitate intracellular measurement (Lucas *et al*. 1975). Recessed tip and double-barrelled microelectrodes are both commercially available, the former allowing very narrow bore and therefore less intrusive tips to be used, the latter facilitating simultaneous pH and membrane potential measurement.

Both microelectrode and Dextran-conjugated dye techniques require the tethering or restraint of individual cells in order to introduce a microneedle or electrode tip into the cell. The technique has been reported as being practically highly demanding, requiring much practice to develop the level of skill required to use the techniques without causing lethal damage to cells (Yan *et al*.). Even after the skills have been mastered the time constraints of measuring many cells on an individual basis renders microinjection and microelectrode investigation inappropriate for many studies.

In mycobiology, fluorescent proteins have been used to avoid the difficulties of cellular delivery. Proteins such as green fluorescent protein (GFP) and yellow fluorescent protein (YFP) have been codon-optimised for expression within the mycelium and to maximise FI changes in response to environmental pH. One such protein is pHluorin (Moseyko and Feldman 2001). This technique is starting to be implemented in mammalian cells using pH sensitive GFP (Bizzarri *et al*. 2006).

### 1.5.3 Polyacrylamide nanosensors: 'PEBBLE's

Recent advances in analytical chemistry have given rise to a generation of dye doped polyacrylamide matrices known as PEBBLEs (Photonic Explorers for Bioanalysis with Biologically Localised Embedding) (Buck *et al*. 2004a) These nanoscale sensing devices have been investigated as a potential tool to overcome the challenges presented by free fluorescent dyes in terms of long-term intracellular investigation. In Chapters 3, 4 and 7, polyacrylamide nanosensors have been discussed in length in terms of their development, application and integration with electrochemical sensing systems respectively. Briefly, polyacrylamide nanosensor technology was developed in response to the challenges regarding current intracellular monitoring techniques. Hand-pulled fibre optics were being used to monitor intracellular changes in $NO^{\bullet}$ (Tan *et al*. 1995). The tip of the optic was coated in a matrix that entrapped a stable reference dye and a $NO^{\bullet}$ sensitive fluorescent dye (Tan *et al*. 1995). Polyacylamide 'PEBBLE' nanosensors were fabricated using a reverse phase microemulsion with acrylamide monomer, signal dye and reference dye dispersed in the aqueous phase. Initiation of polymerisation whilst in emulsion resulted in the formation of nanoparticles of up to 200nm in diameter (Henderson *et al*. 2009). The concept of entrapping dyes within a polymer matrix presented many benefits over using free dye. Protection was conferred through the inherent size exclusion properties of the matrix, preventing unspecific binding of dyes to proteins (Buck *et al*. 2004b). This minimised the amount of dye sequestration by organelles and improved data confidence through the reduction of non-specific redox reaction (Buck *et al*. 2004b). Immobilising the reference and signal dyes locally conferred a ratiometric benefit to the quantification of sensed analyte (Buck *et al*. 2004a; Clark *et al*. 1999b). As the reference dye FI remained consistent throughout testing and only the signal dye was proportional to the analyte sensed the ratio of signal to reference FI shift in relation to intracellular $Ca^{2+}$ release (Clark *et al*. 1999b). The ratiometric element allowed comparison between individual cell populations without the risk of data corruption due to an uneven loading of dye. Some free dyes such as DAF-FM include a structural AM ester to aid cellular internalisation, the hydrolysis of which on contact with the cytosol produces cytotoxic formaldehyde. The encapsulation of the dye negates the need for the hydrolysis of this ester and permits the use of dyes that do not incorporate cell-penetrating devices, as the delivery of nanosensors to the intracellular environment relies on mechanisms outside of active transport or diffusion (Buck *et al*. 2004b).

### 1.5.4 Nanosensor delivery

A comprehensive investigation of various nanosensor delivery methods within cell models was carried out by Webster *et al* at the Boots School of Pharmacy in Nottingham (Webster *et al*. 2007). This extensive discussion of nanosensor delivery methods appeared to conclude that delivery must be tailored to the individual cell type or line that is being examined. Previously published work from the Diagnostic and

Therapeutic Technologies (DTT) group exploited phagocytosis, an innate internalisation process, to deliver nanosensors into rat alveoli NR8383 macrophage cells. The study monitored ROS generated in response to protein kinase C (PKC) stimulation with phorbol-12-myristate-13-acetate (PMA). The study is discussed in more depth in Chapter 3, which also details the development and application of ROS sensitive nanosensors. Whilst internalisation via phagocytosis is shown to be relatively facile all measurements following internalisation originated from within a membrane bound, isolated, selectively permeable organelle (Henderson *et al*. 2009; Webster *et al*. 2007) Exploitation of this natural process unfortunately restricts the use of nanosensors to a very marginal field of biological investigations regarding the phagosome, such as host pathogen interaction (Craig *et al*. 2009).

The most effective method used in this project to deliver nanosensors into cells exploited transfection reagents more commonly used to deliver DNA oligonucleotides to the nucleus in transformation procedures (Dalby *et al*. 2004). By forming complexes between nanosensors and the transfection reagents, the nanosensor cargo was delivered to the internal environment through fusion of the encapsulating liposome with the target cell membrane. Chapters 3 and 4 contain data pertaining to the optimisation of internalisation protocols for glioblastoma and cultured primary muscle cell delivery respectively, and discuss the challenges regarding cargo delivery more extensively. Previously published work has neither wholly championed nor refuted the usefulness of such a technique, although disparities were highlighted in the action of particular reagents such as Escort4 (Webster *et al*. 2007). Liposomal delivery of nanosensors ('lipofection') must be optimised between cell lines. Despite physiological similarities, protocols for lipofection were not transferable between cell types although the basic principle remained the same. This has been demonstrated by the varying successes reported in the literature when a single protocol is applied to many cell types (Clark *et al*. 1999a; Webster *et al*. 2007).

## 1.6 Tools for real time extracellular monitoring

Many methods have been reported for detecting extracellular $O_2^-$. Spectroscopic techniques using the reduction of cytochome *c* have been routinely used to monitor the rate of $O_2^-$ flux in real-time (Barbacanne *et al,* 2000). Unfortunately such methods are unreliable due to nonspecific interactions of cytochrome *c* with reductive species such as ascorbate and glutathione. Cytochrome *c* can readily be reoxidised by cytochrome *c* oxidase, $H_2O_2$ and peroxynitrite, which confers a diminishing effect upon the redox proteins absorbance at λ500nm, and subsequently leading to and underestimation of $O_2^-$ flux. Nitroblue tetrazolium (NBT) has frequently been employed as a spectroscopic $O_2^-$ detection system (Radenović *et al*. 2005) however NBT is ubiquitously used as a tool for assessing cellular viability due to the ease with which the compound undergoes reduction via mitochondrial reduction reactions as well as by coenzymes such as NADPH and FADH. NBT can easily cross the cell membrane and interact with endogenous reductive species. Data recorded from whole cell studies using this technique does not discriminate between the different modes of reduction. This inherent non-specificity for $O_2^-$ renders data generated with respect to $O_2^-$ production ambiguous and unreliable.

Electron spin resonance and spin trapping has also been used to directly detect $O_2^-$ (Liu *et al*. 2004). This technique is mainly employed with cell lysates and purified proteins (Pou *et al*. 1992) meaning the context of superoxide generation in terms of whole cell processes is lost. Although the method can be used to directly monitor the production of $O_2^-$ with good specificity, the inter-reactivity and short half life of the radical results in difficultly detecting $O_2^-$ in a biological system (Tarpey and Fridovich 2001a). So far the only methods capable of monitoring $O_2^-$ flux directly and in real time are amperometric (Manning *et al*. 2001; Santos *et al*. 2008; Shleev *et al*. 2006; Tammeveski *et al*. 1998).

### 1.6.1 Amperometric extracellular $O_2^-$ monitoring

Dynamic electrochemical detection of any molecule is underpinned by the principle that a change in current can be measured as a result of a dynamic redox reaction with a chemical species at the surface of an electrode. Conductive elements such as gold (Beissenhirtz *et al*. 2004; Chang *et al*. 2005; Dronov *et al*. 2008; Ge and Lisdat 2002), platinum (Koo *et al*. 2004; McNeil *et al*. 1989; Soldatkin *et al*. 2009), conducting polymers (Koh *et al*. 2008) and carbon fibres (Tanaka *et al*. 1991) have been used as biosensing electrodes, often following surface chemical functionalisation to convey specificity for a particular analyte of interest. A three-electrode system was used throughout this project, which comprised a steel counter electrode, a Ag/AgCl reference electrode and a gold working electrode. In brief, the working electrode was modified prior to use with linker molecule 3,3'-dithiobis(sulphosuccinimidylpropionate (DTSSP). This molecule formed a gold-thiol bond with the gold electrode surface and presented an amine reactive ester away from the surface, which bound to lysine residues located away from the redox active haem site in cytochrome *c*. The potential the working electrode is poised at against the reference electrode will further contribute towards electrode specificity. Amperometric biosensing systems often have a three electrode set up which consists of a working, reference and counter electrode. The reference electrode establishes a potential against which all changes can be measured. The counter electrode is set at an equal but opposite potential to the reference electrode. Its purpose is to prevent the reference electrode from carrying any current. If the reference electrode were to carry current, the reference potential would be altered. Redox reactions occur at the working electrode producing a change in current proportional to the concentration of the analyte in question.

### 1.6.2 Development of amperometric $O_2^-$ monitoring methods

The $O_2^-$ sensitive electrode method used throughout this project was first suggested in 1993 by McNeil and co-workers (Cooper *et al*, 1993) in a publication describing electron transfer between gold electrodes and the cytochrome *c* immobilised on the surface. In 1998, this work was further developed to demonstrate that a gold electrode with a cytochrome *c* functionalised surface could be used to monitor $O_2^-$ generated through the enzymatic decomposition of xanthine to uric acid and water by xanthine oxidase (XOD) (Tammeveski *et al*, 1998). It was demonstrated that cytochrome *c* exhibited great specificity for $O_2^-$ when covalently immobilised at a gold electrode surface and poised at a constant working potential of +100mV *vs.* Ag/AgCl. The cytochrome *c* functionalised electrode was used *in vitro* to monitor the extracellular flux of $O_2^-$ from PMA stimulated astrocytes, demonstrating a novel tool for real-time $O_2^-$ detection in biological systems (Manning *et al*, 1998). Other methods for sensing of $O_2^-$ using cytochrome *c* and gold electrodes exist offering different characteristics. Ge and Lisdat have reported a multi layered cytochrome *c* electrode for $O_2^-$ sensing, as well as electrodes using long chain thiols as linker molecules between the gold surface and haem containing protein. Shleev *et al (2006)* reported a superoxide sensitive electrode that uses azurin in place of cytochrome *c*, however the stability period of the electrode was reported to be decreased compared with the technique used by Manning *et al* (1998), despite being more labour intensive to prepare.

The functionalisation procedure of the Manning *et al* $O_2^-$ electrode was essentially described as a two-step process, and is discussed in greater detail in Chapters 5, 6 and 7. The first step was to use gold-thiol binding to immobilise the DTSSP linker molecules to the gold surface. The second step was to bind the redox protein cytochrome *c* to the linker molecules, covalently attaching it to the electrode. Many different methods and protocols have been reported for the functionalisation of electrodes for the specific detection of $O_2^-$ (Balamurugan and Chen 2008). The different functionalisation methods described using cytochrome *c* and gold electrodes conferred different electrode characteristics. Ge and Lisdat have reported a multi layered cytochrome *c* electrode for $O_2^-$ sensing, as well as electrodes using long chain thiols as linker molecules between the gold surface and haem containing protein (Ge and Lisdat 2002). Many of the alternative protocols included multi-step protein layering and long incubation times (Beissenhirtz *et al*. 2004; Mao *et al*. 2008) however the simple 2-step method described by Manning *et al* strikes a balance between preparation time and sensitivity.

| Type of biosensor | Sensitivity (A mm$^{-2}$ M$^{-1}$) | Stability (h) | Preparation time (h) | Reference |
|---|---|---|---|---|
| Azurin-DTSSP | $6.0*10^2$ | ≈5 | ≈20 | (Shleev *et al*. 2006) |
| cytochrome *c*-DTSSP | $0.5*10^2$ | 6–8 | ≈20 | (Manning *et al*. 1998) |
| cytochrome *c*-MU | $2.5*10^2$ | ≥8 | ≈30 | (Ge and Lisdat 2002) |

**Table 1.1:** Adapted from (Shleev *et al*. 2008). The study compared $O_2^-$ electrodes prepared using the cytochrome *c* - DTSSP immobilisation protocol described by Manning *et al*, the long chain thiol cytochrome *c* protocol described by Ge and Lisdat and the Azurin – DTSSP protocol of Shleev *et al* in terms of the individual preparation time, stability and sensitivity. The Manning *et al* protocol strikes a good balance between short preparation time, longevity and sensing capability.

The cytochrome *c* functionalised electrode has been reported extensively in its application to $O_2^-$ monitoring of live cells and more recently isolated mitochondria (Aitken *et al*. 2007; Chang *et al*. 2005; Henderson 2009; Manning *et al*. 2001). The same group also reported a modelling investigation whereby the decomposition of xanthine by XOD is used to calibrate the electrode for quantitative analysis of samples. The haem group in cytochrome *c* was the active site of redox reactions with $O_2^-$. By applying a low voltage positive potential the protein will interact specifically with $O_2^-$. A recent study suggested that modification via site directed mutagenesis of the haem site to make it more electropositive could enhance the sensitivity of this protein without compromising its selectivity for $O_2^-$ (Wegerich *et al*. 2009).

## 1.7 Integration of intra- and extracellular monitoring systems

The short-lived nature of ROS moieties and their inter-reactivity has presented novel temporal and spatial challenges when attempting to monitor ROS production, interaction and flux (Thomas *et al*. 2006). Often ROS are transformed, sequestered or are metabolised before they can be sensed (Boulton *et al*. 2011), exemplifying the highly dynamic nature of these free radicals. Current ROS detection techniques rely upon enzyme induction, cellular damage or secondary metabolites as indicators of production (Tarpey and Fridovich 2001b). Commercially available kits were developed to exploit endpoint methods however they do not carry the temporal precision or accuracy of the ideal real time, direct and simultaneous detection platform. Electrochemical detection of such species may be the only method viable for dynamic and selective monitoring of the extracellular production or flux, due to the high specificity for individual ROS reported (Henderson 2009; Manning *et al*. 2001). Promising work has been reported in the generation of novel encapsulated fluorescent sensors for intracellular ROS detection. The nanosensors were optimised in terms of ROS reporting through the incorporation of a ROS-responsive dye (DHR123) in conjunction with a non-responsive and stable reference dye (AlexaFluor568). This is discussed in more detail in Chapters 3 and 4 of this thesis. Together, the two technologies present highly compatible platforms that could be integrated to provide a platform to monitor both intra- and extracellular environment simultaneous in terms of discreet chemical species externally and more general ROS flux internally. The future application of this integrated platform to clinically relevant *in vitro* investigation of ROS induced pathophysiology could give unique insight regarding the temporal, spatial and intercellular effects of cytotoxic stimuli and cell signalling.

## 1.8 References

Afzal, M., Matsugo, S., Sasai, M., Xu, B., Aoyama, K., Takeuchi, T., 2003. Method to overcome photoreaction, a serious drawback to the use of dichlorofluorescein in evaluation of reactive oxygen species. Biochemical & Biophysical Research Communications 304(4), 619-624.

Aitken, G.R., Henderson, J.R., Chang, S.C., McNeil, C.J., Birch-Machin, M.A., 2007. Direct monitoring of UV-induced free radical generation in HaCaT keratinocytes. Clinical & Experimental Dermatology 32(6), 722-727.

Alvin Koh, W.C., Rahman, M.A., Choe, E.S., Lee, D.K., Shim, Y.-B., 2008. A cytochrome *c* modified-conducting polymer microelectrode for monitoring *in vivo* changes in nitric oxide. Biosensors & Bioelectronics 23(9), 1374-1381.

Awad, A.E., Kandalam, V., Chakrabarti, S., Wang, X., Penninger, J.M., Davidge, S.T., Oudit, G.Y., Kassiri, Z., 2010. Tumor necrosis factor induces matrix metalloproteinases in cardiomyocytes and cardiofibroblasts differentially via superoxide production in a PI3Kgamma-dependent manner. American Journal of Physiology - Cell Physiology 298(3), C679-692.

Babior, B.M., 1999. NADPH oxidase: an update. Blood 93(5), 1464-1476.

Babior, B.M., 2004. NADPH oxidase. Current Opinion in Immunology 16(1), 42-47.

Baier, J.r., Maisch, T., Maier, M., Engel, E., Landthaler, M., Bumler, W., 2006. Singlet oxygen generation by UVA light exposure of endogenous photosensitizers. Biophysical Journal 91(4), 1452-1459.

Balamurugan, A., Chen, S.-M., 2008. Fabrication of cytochrome *c*-poly(5-amino-2-napthalenesulfonic acid) electrode by one step procedure and direct electrochemistry of cytochrome *c*. Biosensors & Bioelectronics 24(4), 976-980.

Balcerczyk, A., Soszynski, M., Bartosz, G., 2005. On the specificity of 4-amino-5-methylamino-2',7'-difluorofluorescein as a probe for nitric oxide. Free Radical Biology & Medicine 39(3), 327-335.

Barbacanne, M.A., Souchard, J.P., Darblade, B., Iliou, J.P., Nepveu, F., Pipy, B., Bayard, F., Arnal, J.F., 2000. Detection of superoxide anion released extracellularly by endothelial cells using cytochrome *c* reduction, ESR, fluorescence and lucigenin-enhanced chemiluminescence techniques. Free Radical Biology & Medicine 29(5), 388-396.

Beissenhirtz, M.K., Scheller, F.W., Lisdat, F., 2004. A superoxide sensor based on a multilayer cytochrome *c* electrode. Analytical Chemistry 76(16), 4665-4671.

Berneburg, M., Plettenberg, H., Medve-Konig, K., Pfahlberg, A., Gers-Barlag, H., Gefeller, O., Krutmann, J., 2004. Induction of the Photoaging-Associated Mitochondrial Common Deletion *In vivo* in Normal Human Skin. Journal of Investigative Dermatology 122(5), 1277-1283.

Birch-Machin, M.A., 2006. The role of mitochondria in ageing and carcinogenesis. Clinical & Experimental Dermatology 31(4), 548-552.

Birch-Machin, M.A., Swalwell, H., 2010. How mitochondria record the effects of UV exposure and oxidative stress using human skin as a model tissue. Mutagenesis 25(2), 101-107.

Bizzarri, R., Arcangeli, C., Arosio, D., Ricci, F., Faraci, P., Cardarelli, F., Beltram, F., 2006. Development of a novel GFP-based ratiometric excitation and emission pH indicator for intracellular studies. Biophysical Journal 90(9), 3300-3314.

Boulton, S., Anderson, A., Swalwell, H., Henderson, J.R., Manning, P., Birch-Machin, M.A., 2011. Implications of using the fluorescent probes, dihydrorhodamine 123 and 2',7'-dichlorodihydrofluorescein diacetate, for the detection of UVA-induced reactive oxygen species. Free Radical Research 45(2), 139-146.

Bringmann, G., Feineis, D., God, R., Fahr, S., Wesemann, W., Clement, H.W., Grote, C., Kolasiewicz, W., Sontag, K.H., Heim, C., Sontag, T.A., Reichmann, H., Janetzky, B., Rausch, W.D., Abdel-Mohsen, M., Koutsilieri, E., Götz, M.E., Gsell, W., Zielke, B., Riederer, P., 1996. Neurotoxic effects on the dopaminergic system induced by TaClo (1-trichloromethyl-1,2,3,4-tetrahydro-β-carboline), a potential mammalian alkaloid: *In vivo* and *in vitro* studies. Biogenic Amines 12(2), 83-102.

Bringmann, G., God, R., Feineis, D., Janetzky, B., Reichmann, H., 1995. TaClo as a neurotoxic lead: improved synthesis, stereochemical analysis, and inhibition of the mitochondrial respiratory chain. Journal of Neural Transmission Supplementum 46, 245-254.

Buck, S.M., Koo, Y.E., Park, E., Xu, H., Philbert, M.A., Brasuel, M.A., Kopelman, R., 2004a. Optochemical nanosensor PEBBLEs: photonic explorers for bioanalysis with biologically localised embedding. Current Opinion in Chemical Biology 8(5), 540-546.

Buck, S.M., Xu, H., Brasuel, M., Philbert, M.A., Kopelman, R., 2004b. Nanoscale probes encapsulated by biologically localised embedding (PEBBLEs) for ion sensing and imaging in live cells. Talanta 63(1), 41-59.

Carsillo, M., Kutala, V.K., Puschel, K., Blanco, J., Kuppusamy, P., Niewiesk, S., 2009. Nitric oxide production and nitric oxide synthase type 2 expression by cotton rat (Sigmodon hispidus) macrophages reflect the same pattern as human macrophages. Developmental & Comparative Immunology 33(5), 718-724.

Chang, S.C., Pereira-Rodrigues, N., Henderson, J.R., Cole, A., Bedioui, F., McNeil, C.J., 2005. An electrochemical sensor array system for the direct, simultaneous *in vitro* monitoring of nitric oxide and superoxide production by cultured cells. Biosensors & Bioelectronics 21(6), 917-922.

Cheeseman, K.H., 1993. Mechanisms and effects of lipid peroxidation. Molecular Aspects of Medicine 14(3), 191-197.

Cheeseman, K.H., Slater, T.F., 1993. An introduction to free radical biochemistry. British Medical Bulletin 49(3), 481-493.

Chen, X., Zhong, Z., Xu, Z., Chen, L., Wang, Y., 2010. 2',7'-Dichlorodihydrofluorescein as a fluorescent probe for reactive oxygen species measurement: Forty years of application and controversy. Free Radical Research 44(6), 587-604.

Clark, H.A., Hoyer, M., Philbert, M.A., Kopelman, R., 1999a. Optical nanosensors for chemical analysis inside single living cells. 1. Fabrication, characterization, and methods for intracellular delivery of PEBBLE sensors. Analytical Chemistry 71(21), 4831-4836.

Clark, H.A., Kopelman, R., Tjalkens, R., Philbert, M.A., 1999b. Optical nanosensors for chemical analysis inside single living cells. 2. Sensors for pH and calcium and the intracellular application of PEBBLE sensors. Analytical Chemistry 71(21), 4837-4843.

Cookson, M.R., Menzies, F.M., Manning, P., Eggett, C.J., Figlewicz, D.A., McNeil, C.J., Shaw, P.J., 2002. Cu/Zn superoxide dismutase (SOD1) mutations associated with familial amyotrophic lateral sclerosis (ALS) affect cellular free radical release in the presence of oxidative stress. Amyotrophic Lateral Sclerosis & Other Motor Neuron Disorders 3(2), 75-85.

Cooper, J.M., Greenough, K.R., McNeil, C.J., 1993. Direct electron transfer reactions between immobilised cytochrome *c* and modified gold electrodes. Journal of Electroanalytical Chemistry 347(1-2), 267-275.

Corral-Debrinski, M., Horton, T., Lott, M.T., Shoffner, J.M., Beal, M.F., Wallace, D.C., 1992. Mitochondrial DNA deletions in human brain: regional variability and increase with advanced age. Nature Genetics 2(4), 324-329.

Craig, M., Slauch, J.M., 2009. Phagocytic superoxide specifically damages an extracytoplasmic target to inhibit or kill Salmonella. PLoS ONE 4(3), e4975.

Dalby, B., Cates, S., Harris, A., Ohki, E.C., Tilkins, M.L., Price, P.J., Ciccarone, V.C., 2004. Advanced transfection with Lipofectamine 2000 reagent: primary neurons, siRNA, and high-throughput applications. Methods 33(2), 95-103.

Danial, N.N., Korsmeyer, S.J., 2004. Cell Death: Critical Control Points. Cell 116(2), 205-219.

Deng, T., Xu, K., Zhang, L., Zheng, X., 2008. Dynamic determination of Ox-LDL-induced oxidative/nitrosative stress in single macrophage by using fluorescent probes. Cell Biology International 32(11), 1425-1432.

Di Matteo, V., Pierucci, M., Benigno, A., Crescimanno, G., Esposito, E., Di Giovanni, G., 2009. Involvement of nitric oxide in nigrostriatal dopaminergic system degeneration: a neurochemical study. Annals of the New York Academy of Sciences 1155, 309-315.

Dronov, R., Kurth, D.G., Mohwald, H., Scheller, F.W., Friedmann, J., Pum, D., Sleytr, U.B., Lisdat, F., 2008. Self-assembly of S-layer-enveloped cytochrome *c* polyelectrolyte multilayers. Langmuir 24(16), 8779-8784.

Fahn, S., Cohen, G., 1992. The oxidant stress hypothesis in Parkinson's disease: Evidence supporting it. Annals of Neurology 32(6), 804-812.

Faulkner, K., Fridovich, I., 1993. Luminol and lucigenin as detectors for $O_2^-$. Free Radical Biology & Medicine 15(4), 447-451.

Felitsyn, N., Stacpoole, P.W., Notterpek, L., 2007. Dichloroacetate causes reversible demyelination *in vitro*: potential mechanism for its neuropathic effect. Journal of Neurochemistry 100(2), 429-436.

Fisher, G.J., Quan, T., Purohit, T., Shao, Y., Cho, M.K., He, T., Varani, J., Kang, S., Voorhees, J.J., 2009. Collagen fragmentation promotes oxidative stress and elevates matrix metalloproteinase-1 in fibroblasts in aged human skin. American Journal of Pathology 174(1), 101-114.

Fouque, F.O., Brivet, M., Boutron, A., Vequaud, C., Marsac, C.C., Zabot, A.N.D.M.-T.R.S., Benelli, C., 2003. Differential effect of DCA treatment on the pyruvate dehydrogenase Complex In patients with severe PDHC deficiency. Pediatric Research 53(5), 793-799.

Ge, B., Lisdat, F., 2002. Superoxide sensor based on cytochrome *c* immobilised on mixed-thiol SAM with a new calibration method. Analytica Chimica Acta 454(1), 53-64.

Geisow, M.J., 1984. Fluorescein conjugates as indicators of subcellular pH : A critical evaluation. Experimental Cell Research 150(1), 29-35.

Genova, M.L., Ventura, B., Giuliano, G., Bovina, C., Formiggini, G., Parenti Castelli, G., Lenaz, G., 2001. The site of production of superoxide radical in mitochondrial Complex I is not a bound ubisemiquinone but presumably iron-sulfur cluster N2. FEBS Letters 505(3), 364-368.

Gillespie, J.I., Markerink-van Ittersum, M., de Vente, J., 2004. cGMP-generating cells in the bladder wall: identification of distinct networks of interstitial cells. British Journal of Urology International 94(7), 1114-1124.

Gross, S., Gammon, S.T., Moss, B.L., Rauch, D., Harding, J., Heinecke, J.W., Ratner, L., Piwnica-Worms, D., 2009. Bioluminescence imaging of myeloperoxidase activity *in vivo*. Nature Medicine 15(4), 455-461.

Halliwell, B., 1991. Reactive oxygen species in living systems: Source, biochemistry, and role in human disease. The American Journal of Medicine 91(3), S14-S22.

Hallstrom, S., Franz, M., Gasser, H., Vodrazka, M., Semsroth, S., Losert, U.M., Haisjackl, M., Podesser, B.K., Malinski, T., 2008. S-nitroso human serum albumin reduces ischaemia/reperfusion injury in the pig heart after unprotected warm ischaemia. Cardiovascular Research 77(3), 506-514.

Han, D., Williams, E., Cadenas, E., 2001. Mitochondrial respiratory chain-dependent generation of superoxide anion and its release into the intermembrane space. Biochem J 353(Pt 2), 411-416.

Hartley, A., Stone, J.M., Heron, C., Cooper, J.M., Schapira, A.H.V., 1994. Complex I inhibitors induce dose-dependent apoptosis in PC12 cells: relevance to Parkinson's disease. Journal of Neurochemistry 63(5), 1987-1990.

Henderson, G.N., Curry, S.H., Derendorf, H., Wright, E.C., Stacpoole, P.W., 1997. Pharmacokinetics of dichloroacetate in adult patients with lactic acidosis. Journal of Clinical Pharmacology 37(5), 416-425.

Henderson, J.R., Fulton, D.A., McNeil, C.J., Manning, P., 2009. The development and *in vitro* characterisation of an intracellular nanosensor responsive to reactive oxygen species. Biosensors & Bioelectronics 24(12), 3608-3614.

Henderson, J.R., Swalwell, H., Boulton, S.J., Manning, P., Birch-Machin, M., McNeil, C.J., 2009. Direct, real-time monitoring of superoxide generation in isolated mitochondria. Free Radical Research 43(9), 1-7.

Herrero, A., Barja, G., 1997. Sites and mechanisms responsible for the low rate of free radical production of heart mitochondria in the long-lived pigeon. Mechanisms of Ageing & Development 98(2), 95-111.

Koo, Y.E., Cao, Y., Kopelman, R., Koo, S.M., Brasuel, M., Philbert, M.A., 2004. Real-time measurements of dissolved oxygen inside live cells by organically modified silicate fluorescent nanosensors. Analytical Chemistry 76(9), 2498-2505.

Kourie, J.I., 1998. Interaction of reactive oxygen species with ion transport mechanisms. American Journal of Physiology - Cell Physiology 275(1), C1-C24.

Krishnan, K.J., Harbottle, A., Birch-Machin, M.A., 2004. The use of a 3895 bp mitochondrial DNA deletion as a marker for sunlight exposure in human skin. Journal of Investigative Dermatology 123(6), 1020-1024.

Krutmann, J., 2000. Ultraviolet A radiation-induced biological effects in human skin: relevance for photoaging and photodermatosis. Journal of Dermatological Science 23 (1), S22-26.

Krutmann, J., Schroeder, P., 2009. Role of mitochondria in photoaging of human skin: the defective powerhouse model. Journal of Investigative Dermatology Symposium Proceedings 14(1), 44-49.

Kurauchi, Y., Hisatsune, A., Isohama, Y., Katsuki, H., 2009. Nitric oxide-cyclic GMP signaling pathway limits inflammatory degeneration of midbrain dopaminergic neurons: cell type-specific regulation of heme oxygenase-1 expression. Neuroscience 158(2), 856-866.

Lambert, A.J., Brand, M.D., 2004. Inhibitors of the quinone-binding site allow rapid superoxide production from mitochondrial NADH:ubiquinone oxidoreductase (Complex I). Journal of Biological Chemistry 279(38), 39414-39420.

Langer, D.A., Das, A., Semela, D., Kang-Decker, N., Hendrickson, H., Bronk, S.F., Katusic, Z.S., Gores, G.J., Shah, V.H., 2008. Nitric oxide promotes caspase-independent hepatic stellate cell apoptosis through the generation of reactive oxygen species. Hepatology 47(6), 1983-1993.

Lanz, E., Gregor, M., Slavík, J., Kotyk, A., 1997. Use of FITC as a fluorescent probe for intracellular pH measurement. Journal of Fluorescence 7(4), 317-319.

Laurent, A., Nicco, C., Chéreau, C., Goulvestre, C., Alexandre, J.r.m., Alves, A., Lévy, E., Goldwasser, F., Panis, Y., Soubrane, O., Weill, B., Batteux, F.d.r., 2005. Controlling tumor growth by modulating endogenous production of reactive oxygen species. Cancer Research 65(3), 948-956.

Lin, M.T., Beal, M.F., 2006. Mitochondrial dysfunction and oxidative stress in neurodegenerative diseases. Nature 443(7113), 787-795.

Liu, K., Sun, J., Song, Y.-g., Liu, B., Xu, Y.-k., Zhang, S.-x., Tian, Q., Liu, Y., 2004. Superoxide, hydrogen peroxide and hydroxyl radical in D1/D2/cytochrome b-559 photosystem II reaction center complex. Photosynthesis Research 81(1), 41-47.

Liu, S.L., Li, Y.H., Shi, G.Y., Tang, S.H., Jiang, S.J., Huang, C.W., Liu, P.Y., Hong, J.S., Wu, H.L., 2009. Dextromethorphan reduces oxidative stress and inhibits atherosclerosis and neointima formation in mice. Cardiovascular Research 82(1), 161-169.

Liu, Y.-S., Sun, Y., Vernier, P.T., Liang, C.-H., Chong, S.Y.C., Gundersen, M.A., 2007. pH-sensitive photoluminescence of CdSe/ZnSe/ZnS quantum dots in human ovarian cancer cells. Journal of Physical Chemistry *c* 111(7), 2872-2878.

Lucas, M.L., Schneider, W., Haberich, F.J., Blair, J.A., 1975. Direct measurement by pH-microelectrode of the pH microclimate in rat proximal jejunum. Proceedings of the Royal Society of London. Series B. Biological Sciences 192(1106), 39-48.

Mahns, A., Melchheier, I., Suschek, C.V., Sies, H., Klotz, L.O., 2003. Irradiation of cells with ultraviolet-A (320-400 nm) in the presence of cell culture medium elicits biological effects due to extracellular generation of hydrogen peroxide. Free Radical Research 37(4), 391-397.

Manning, P., Cookson, M.R., McNeil, C.J., Figlewicz, D., Shaw, P.J., 2001. Superoxide-induced nitric oxide release from cultured glial cells. Brain Research 911(2), 203-210.

Manning, P., McNeil, C.J., Cooper, J.M., Hillhouse, E.W., 1998. Direct, real-time sensing of free radical production by activated human glioblastoma cells. Free Radical Biology & Medicine 24(7-8), 1304-1309.

Mao, L., Tian, Y., Ohsaka, T., 2008. Superoxide electrochemical sensors and biosensors: Principles, development and applications. Electrochemical Sensors, Biosensors and their Biomedical Applications, Academic Press, San Diego. p145-185.

Maresca, V., Flori, E., Briganti, S., Mastrofrancesco, A., Fabbri, C., Mileo, A.M., Paggi, M.G., Picardo, M., 2008. Correlation between melanogenic and catalase activity in *in vitro* human melanocytes: a synergic strategy against oxidative stress. Pigment Cell & Melanoma Research 21(2), 200-205.

Masserano, J.M., Gong, L., Kulaga, H., Baker, I., Wyatt, R.J., 1996. Dopamine induces apoptotic cell death of a catecholaminergic cell line derived from the central nervous system. Molecular Pharmacology 50(5), 1309-1315.

Massion, P.B., Pelat, M., Belge, C., Balligand, J.L., 2005. Regulation of the mammalian heart function by nitric oxide. Comparative Biochemistry & Physiology Part A, Molecular & Integrative Physiology 142(2), 144-150.

McLaughlin, B.A., Nelson, D., Erecińska, M., Chesselet, M.F., 1998. Toxicity of dopamine to striatal neurons *in vitro* and potentiation of cell death by a mitochondrial inhibitor. Journal of Neurochemistry 70(6), 2406-2415.

McNeil, C.J., Spoors, J.A., Cocco, D., Cooper, J.M., Bannister, J.V., 1989. Thermostable reduced nicotinamide adenine dinucleotide oxidase: application to amperometric enzyme assay. Analytical Chemistry 61(1), 25-29.

Menon, E.L., Morrison, H., 2002. Formation of singlet oxygen by urocanic acid by UVA irradiation and some consequences thereof. Photochemistry & Photobiology 75(6), 565-569.

Mizock, B.A., Falk, J.L., 1992. Lactic acidosis in critical illness. Critical Care Medicine 20(1), 80-93.

Moseyko, N., Feldman, L.J., 2001. Expression of pH-sensitive green fluorescent protein in Arabidopsis thaliana. Plant, Cell & Environment 24(5), 557-563.

Mott, J.L., Zhang, D., Zassenhaus, H.P., 2005. Mitochondrial DNA mutations, apoptosis, and the misfolded protein response. Rejuvenation Research 8(4), 216-226.

Muller, F.L., Liu, Y., Van Remmen, H., 2004. Complex III releases superoxide to both sides of the inner mitochondrial membrane. Journal of Biological Chemistry 279(47), 49064-49073.

Negre-Salvayre, A., Augé, N., Duval, C., Robbesyn, F., Thiers, J.-C., Nazzal, D., Benoist, H., Salvayre, R., 2002. Detection of intracellular reactive oxygen species in cultured cells using fluorescent probes. Methods in Enzymology, Academic Press. Pasedena, California. pp. 62-71.

Newland, P.L., Yates, P., 2008. Nitric oxide modulates salt and sugar responses via different signalling pathways. Chemical Senses 33(4), 347-356.

Nicotra, A., Pierucci, F., Parvez, H., Senatori, O., 2004. Monoamine oxidase expression during development and aging. Neurotoxicology 25(1-2), 155-165.

Oh, P.S., Lim, K.T., Oh, P.-S., Lim, K.-T., 2008. Blocking of intracellular ROS production by phytoglycoprotein (30 kDa) causes anti-proliferation in bisphenol A-stimulated Chang liver cells. Journal of Applied Toxicology 28(6), 749-758.

Ozgocmen, S., Ozyurt, H., Sogut, S., Akyol, O., 2006. Current concepts in the pathophysiology of fibromyalgia: the potential role of oxidative stress and nitric oxide. Rheumatology International 26(7), 585-597.

Patel, R.P., Moellering, D., Murphy-Ullrich, J., Jo, H., Beckman, J.S., Darley-Usmar, V.M., 2000. Cell signaling by reactive nitrogen and oxygen species in atherosclerosis. Free Radical Biology & Medicine 28(12), 1780-1794.

Petersen, A.B., Gniadecki, R., Vicanova, J., Thorn, T., Wulf, H.C., 2000. Hydrogen peroxide is responsible for UVA-induced DNA damage measured by alkaline comet assay in HaCaT keratinocytes. Journal of Photochemistry & Photobiology B: Biology 59(1-3), 123-131.

Pou, S., Pou, W.S., Bredt, D.S., Snyder, S.H., Rosen, G.M., 1992. Generation of superoxide by purified brain nitric oxide synthase. Journal of Biological Chemistry 267(34), 24173-24176.

Radenović, L., Selaković, V., Kartelija, G., 2005. Mitochondrial superoxide production and MnSOD activity after exposure to agonist and antagonists of ionotropic glutamate receptors in hippocampus. Annals of the New York Academy of Sciences 1048(1), 363-365.

Radi, R., Cosgrove, T.P., Beckman, J.S., Freeman, B.A., 1993. Peroxynitrite-induced luminol chemiluminescence. Journal of iochemistry 15(290), 51-57.

Read, S.J., Manning, P., McNeil, C.J., Hunter, A.J., Parsons, A.A., 1999. Effects of sumatriptan on nitric oxide and superoxide balance during glyceryl trinitrate infusion in the rat. Implications for antimigraine mechanisms. Brain Research 847(1), 1-8.

Rinna, A., Torres, M., Forman, H.J., 2006. Stimulation of the alveolar macrophage respiratory burst by ADP causes selective glutathionylation of protein tyrosine phosphatase 1B. Free Radical Biology & Medicine 41(1), 86-91.

Rinne, J.O., Mlic, J.R., Paljärvi, L., Rinne, U.K., 1989. Dementia in Parkinson's disease is related to neuronal loss in the medial *substantia nigra*. Annals of Neurology 26(1), 47-50.

Robergs, R.A., Ghiasvand, F., Parker, D., 2004. Biochemistry of exercise-induced metabolic acidosis. American Journal of Physiology - Regulatory, Integrative & Comparative Physiology 287(3), R502-R516.

Sachi, Y., Hirota, K., Masutani, H., Toda, K.-i., Okamoto, T., Takigawa, M., Yodoi, J., 1995. Induction of ADF/TRX by oxidative stress in keratinocytes and lymphoid cells. Immunology Letters 44(2-3), 189-193.

Santos, R.M., Lourenco, C.F., Piedade, A.P., Andrews, R., Pomerleau, F., Huettl, P., Gerhardt, G.A., Laranjinha, J., Barbosa, R.M., 2008. A comparative study of carbon fiber-based microelectrodes for the measurement of nitric oxide in brain tissue. Biosensors & Bioelectronics 24(4), 704-709.

Sarti, P., Avigliano, L., Gorlach, A., Brune, B., 2002. Superoxide and nitric oxide participation in cell communication. Cell Death & Differentiation 9(10), 1160-1162.

Savina, A., Jancic, C., Hugues, S., Guermonprez, P., Vargas, P., Moura, I.C., Lennon-Duménil, A.-M., Seabra, M.C., Raposo, G., Amigorena, S., 2006. NOX2 controls phagosomal pH to regulate antigen processing during cross-presentation by dendritic cells. Cell 126(1), 205-218.

Shleev, S., Wetterö, J., Magnusson, K.-E., Ruzgas, T., 2006. Electrochemical characterization and application of azurin-modified gold electrodes for detection of superoxide. Biosensors & Bioelectronics 22(2), 213-219.

Shleev, S., Wettero, J., Magnusson, K.E., Ruzgas, T., 2008. Simultaneous use of electrochemistry and chemiluminescence to detect reactive oxygen species produced by human neutrophils. Cell Biology International 32(12), 1486-1496.

Soh, N., Soh, N., 2006. Recent advances in fluorescent probes for the detection of reactive oxygen species. Analytical & Bioanalytical Chemistry 386(3), 532-543.

Soldatkin, O.O., Schuvailo, O.M., Marinesco, S., Cespuglio, R., Soldatkin, A.P., 2009. Microbiosensor based on glucose oxidase and hexokinase co-immobilised on platinum microelectrode for selective ATP detection. Talanta 78(3), 1023-1028.

Srinivasan, A., Lehmler, H.-J., Robertson, L.W., Ludewig, G., 2001. Production of DNA strand breaks *in vitro* and reactive oxygen species *in vitro* and in HL-60 cells by PCB metabolites. Toxicological Sciences 60(1), 92-102.

Stacpoole, P.W., Moore, G.W., Kornhauser, D.M., 1979. Toxicity of chronic dichloroacetate. New England Journal of Medicine 300(7), 372.

Tammeveski, K., Tenno, T.T., Mashirin, A.A., Hillhouse, E.W., Manning, P., McNeil, C.J., 1998. Superoxide electrode based on covalently immobilised cytochrome *c*: modelling studies. Free Radical Biology & Medicine 25(8), 973-978.

Tan, W., Shi, Z.-Y., Kopelman, R., 1995. Miniaturised fiber-optic chemical sensors with fluorescent dye-doped polymers. Sensors & Actuators B: Chemical 28(2), 157-163.

Tanaka, K., Kobayashi, F., Isogai, Y., Iizuka, T., 1991. Electrochemical determination of superoxide anions generated from a single neutrophil. Journal of Electroanalytical Chemistry & Interfacial Electrochemistry 26(3), 413-421.

Tarpey, M.M., Fridovich, I., 2001a. Methods of detection of vascular reactive species. Circulation Research 89(3), 224-236.

Tarpey, M.M., Fridovich, I., 2001b. Methods of detection of vascular reactive species: nitric oxide, superoxide, hydrogen peroxide, and peroxynitrite. Circulation Research. 89, 224-236.

Thomas, D.D., Ridnour, L.A., Espey, M.G., Donzelli, S., Ambs, S., Hussain, S.P., Harris, C.C., DeGraff, W., Roberts, D.D., Mitchell, J.B., Wink, D.A., 2006. Superoxide fluxes limit nitric oxide-induced signaling. Journal of Biological Chemistry 281(36), 25984-25993.

Thomas, R.C., 1974. Intracellular pH of snail neurones measured with a new pH-sensitive glass micro-electrode. Journal of Physiology 238(1), 159-180.

Urakami, H., Abe, Y., Grisham, M.B., 2007. Role of reactive metabolites of oxygen and nitrogen in partial liver transplantation: lessons learned from reduced-size liver ischaemia and reperfusion injury. Clinical & Experimental Pharmacology & Physiology 34(9), 912-919.

Van Lente, F., 1993. Free Radicals. Analytical Chemistry. 65(12), 374-377.

Webster, A., Compton, S.J., Aylott, J.W., 2005. Optical calcium sensors: development of a generic method for their introduction to the cell using conjugated cell penetrating peptides. Analyst 130(2), 163-170.

Webster, A., Coupland, P., Houghton, F.D., Leese, H.J., Aylott, J.W., 2007. The delivery of PEBBLE nanosensors to measure the intracellular environment. Biochemical Society Transactions 35(Pt 3), 538-543.

Wegerich, F., Turano, P., Allegrozzi, M., Mohwald, H., Lisdat, F., 2009. Cytochrome *c* mutants for superoxide biosensors. Analytical Chemistry 81(8), 2976-2984.

Wei, Y.-H., Lee, H.-C., 2002. Oxidative stress, mitochondrial DNA mutation, and impairment of antioxidant enzymes in aging. Experimental Biology & Medicine. 227(9), 671-682.

Wondrak, G.T., Jacobson, M.K., Jacobson, E.L., 2006. Endogenous UVA-photosensitizers: mediators of skin photodamage and novel targets for skin photoprotection. Photochemical & Photobiological Sciences 5(2), 215-237.

Yan, Q., Loiselle, F.B., Casey, J.R., Measurement of intracellular pH. In: Walker, J.M. (Ed.), Membrane Transporters in Drug Discovery and Development, Humana Press, New York. pp. 311-331.

Yin, J.X., Yang, R.F., Li, S., Renshaw, A.O., Li, Y.L., Schultz, H.D., Zimmerman, M.C., 2010. Mitochondria-produced superoxide mediates angiotensin II-induced inhibition of neuronal potassium current. American Journal of Physiology - Cell Physiology 298(4), C857-865.

Zeng, X., Chen, J., Deng, X., Liu, Y., Rao, M.S., Cadet, J.-L., Freed, W.J., 2006. An *in vitro* model of human dopaminergic neurons derived from embryonic stem cells: MPP+ toxicity and GDNF neuroprotection. Neuropsychopharmacology 31(12), 2708-2715.

Zmijewski, J.W., Lorne, E., Banerjee, S., Abraham, E., 2009. Participation of mitochondrial respiratory Complex III in neutrophil activation and lung injury. American Journal of Physiology – Lung Cellular & Molecular Physiology. 296, L624-634.

# Chapter 2. Implications of using the fluorescent dyes, dihydrorhodamine-123 and 2',7'-dichlorodihydrofluorescein diacetate, for the detection of UVA-induced reactive oxygen species

**S. Boulton, A. Anderson, H. Swalwell, J.R. Henderson, P. Manning, M.A. Birch-Machin**

*Free Radical Research, February 2011; 45(2): 115–122*

## 2.1 Introduction

The determination of intracellular ROS generation is an important part of many *in vitro* investigations. DHR123 and DCF-DA are two dyes capable of reporting changes of the intracellular oxidative stress state, both have formed important parts of many studies and have received a great deal of press. During investigation of UVA induced stress in HaCaT keratinocytes, abhorrent false positive results were noticed within control samples. The effects of diluent, UVA pre-treatment and loading protocols have been investigated in the hope of identifying a best practice regimen. This study aimed to address the pitfalls of using both DHR123 and DCF-DA as dyes for UVA induced stress, and highlight precautions that can be taken to maintain data validity.

ROS are known to be key signalling species of cellular stress, damage and death (Cheeseman 1993a, b; Halliwell and Gutteridge 1984; Kaczara *et al*. 2010; Yuan *et al*. 2009). In addition to their involvement in communication and oxidative damage, it is now thought that these short lived and potentially highly reactive molecules may harbour a more intrinsic and sophisticated role in ubiquitous cellular processes (Cui *et al*. 2006; Foyer and Noctor 2005; McNeil and Manning 2002; Traverso *et al*. 2007).

The development of sensors capable of reporting and quantifying changes in ROS has been the focus of a considerable amount of research (Aitken *et al*. 2007; Barbacanne *et al*. 2000; Chang *et al*. 2005a; Chang *et al*. 2005b; Henderson *et al*. 2009; McNeil and Manning 2002; Tammeveski *et al*. 1998; Van Lente 1993), though the realisation of a real-time, direct and dynamic sensor method remains somewhat elusive. The fluorescent dyes DHR123 and DCF-DA are commonly used to detect production of cellular ROS in a variety of cell types. In this process DHR123 is oxidised from non-fluorescent DHR123 to fluorescent rhodamine 123 (R123), and DCF-DA is similarly oxidised to its fluorescent product DCF.

Whilst studying UVA light induced oxidative stress with DHR123 and DCF-DA, there was an unexpected observation of abnormally large difference in the trend and magnitude of response between human skin keratinocytes (i.e. HaCaTs) loaded with ROS-sensitive dye either immediately before or after UVA exposure of the cultured cells. This suggested that UVA light may itself exhibit an effect on DHR123 and DCF-DA that is independent of cellular ROS production. A possible explanation for this observation may in part be due to a non-specific interaction with the cell culture medium as a focused review of previous studies identified similar anomalies which may be attributed to the nature or content of the cell culture medium (Granzow *et al*. 1995; Grzelak *et al*. 2001; Long and Halliwell 2009). Therefore, this current study addresses three important questions regarding the optimisation and good laboratory practice surrounding the future use of DHR123 and DCF-DA in detecting ROS production in cell biology investigations, building upon a foundation of peer reviewed investigatory work surrounding potential pitfalls of fluorescent ROS measurement (Afzal *et al*. 2003; Chen *et al*. 2010; Mahns *et al*. 2003; Soh and Soh 2006). First, does the experimental diluent (e.g. culture medium/buffer) interact with the dyes thereby modifying its response to ROS? Second, does UVA irradiation affect the fluorescence of DHR123 and DCF-DA and if so, is this effect independent of ROS interaction? Third, does the effect on the dyes alter their capacity or sensitivity for ROS detection?

## 2.2 Materials and methods

Propidium iodide (PI), DHR123, DCF-DA, PBS tablets, xanthine and XOD were all purchased from Sigma-Aldrich (Poole, UK)

### 2.2.1 Cell culture and preparation

Spontaneously immortalised basal keratinocyte cell line HaCaT was cultured in phenol red free Dulbecco's Modified Eagle's Medium (DMEM) supplemented with 10% foetal calf serum (FCS) and incubated at 37.5°C in a 5% $CO_2$ humidified atmosphere. Cells were grown to ~70% confluence before testing and underwent no more than 6 passages over the course of experimentation.

### 2.2.2 Fluorimeter-facilitated cell free measurements

The following settings were used for all fluorimetric analysis: DCF-DA: $\lambda_{ex}$495 nm, $\lambda_{em}$535 nm; DHR123: $\lambda_{ex}$488nm, $\lambda_{em}$520 nm. Phenol red free medium was employed throughout fluorimetric experimentation without modification unless otherwise stated. DHR123 and DCF-DA were used consistently at 25µM and 10µM respectively.

### 2.2.3 Quantifying UVA exposure dose response of dyes

Previous work by Gniadecki *et al* (Gniadecki *et al*, 2000) was used as a basis for the current UVA dose regime together with previous experience obtained from our studies using sub-lethal doses of UVR in cultured skin cells (Aitken *et al,* 2007). A dose of 10 Jcm$^{-2}$ was found to be sub-lethal but sufficient to induce increased cellular ROS generation. The source of the UVA irradiation was a glass filtered TL09 (Phillips TL100/09) providing a peak output of 350nm with a range of 315-410nm. DHR123 and DCF-DA were made to 25µM and 10µM respectively in plain DMEM, complete DMEM and PBS. Probe solutions were aliquoted into a white 96 well plate (Corning, UK), with the UVA negative control aliquots subsequently heavily masked from any UVA exposure. The plates were exposed to increasing doses of UVA from 0 to 10 Jcm$^{-2}$. Once all wells had received their allocated exposure, the UVA untreated wells were unmasked and the plate transferred to a Tecan Infinite M200 fluorimeter (Tecan, Austria) for FI measurement.

### 2.2.4 Observation of the effects of UVA on dye emission spectra

Two sample groups of both DHR123 and DCF-DA solution at working concentration were aliquoted to a white-walled 96 well plate in triplicate. One of the sample groups for each dye was heavily masked against UVA exposure. The plate was exposed to a 10 $Jcm^{-2}$ dose of UVA. Once exposure was complete, the plate was transferred to a Tecan Infinite M200 fluorimeter (Tecan, Austria) for fluorescence emission scan measurement. $\lambda_{ex}$ of 495nm was used for both dyes. $\lambda_{em}$ FI was measured by scanning from 450-650nm in 2nm steps.

### 2.2.5 Quantifying responses to xanthine/xanthine oxidase generated ROS

Immediately prior to use, each dye was irradiated with 10 $Jcm^{-2}$ UVA, diluted in PBS to working concentration and then transferred (50 µl/well) to a white 96-well plate (Corning, UK). Each well in the 'baseline' column (i.e. 9 replicate wells) of the plate received a further 50 µl PBS; thereby diluting the dye to a working concentration to account for baseline FI. 4 columns then received 40 µl 10 mM xanthine in PBS, 1 column received a further 10 µl PBS and served as a control for any FI changes elicited by xanthine. The remaining 3 columns were treated with 10 µl of differing XOD concentrations making the final concentration range of enzyme across the plate 0.1, 0.5 and 2.5 $Uml^{-1}$. Once all these additions were completed, the plate was incubated at room temperature for 5 min prior to being transferred to the fluorimeter for FI measurement. As XOD exhibits fluorescence quenching capabilities at 520 nm, DHR123 fluorescent emission was determined at a wavelength of 535 nm as opposed to the more conventional 520 nm in order to avoid any interference whilst maintaining sufficient sensitivity of the FI readings.

### 2.2.6 FACS analysis of UVA irradiated HaCaT cells

HaCat cells were treated with trypsin, washed and re-suspended in PBS. Half of the cells were incubated with either DCF-DA for 30 min or DHR123 for 20 min in complete darkness and designated as 'pre-UV loaded dye'. All the cells were then irradiated with 10 $Jcm^{-2}$ UVA during which the cells were gently agitated every 5 min to prevent adherence (control samples were treated identically but heavily masked to prevent exposure to UVA). The remaining unstained cells (i.e. the other half of the cells) were incubated with either DCF-DA or DHR123 as described above and designated as 'post-

UV loaded dye'. All cells were then washed and re-suspended in PBS with 10 mm propidium iodide and incubated at room temperature for 5min prior to FACS analysis using the FL1 channel of a BD FacScan (Becton Dickinson, UK). Analysis was performed on PI negative cells using Venture 1 software (Applied Cytometry Inc., TX).

### 2.2.7 Fluorimetric analysis of UVA irradiated HaCaT cells

HaCaT cells were plated into a white 96-well plate (Corning, VWR, Lutterworth, Leicestershire, UK) at a density of 5000 cells per well and were incubated overnight to allow adherence to the culture flask. Cells investigated as 'pre-loaded' with dyes were incubated as for FACS analysis prior to UVA irradiation. A sub-sample of 'pre-loaded' cells was heavily masked to serve as UVA negative controls. All cells were washed and covered with PBS for the duration of irradiation with 10 $Jcm^{-2}$ UVA. The remaining unstained sample cells (i.e. the 'post-UVA loaded' cells) were incubated with the dyes as previously described. The plate was then loaded into the fluorimeter for FI measurement.

## 2.3 Results

### 2.3.1 Effect of diluent upon fluorescence of DHR123 and DCF-DA

The data in Figure 2.1 investigates the question of whether the experimental diluent (e.g. culture medium/buffer) interacts with the fluorescent dyes and consequently modifies their response to ROS. At time zero, increased fluorescence was observed in solutions of DHR123 and DCF-DA diluted in plain and complete DMEM when compared with dye diluted in PBS. When exposed to UVA, DCF-DA in plain DMEM exhibited a striking increase in FI within 1 Jcm$^{-2}$ of UVA exposure. The increase in fluorescence continued for the duration of the UVA exposure, resulting in a 10-fold increase in fluorescence at a 10 Jcm$^{-2}$ dose of UVA. In contrast, other combinations of dyes and diluents did not provide such an amplified response. For example, DCF-DA in complete DMEM exhibited an ~2-fold increase in FI following 10 Jcm$^{-2}$ UVA. Interestingly, a very similar profile of dose curves was observed for the UVA irradiation of DHR123 in both plain and complete DMEM where again an ~2-fold increase in FI was recorded following 10 Jcm$^{-2}$ UVA. In complete contrast to the behaviour of the dyes in plain and complete DMEM, the dyes diluted in PBS exhibited only a slight increase in FI when exposed to UVA.

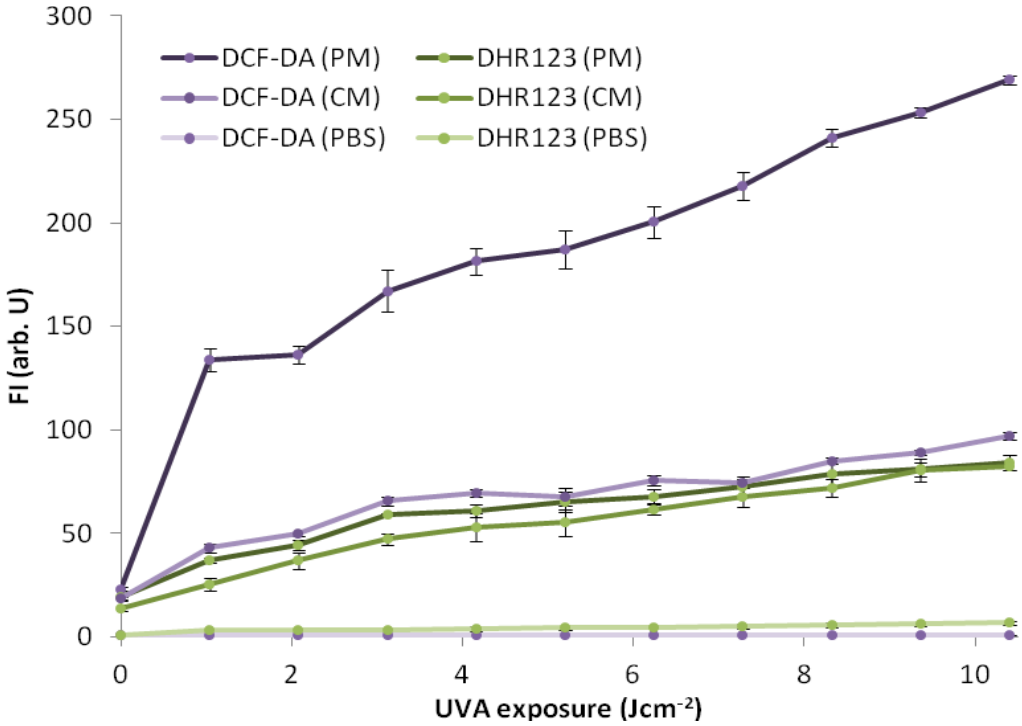

**Figure 2.1:** Differential FI responses of DCFDA and DHR123 diluted in PBS, plain DMEM (PM) or complete DMEM (CM) resulting from increasing UVA exposure. FI was measured using a fluorimeter as described in Materials and Methods. Data presented ±standard error of the mean, n=6.

### 2.3.2 Effect of UVA upon the emission profiles of DHR123 and DCF-DA

The data in Figure 2.2 was generated to more fully investigate the changes in the emission spectra of DHR123 and DCF-DA after exposure to UVA. DHR123 exhibited a marked increase in fluorescence emission between λ520-650nm, with all values increasing by ~2 fold. Conversely, the fluorescence profile exhibited by DCF-DA is almost completely quenched after exposure to UVA.

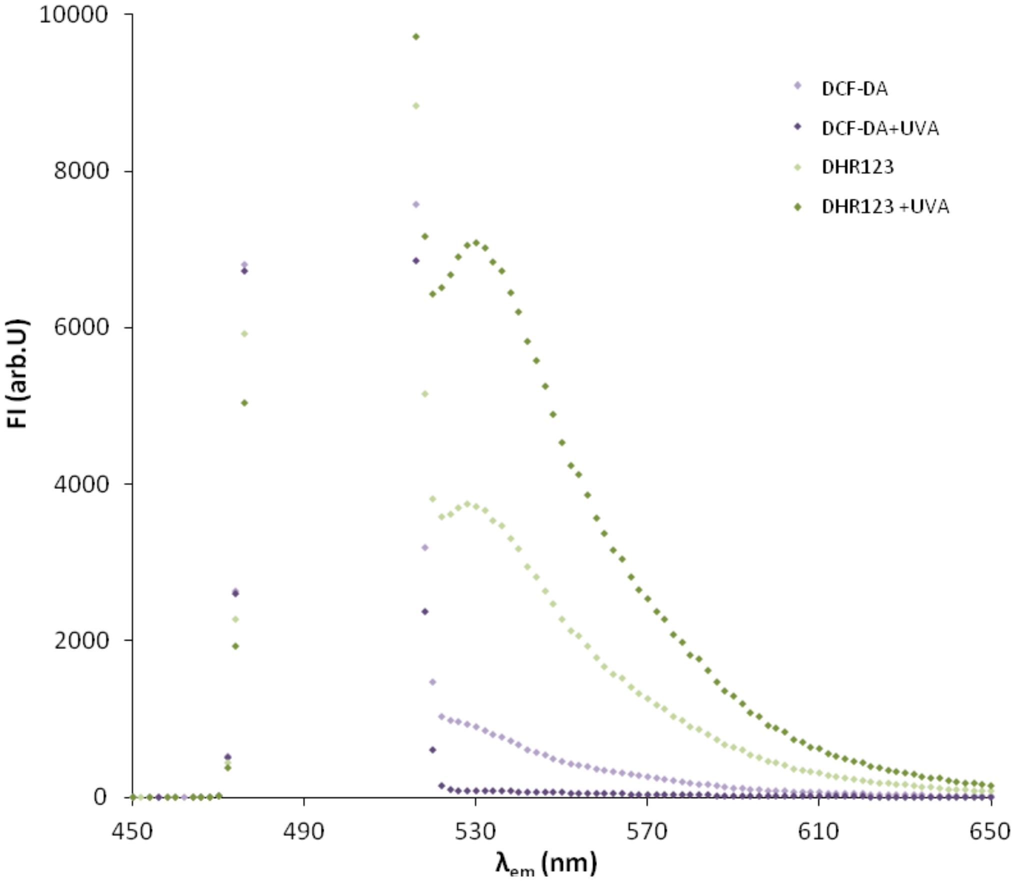

**Figure 2.2:** Differential emission scan responses from both DHR123 and DCF-DA with and without UVA exposure. The data is representative of individual sample FI scans.

### 2.3.3 Effect of UVA pre-treatment upon the response of DHR123/DCF-DA

In order to address the other two questions of the study (namely does UVA irradiation affect the fluorescence of DHR123 and DCF-DA and, if so, is this effect independent of ROS interaction and does it alter dye sensitivity for ROS?), a previously established system for the generation of $H_2O_2$ and $O_2^-$ using xanthine and XOD was used to determine the ROS responses of DHR123 and DCF-DA both in the absence and presence of UVA pre-treatment. The study took into consideration any effects of xanthine or XOD upon the dyes (see methods). The data in Figure 2.3 clearly show that DCF-DA exhibits a decreased response to xanthine/XOD generated ROS following UVA irradiation when compared with the absence of any UVA pre-treatment. There was a significant difference in the response ($p<0.005$) between the irradiated and non-irradiated samples at all enzyme concentrations (taking into account the absolute FI for the XOD free controls in which the irradiated DCF-DA samples exhibited higher absolute FI values than the non-irradiated counter parts). The inset in Figure 2.3 emphasizes the fact that both UVA irradiated and non-irradiated sample sets show a similar trend of DCF-DA response to the gene rated ROS (although the amplitude is more pronounced in the non-irradiated dataset, implying an increased response to ROS in the absence of any UVA pre-treatment). The data in Figure 2.4 represents the same experimental protocol used in Figure 2.3 with the exception that the dye used was DHR123 rather than DCF-DA. In a similar fashion to the observations reported in Figure 2.3, DHR123 exhibited a decreased response to xanthine/XOD generated ROS following UVA irradiation when compared with the absence of any UVA pre-treatment. Again, taking into account the absolute FI for the XOD free controls (in which the irradiated DHR123 samples exhibited higher absolute FI values than the non-irradiated counterparts), there was a significant difference between irradiated and non-irradiated dye, most notably at 0.5 and 2.5 Uml$^{-1}$ XOD ($p<0.0001$) (the trend was not observed at the lowest XOD concentration for which similarly low responses were exhibited). The inset in Figure 2.4 emphasizes the decreased response of the dye following UVA pretreatment, although the actual profile of the DHR123 response was different to that observed for DCF-DA (i.e. UVA appeared to decrease the response of DHR123 more than DCF-DA). Despite this issue, all the data displayed in Figure 2.3 and Figure 2.4 clearly suggested that UVA pre-treatment had a compromising effect on the ability of the dyes to respond reliably to ROS generated in a cell-free system.

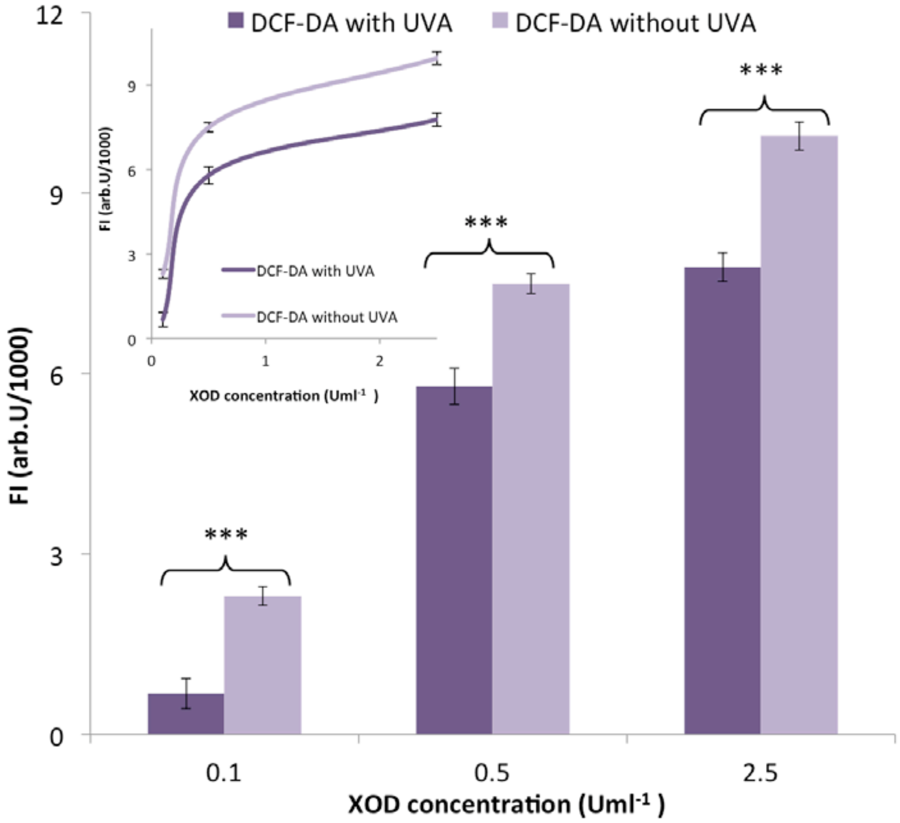

**Figure 2.3:** XOD dose-dependent fluorescence of DCF-DA with or without UVA pre-treatment (10 Jcm$^{-2}$) in a cell-free system. FI was determined as described in section 2.2.6. Significant difference between data sets denoted by *** ($p < 0.001$) and **($p < 0.01$) as determined by one way ANOVA. Data presented ±standard error of the mean, n=8.

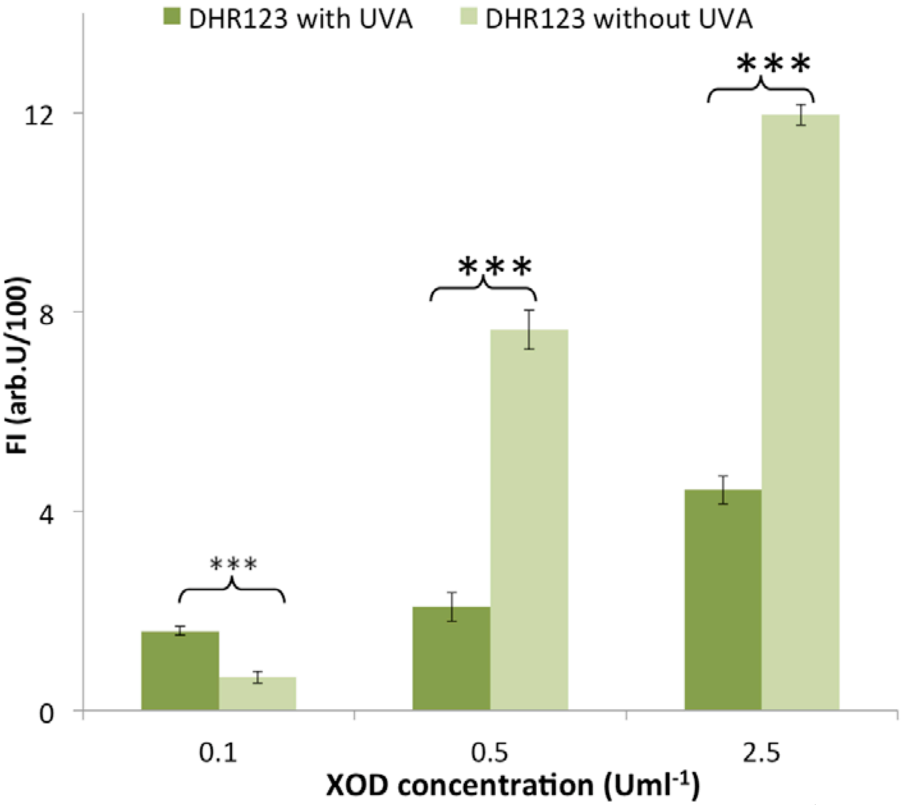

**Figure 2.4:** XOD dose-dependent fluorescence of DHR123 with or without UVA pretreatment (10 Jcm$^{-2}$) in a cell-free system. FI was determined as described in 2.2.6. Significant difference between data sets denoted by *** ($p$<0.001) as determined by one way ANOVA. Data presented standard error of the mean, $n$=8.

### 2.3.4 *In vitro* methods using DHR123/DCF-DA as probes for UVA-induced oxidative stress

The next question to address was whether UVA treatment had a compromising effect on the ability of the dyes to respond reliably to ROS generated *in vitro* from cultured human skin cells when compared with the cell-free environment as described in Figures 2.3 and 2.4. Additionally, in order to study the dynamics of the UVA effect on the dyes, HaCaT cells were loaded with DHR123 or DCF-DA either before or after exposure to 10 $Jcm^{-2}$ UVA and the resulting changes in FI were detected using fluorimetry. A significantly greater UVA induced FI was observed in those HaCaT cells loaded with DHR123 or DCF-DA prior to UVA treatment (i.e. pre-UVA loaded dye) compared with loading the cells with the dye post-UVA treatment (i.e. post-UVA loaded dye). Control fluorescence data from non-irradiated HaCaT cells were used to normalize the FI in both sample sets. Even though the UVA treatment was sub-lethal to the HaCaT cells, a further experiment was performed in order to account for any confounding effects due to cell death or lack of cell viability. This involved flow cytometric analysis of cells double labelled with the ROS dye and propidium iodide to indicate any dead cells which might have taken up the dye and would therefore contribute to the overall FI reading. Table I shows the results of the flow cytometric measurement of HaCaT cells loaded with both dyes either before or after exposure to 10 $Jcm^{-2}$ UVA. The results of this experiment confirm the data displayed in Figure 2.5 by demonstrating a significantly greater UVA-induced FI in those HaCaT cells loaded with DHR123 or DCF-DA prior to UVA treatment (i.e. pre-UVA loaded) compared with loading the cells with the dye post-UVA treatment (i.e. post-UVA loaded) ($p<0.005$ (DHR123), $p<0.05$ (DCF-DA)). As in Figure 2.5, control fluorescence data from non-irradiated HaCaT cells were used to normalize the FI in both sample sets.

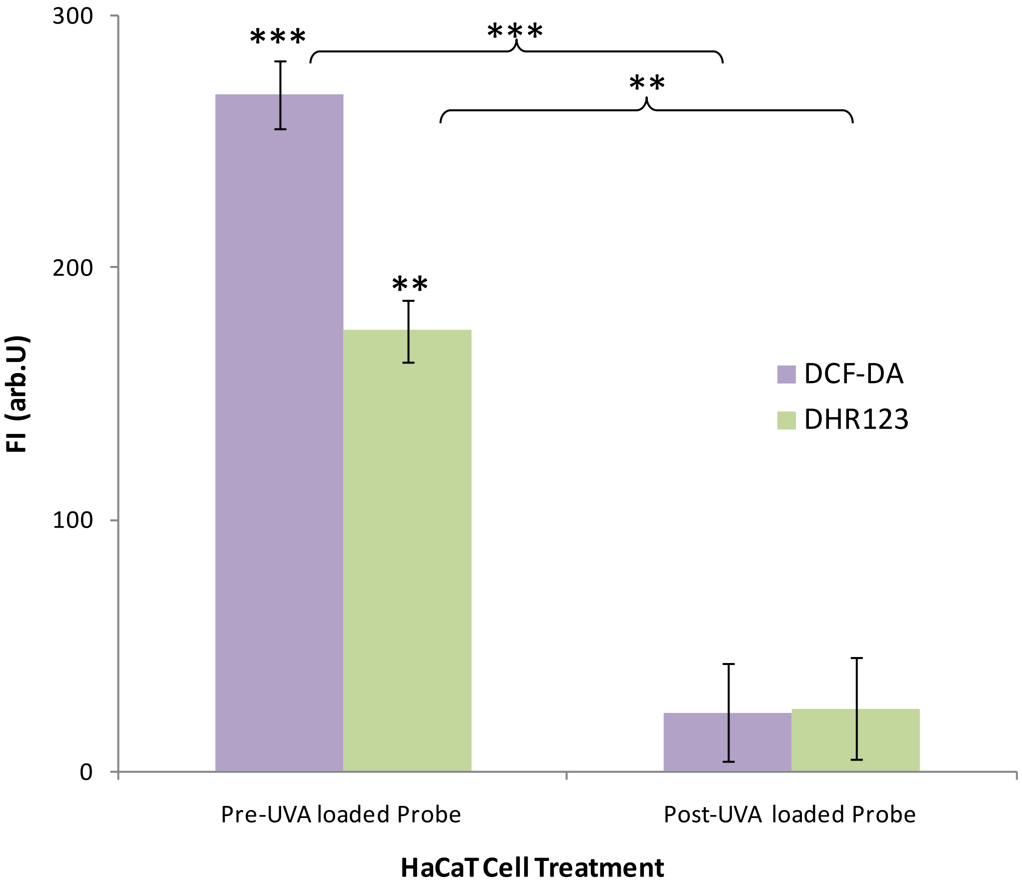

**Figure 2.5:** Fluorimeter defined loading dependent responses by DCF-DA and DHR123 to UVA induced ROS production in HaCaT cells. Probes were loaded into HaCaT cells pre or post 50 minutes UVA exposure and FI was quantified as described in section 2.2.6. The data is presented ± standard error of the mean, n=3.

| | DHR123 | | DCF-DA | | |
|---|---|---|---|---|---|
| | $\bar{\chi}$ | σ | $\bar{\chi}$ | σ | "p" value |
| Pre UVA loaded | **386.79** | 2.87 | **1115.31** | 147.81 | 0.002 |
| Post UVA loaded | **78.54** | 1.58 | **47.37** | 50.97 | 0.1 |
| "p" value | 0.00002 | | 0.002 | | |

**Table 2.1:** FACS-defined, loading-dependent responses of DCF-DA and DHR123 to UVA-induced ROS production *in vitro*. HaCaT cells were loaded with DHR123 or DCF-DA either before or after exposure to 10 Jcm$^{-2}$ UVA with the resulting changes in FI quantified in living cells (i.e. propidium iodide negative cells) using flow cytometry as described in section2.2.7. The data is presented ± standard error of the mean, n=3.

## 2.4 Discussion

This study set out to address three questions. The first was whether the experimental diluent (e.g. culture medium/buffer) interacted with the dyes thereby modifying their response to ROS? By exposing the native dye to increasing UVA exposure in a range of media, Figure 2.1 shows that the diluent used during irradiation will impact upon the magnitude of fluorescence determined by both DHR123 and DCF-DA. Halliwell and Long (Long and Halliwell 2009) have shown that components of DMEM can catalyse the production of $H_2O_2$ on the addition of phenolic compounds such as epigallocatechin gallate. This may provide some indication as to why dyes such as DHR123 and DCF-DA, themselves phenolic compounds, may interact with components of DMEM and were observed to exhibit increased FI. Spontaneous oxidation of the dyes has been demonstrated to be in the order of ~0.02%/min (Royall and Ischiropoulos 1993) in a ROS free system, thus the observed changes in FI are likely to originate from the generation of an oxidative species. Riboflavin is a key component of DMEM and not only has it been shown to produce ROS it has also been identified as an intracellular source of $O_2^{-}$ upon exposure to sunlight (Cunningham *et al*. 1985; Wang and Nixon 1978). The inherent redox activity of riboflavin, which is known to interfere with cytotoxicity assays (Granzow *et al*. 1995) may also play a part in the interaction between the media content and the ROS sensing dyes.

A number of studies have demonstrated that DMEM, when exposed to ambient light such as that from a non-UV safety cabinet bulb, can produce ROS catalysed by trace metal ions such as iron, magnesium, sodium, potassium and calcium (Cunningham *et al*. 1985; Valko *et al*. 1999; Wang and Nixon 1978). These metal ions also accelerate ROS production through the auto-oxidation of glucose. Mammalian serum albumins such as those present in FCS have been shown to exhibit non-specific binding properties with a wide range of different ions including $Cu^{2+}$, $Cd^{2+}$, $Ni^{2+}$ and $Zn^{2+}$ due to the N-terminal 3 residues that form a strong square planar binding site (Bal *et al*. 1998; Sadler *et al*. 1994). Other studies have suggested that there is more than one metal specific binding site on serum albumin (Valko *et al*. 1999; Zgirski and Frieden 1990). This is in keeping with the difference in dye fluorescence observed in plain DMEM compared with complete DMEM as displayed in Figure 2.1. This difference in FI levels may be attributed to the presence of FCS in the media. For example, in complete DMEM non-specific interactions between serum protein and the metal ions may attenuate the catalysis of peroxide generation (and decrease the production of hydroxyl radicals from $H_2O_2$ catalysed by transition metals such as iron and copper via the Fenton reaction (Batandier *et al*. 2002)) thereby leading to reduced FI as shown in Figure 2.1. However, this is clearly not the entire explanation as there was greater amplitude of response with DCF-DA compared with DHR123 which may in part be related to additional structural or stochastic interactions. In complete contrast to the behaviour of the dyes in plain and complete DMEM, the dyes diluted in PBS exhibited only a slight increase in FI when exposed to UVA. As shown by the $\lambda_{em}$ scan data presented in Figure 2.2, clear fluorescence emission peaks were observed both pre- and post-UVA irradiation of DHR123 in PBS. The entire FI emission profile of DHR123 appears to have increased ~2 fold between 520-650nm, indicating possible photo-activation of the dye. Conversely the opposite effect is observed after irradiation of DCF-DA with complete attenuation of FI emission and is corroborated by the same pattern of changes in Figure 2.2. The simple composition and lack of any metal ions in PBS maintains a 'neutral' environment for the irradiation of dyes thereby removing the opportunity for any exacerbation of fluorescence by the presence of such components in DMEM.

This effect was more pronounced with DHR123 than DCF-DA. It appears therefore that the dye may be excited and sensitised directly by the UVA light, resulting in a decreased proportion of the non-excited state remnant of the dye being available for interaction with the ROS generated by the xanthine/XOD system. This reduced capacity to interact with any XOD generated ROS would explain the decreased ability of the dyes to sense ROS following UVA treatment as there was a smaller residue of non-reduced dye able to respond to the XOD generated ROS. Hence, as XOD was introduced to the dye in increasing concentrations, only a relatively small change in FI was observed in the irradiated dye compared with non-irradiated dye. Against the background of this 'desensitisation-like effect' exhibited by the two dyes, it is interesting to note that there was a different profile of response between DCF-DA and DHR123 and again this may depend in part on additional structural or stochastic interactions. This 'desensitisation-like effect' is important as it suggests that the increase in fluorescence induced by UVA treatment of DHR123, and to a lesser extent DCF-DA, could in fact be masking the more subtle but nevertheless key responses in ROS mediated pathways and events.

Whilst there is little detailed published literature on the photo-stability of DHR123 and DCF-DA, particularly in relation to UVA, this study provided evidence that UVA irradiation increased conversion of DHR123 to R123 and DCF-DA to fluorescent DCF (dichorofluorescine; two hydrogen atoms are lost) in a cellular ROS-independent manner. This has important implications for those studies requiring the use of a fluorescent dye such as DCF-DA and DHR123 when UVA is the inducer for oxidative stress in the cells. Subtle differences in cellular ROS production (which may in fact represent significant events in cellular signalling responses) are likely to be masked by an exaggerated response of dyes to UVA especially when diluted in DMEM, likewise, the effects of largely cytotoxic stimuli may indeed be disproportionately reported and thus overestimated. This may be particularly important if such dyes are to be loaded into cells prior to UV exposure. The data presented in this study suggests that such dyes should be loaded preferably in PBS and post-UV irradiation. However, loading dyes after UV exposure may cause a trade-off in measuring the time course of a response when ROS production is measured after the initial UV-induced burst of ROS. If loaded pre-UV irradiation, then adequate control conditions must be included to account for the potential confounding effects reported in this work.

## 2.5 References

Afzal, M., Matsugo, S., Sasai, M., Xu, B., Aoyama, K., Takeuchi, T., 2003. Method to overcome photoreaction, a serious drawback to the use of dichlorofluorescin in evaluation of reactive oxygen species. Biochemical & Biophysical Research Communications 304(4), 619-624.

Aitken, G.R., Henderson, J.R., Chang, S.C., McNeil, C.J., Birch-Machin, M.A., 2007. Direct monitoring of UV-induced free radical generation in HaCaT keratinocytes. Clinical Experimental Dermatology 32(6), 722-727.

Bal, W., Christodoulou, J., Sadler, P.J., Tucker, A., 1998. Multi-metal binding site of serum albumin. Journal of Inorganic Biochemistry 70(1), 33-39.

Barbacanne, M.A., Souchard, J.P., Darblade, B., Iliou, J.P., Nepveu, F., Pipy, B., Bayard, F., Arnal, J.F., 2000. Detection of superoxide anion released extracellularly by endothelial cells using cytochrome *c* reduction, ESR, fluorescence and lucigenin-enhanced chemiluminescence techniques. Free Radical Biology & Medicine 29(5), 388-396.

Batandier, C., Fontaine, E., Keriel, C., Leverve, X.M., 2002. Determination of mitochondrial reactive oxygen species: methodological aspects. Journal of Cell & Molecular Medicine 6(2), 175-187.

Chang, S.C., Pereira-Rodrigues, N., Henderson, J.R., Cole, A., Bedioui, F., McNeil, C.J., 2005a. An electrochemical sensor array system for the direct, simultaneous *in vitro* monitoring of nitric oxide and superoxide production by cultured cells. Biosensors & Bioelectronics 21(6), 917-922.

Chang, S.C., Rodrigues, N.P., Zurgil, N., Henderson, J.R., Bedioui, F., McNeil, C.J., Deutsch, M., 2005b. Simultaneous intra- and extracellular superoxide monitoring using an integrated optical and electrochemical sensor system. Biochemical & Biophysical Research Communications 327(4), 979-984.

Cheeseman, K.H., 1993a. Mechanisms and effects of lipid peroxidation. Molecular Aspects of Medicine 14(3), 191-197.

Cheeseman, K.H., 1993b. Tissue injury by free radicals. Toxicology & Industrial Health 9(1-2), 39-51.

Chen, X., Zhong, Z., Xu, Z., Chen, L., Wang, Y., 2',7'-Dichlorodihydrofluorescein as a fluorescent probe for reactive oxygen species measurement: Forty years of application and controversy. Free Radical Research 44(6), 587-604.

Cui, X.-L., Ding, Y., Alexander, L.D., Bao, C., Al-Khalili, O.K., Simonson, M., Eaton, D.C., Douglas, J.G., 2006. Oxidative signaling in renal epithelium: Critical role of cytosolic phospholipase A2 and p38SAPK. Free Radical Biology & Medicine 41(2), 213-221.

Cunningham, M.L., Krinsky, N.I., Giovanazzi, S.M., Peak, M.J., 1985. Superoxide anion is generated from cellular metabolites by solar radiation and its components. Journal of Free Radicals in Biology & Medicine 1(5-6), 381-385.

Foyer, C.H., Noctor, G., 2005. Redox homeostasis and antioxidant signaling: a metabolic interface between stress perception and physiological responses. Plant Cell 17(7), 1866-1875.

Gniadecki, R., Thorn,T

Granzow, C., Kopun, M., Krober, T., 1995. Riboflavin-mediated photosensitization of vinca alkaloids distorts drug sensitivity assays. Cancer Research 55(21), 4837-4843.

Grzelak, A., Rychlik, B., Bartosz, G., 2001. Light-dependent generation of reactive oxygen species in cell culture media. Free Radical Biology & Medicine 30(12), 1418-1425.

Halliwell, B., Gutteridge, J., 1984. Lipid peroxidation, oxygen radicals, cell damage and antioxidant therapy. The Lancet 105, 1396-1397.

Henderson, J.R., Swalwell, H., Boulton, S., Manning, P., McNeil, C.J., Birch-Machin, M.A., 2009. Direct, real-time monitoring of superoxide generation in isolated mitochondria. Free Radical Research 43(9), 796-802.

Kaczara, P., Sarna, T., Burke, J.M., 2010. Dynamics of $H_2O_2$ availability to ARPE-19 cultures in models of oxidative stress. Free Radical Biology & Medicine 48(8), 1064-1070.

Long, L.H., Halliwell, B., 2009. Artefacts in cell culture: Pyruvate as a scavenger of hydrogen peroxide generated by ascorbate or epigallocatechin gallate in cell culture media. Biochemical & Biophysical Research Communications 388(4), 700-704.

Mahns, A., Melchheier, I., Suschek, C.V., Sies, H., Klotz, L.O., 2003. Irradiation of cells with ultraviolet-A (320-400 nm) in the presence of cell culture medium elicits biological effects due to extracellular generation of hydrogen peroxide. Free Radical Research 37(4), 391-397.

McNeil, C.J., Manning, P., 2002. Sensor-based measurements of the role and interactions of free radicals in cellular systems. Reviews in Molecular Biotechnology. 82, 443-455.

Royall, J.A., Ischiropoulos, H., 1993. Evaluation of 2',7'-dichlorofluorescin and dihydrorhodamine 123 as fluorescent probes for intracellular $H_2O_2$ in cultured endothelial cells. Archives of Biochemistry & Biophysics 302(2), 348-355.

Sadler, P.J., Tucker, A., Viles, J.H., 1994. Involvement of a lysine residue in the N-terminal $Ni^{2+}$ and $Cu^{2+}$ binding site of serum albumins. Comparison with $Co^{2+}$, $Cd^{2+}$ and $Al^{3+}$. European Journal of Biochemistry 220(1), 193-200.

Soh, N., Soh, N., 2006. Recent advances in fluorescent probes for the detection of reactive oxygen species. Analytical & Bioanalytical Chemistry 386(3), 532-543.

Tammeveski, K., Tenno, T.T., Mashirin, A.A., Hillhouse, E.W., Manning, P., McNeil, C.J., 1998. Superoxide electrode based on covalently immobilised cytochrome *c*: Modelling studies. Free Radical Biology & Medicine 25(8), 973-978.

Traverso, J.A., Vignols, F., Chueca, A., 2007. Thioredoxin and redox control within the new concept of oxidative signaling. Plant Signal Behavior 2(5), 426-427.

Valko, M., Morris, H., Mazur, M., Telser, J., McInnes, E.J.L., Mabbs, F.E., 1999. High-affinity binding site for copper(II) in human and dog serum albumins (an EPR Study). The Journal of Physical Chemistry B 103(26), 5591-5597.

Van Lente, F., 1993. Free radicals. Analytical Chemistry 65(12), 374-377.

Wang, R.J., Nixon, B.T., 1978. Identification of hydrogen peroxide as a photoproduct toxic to human cells in tissue-culture medium irradiated with 'daylight' fluorescent light. *In vitro* 14(8), 715-722.

Yuan, H., Perry, C.N., Huang, C., Iwai-Kanai, E., Carreira, R.S., Glembotski, C.C., Gottlieb, R.A., 2009. LPS-induced autophagy is mediated by oxidative signaling in cardiomyocytes and is associated with cytoprotection. American Journal of Physiology: Heart & Circulatory Physiology 296(2), H470-479.

Zgirski, A., Frieden, E., 1990. Binding of Cu(II) to non-prosthetic sites in ceruloplasmin and bovine serum albumin. Journal of Inorganic Biochemistry 39(2), 137-148.

# Chapter 3. Development and characterisation of optical techniques for intracellular analysis of ROS production

## 3.1 Introduction

As previously discussed in Chapter 2, the various roles of ROS within cell systems encompass signal transduction, detoxification and cell communication amongst many others (Craig *et al*. 2009; Gautam *et al*. 2006; Kurauchi *et al*. 2009). The dysregulation or overproduction of such highly reactive molecules has been identified as a progenitor of a range of disease states where DNA damage, progressive cell death or modulated cell communication are key features (Hartley *et al*. 1994; Langer *et al*. 2008; Liu *et al*. 2009). Monitoring the intracellular production of ROS is therefore of great interest to a range of investigations regarding the pathophysiology of disease states, however the high inter-reactivity of ROS along with their short half lives makes direct and real-time intracellular monitoring very difficult. ROS-sensitive nanosensors were recently developed to overcome the difficulties associated with fluorescent intracellular monitoring.

The use of fluorescent dyes such as DHR123 and DCF-DA to evaluate dynamic intracellular ROS generation is widespread (Chang *et al*. 2005; Henderson and Chappell 1993; Tobi *et al*. 2000; Zurgil *et al*. 2006). The inherent difficulties surrounding the use of such dyes were highlighted previously in Chapter 2 and have been reported extensively in recent literature (Boulton *et al*. 2011; Chen *et al*. 2010). Naked dyes introduced to the intracellular environment are often prone to auto-oxidation and interaction with endogenous proteins that cause variation and inaccurate fluorescent responses (Graber *et al*. 1986). The ROS-responsive dye DCF-DA has also been shown to generate $O_2^-$ through the formation of the semiquinone $DCF^{\bullet -}$ during oxidation and subsequent reduction of $O_2$. The oxidation of DCF-DA in this manner is thought to be a consequence of interaction with $H_2O_2$/peroxidise enzyme intermediates (Rota *et al*. 1999). The nanosensor matrix prevents the interaction of the entrapped dyes with large intracellular proteins and their intermediates. This may improve the reliability of the observed fluorescent response to ROS (Park *et al*. 2003; Xu *et al*. 2002).

Polyacrylamide 'PEBBLE' nanosensors have been developed for many analytes including calcium, pH and oxygen. (Buck *et al*. 2004; Coupland *et al*. 2009; Webster *et al*. 2005) There have been many different types of PEBBLE nanosensors as mentioned in Chapter 1, including those fabricated from sol-gel, ormosil, and silica (Clark *et al*. 1999; Hammond *et al*. 2008; Koo *et al*. 2004). The nanosensors reported in this study were fabricated from polyacrylamide due to the bioinert nature of the final nanoscale matrix and previously demonstrated high dye retention properties previously reported (Buck *et al*. 2004). The development of a novel ROS-sensitive nanosensor that comprised a ROS-responsive and a stable reference dye co-localised within a nanoscale polyacrylamide matrix was recently reported by the group (Henderson *et al*, 2009). The polyacrylamide nanosensor platform confers many benefits over the use of free dyes when monitoring analytes intracellularly. As previously mentioned the interaction of the encapsulated dyes with endogenous macromolecules is prevented through size exclusion by the polymer matrix pores, reducing the opportunity for non-specific oxidation of dyes by endogenous macromolecules and the risk of 'false positive' results (Sumner *et al*. 2002) The entrapment of dyes within the bioinert polyacrylamide matrix also protects cells from the often cytotoxic effects of long term exposure to native dyes (Buck *et al*. 2004). These properties, alongside the negligible volume of the nanosensors once internalised, also promotes the long term monitoring of dynamic ROS flux that is currently not possible with free dyes.

The cells used in this study were from the phagocytic rat alveolar macrophage line NR8383. This cell line was chosen as it has been reported to be a robust model of cellular ROS generation which was required to facilitate to characterisation of the nanosensors. The $O_2^-$ burst associated with macrophage cells has been extensively investigated and can be stimulated in a dose dependent manner through the application of phorbol-12-myristate-13-acetate (PMA) (Amatore *et al*. 2008; Giron-Calle and Forman 2000; Rinna *et al*. 2006). The natural process of phagocytosis exhibited by these cells can also be exploited as a nanosensor delivery mechanism, allowing uptake of the nanosensors as a passive consequence of culture medium doping. Although the nanosensors will be reporting ROS generation from within a phagosome, the exploitation of a natural process to deliver the nanosensor allows the optimisation process to be broken down into simple stages, reducing the risk of data misinterpretation inherent in a more complex, multivariate investigation.

The nanosensors reported in this study were first optimised in terms of the ROS responsive component included. Chapter 2 highlighted the different modes of action of both DHR123 and DCF-DA and as a consequence of this work both dyes were investigated within the nanosensor platform. Co-localisation of an analyte responsive ‘signal’ dye and a stable, non-responsive ‘reference’ dye facilitates ratiometric measurement of analytes once calibrated and internalised by cells. Although ratiometric measurements were not made in the group’s previous study (Henderson *et al*. 2009), the current investigation built upon this work to monitor PMA induced ROS generation in NR8282 macrophage cells in a ratiometric manner. The fabrication and internalisation of ROS sensitive nanosensors was optimised and proven in rat alveolar macrophage cell line NR8383.  Delivery to the intracellular environment was achieved using a cell-mediated technique that allowed the cells to phagocytose nanosensors introduced to the extracellular environment. The compatibility of ROS sensitive free dyes with extracellular ROS sensitive electrodes has already been demonstrated. The successful development of a ratiometric intracellular nanosensor for ROS would facilitate the characterisation of a fully integrated platform for the long-term semi-quantitative analysis of ROS generation within the external and internal environments of cell models of disease.

## 3.2 Materials and methods

### 3.2.1 Cell culture and preparation

Rat alveolar macrophage cell line NR8383 was cultured in phenol red free Knight's modified Ham's F12 medium (Ham's F12K) supplemented with 10% foetal calf serum (FCS) and 1% non-essential amino acids (NEAA). Cells were maintained in a 5% $CO_2$ at 37.5˚C humidified atmosphere and were grown to ~70% confluence before testing. Macrophages underwent no more than 6 passages over the course of experimentation.

### 3.2.2 Reactive oxygen species sensitive nanosensor fabrication

Nanosensors comprising ROS-sensitive dye DHR123 and stable reference dye AlexaFluor568 co-localised within a porous polyacrylamide matrix were fabricated using a method adapted from a previously described technique (Clark *et al*. 1999). An organic phase was prepared by doping 42 ml hexane with the surfactants sulphododecylsuccinate (SDS) and Brij30 in order to control nanosensor diameter and pore size. An aqueous solution of monomers was prepared by dissolving powdered acrylamide (3.8 M) and N,N-methylenebisacrylamide (0.5 M) in 2 ml water. DHR123 and AlexaFluor568 were added to the monomer solution to a concentration of 100 $\mu g ml^{-1}$ immediately prior to dispersal within the hexane/surfactant mixture to form a reverse phase microemulsion. Whilst under constant stirring, polymerisation was initiated by the addition of 15 µl TMED and 30 µl 10% APS solution. Polymerisation was continued for at least 2 h. Hexane was rotovaporated from the emulsion to yield nanosensor-containing slurry. Washing in absolute ethanol removed the surfactants from the nanosensors that were finally retrieved from suspension using a vacuum filtration system in conjunction with 20nm pore-size Whatman anodisc filters. Dry nanosensors were stored at -20°C and protected from light by wrapping with aluminium foil. This method of fabrication yielded nanosensors with average hydrodynamic radii of 18nm (±1nm) in monomodal distribution (Henderson *et al*. 2009).

### 3.2.3 Nanosensor calibration

A 1 $mg ml^{-1}$ nanosensor solution was made using 5mM xanthine in PBS. This solution was aliquoted in triplicate to a black walled 96-well microplate (Corning, UK). An

Infinite M200 fluorimeter (Tecan, UK) was used to make all fluorescence measurements form the nanosensors and was used in conjunction with associated Magellan control and data analysis software. The samples were treated with XOD in a range of concentrations from 0-25 Uml$^{-1}$ then placed in the fluorimeter for measurement using the following settings; DHR123 FI: $\lambda_{ex}$ = 488nm, $\lambda_{em}$= 525nm; AlexaFluor568 FI: $\lambda_{ex}$ = 578nm, $\lambda_{em}$= 603nm.

### 3.2.4 Cell mediated nanosensor delivery

During all stages of preparation and internalisation the sensors were protected from light-induced dye autoxidation as far as possible by covering containers with aluminium foil. A 100 mgml$^{-1}$ nanosensor solution was prepared in PBS then diluted as necessary directly into routine culture flasks of the macrophage cells. Overnight incubation ensured that sufficient nanosensors were phagocytosed to allow fluorescence measurement. Prior to use in experimentation, the cells were rinsed thoroughly in pre-warmed PBS to remove any sensors that remained in the medium.

### 3.2.5 MTT cell viability assay

Macrophage cells were seeded into a clear walled 96-well microplate at 1000 cells per well and incubated in routine culture conditions for 3 h to allow cell attachment. Samples of cells in triplicate were treated with nanosensors by replacing the medium with 5, 10, or 20 mgml$^{-1}$ nanosensors in culture medium. Negative control samples received only fresh medium with no nanosensor exposure. The cells were incubated with their respective treatment overnight to ensure an uptake representative of standard internalisation procedure to be employed in future work. The following morning the medium was aspirated from the cells and was replaced with 5 mgml$^{-1}$ MTT solution in PBS. MTT exposure continued for 2 h in routine culture conditions before the cells were lysed and any accumulated metabolite solubilised by replacing the solution in every well with 100 µl DMSO and agitating the plate on a shaker for 5 min. The optical density of each well was read using a SpectraMax 180 plate reader. The data was expressed as an average percentage of the nanosensor untreated control cells.

### 3.2.6 Extracellular amperometric nitric oxide and hydrogen peroxide monitoring

NR8383 macrophage cells were seeded into 3cm diameter plastic cell culture dishes at a concentration of ~$1x10^6$ cells.$ml^{-1}$. The medium of half the dishes was doped with 5 $mgml^{-1}$ ROS-sensitive nanosensors while the other half did not receive any nanosensor treatment. The cells were allowed to phagocytose the nanosensors overnight. The following morning, the medium of the dishes was replaced. A commercially available Apollo 4000 free radical analyser (World Precision Instruments, USA) was employed to amperometrically detect extracellular $H_2O_2$ and $NO^•$ flux in response to PMA stimulation. The $NO^•$ and $H_2O_2$ selective electrodes were positioned as close to the cells as possible. The recording of current values for both analytes was commenced and upon the observation of a stable baseline either 1 or 5 $\mu gml^{-1}$ PMA was aliquoted directly upon the cells nearest the electrodes. Any changes in current were recorded for at least 200 s following PMA addition. This was repeated 3 times each for both nanosensor treated and untreated cell populations, after which the peak current response for each trace was identified and averaged over the 3 repeated challenges.

### 3.2.7 Measurement of PMA-induced extracellular ROS flux.

Cells loaded with nanosensors were seeded into a 24 well plate containing 16mm diameter glass coverslips and allowed to attach for at least 3 h. To monitor the cells the coverslips were removed from the plate, rinsed and inverted over a drop of PBS onto a microscope slide taking care to avoid the formation of air bubbles. Inverting the coverslip permitted the use of an oil immersion objective to take close images of the cells as necessary. Images representing the individual dyes were acquired separately using a Nikon Eclipse 80*i* Epi-Fluorescence microscope in conjunction with Nikon BR image acquisition and analysis software. Excitation of the dyes was achieved using a 50W Hg lamp in conjunction with relevant filter sets. DHR123 was observed using a B-2E/C filter ($\lambda_{ex}$= 465-495 nm, $\lambda_{em}$= 515-555 nm) while AlexaFluor568 was observed using a CY3 HYQ filter ($\lambda_{ex}$= 530-560 nm, $\lambda_{em}$= 573-648 nm). Minimal exposure times were used to reduce the impact of photo-bleaching upon the samples. Some 5 $\mu gml^{-1}$ PMA was added and two images of the cells (one with each filter specified above) were taken immediately after in quick succession to ascertain an initial FI ratio. Image acquisition was repeated as every 5 min for 20 min thereafter.

## 3.3 Results

### 3.3.1 ROS-responsive nanosensor calibration

Two types of ROS-sensitive nanosensors were fabricated incorporating different ROS sensitive dyes, one incorporating DCF-DA (DCF568), the other incorporating DHR123 (DHR568). The two systems were compared in terms of ROS reporting capability by challenging nanosensor solutions at 1 mgml$^{-1}$ with $O_2^-$ generated as an intermediate species in the enzymatic decomposition of xanthine to uric acid by XOD.

Both dyes exhibited an increase in FI ratio dependent upon XOD concentration however the DCF568 nanosensors exhibited a larger background FI ratio compared to the DHR568 type. There was also a greater variation of FI ratio within the DCF568 datasets compared to the DHR568. The FI ratio shifts in response to generated $O_2^-$ appeared overall to be larger and more highly resolved in the DHR568 nanosensors however the relatively small increase in FI ratio between the 2.5 and 5 Uml$^{-1}$ challenges (+0.109) suggested that the nanosensors reached maximum response.

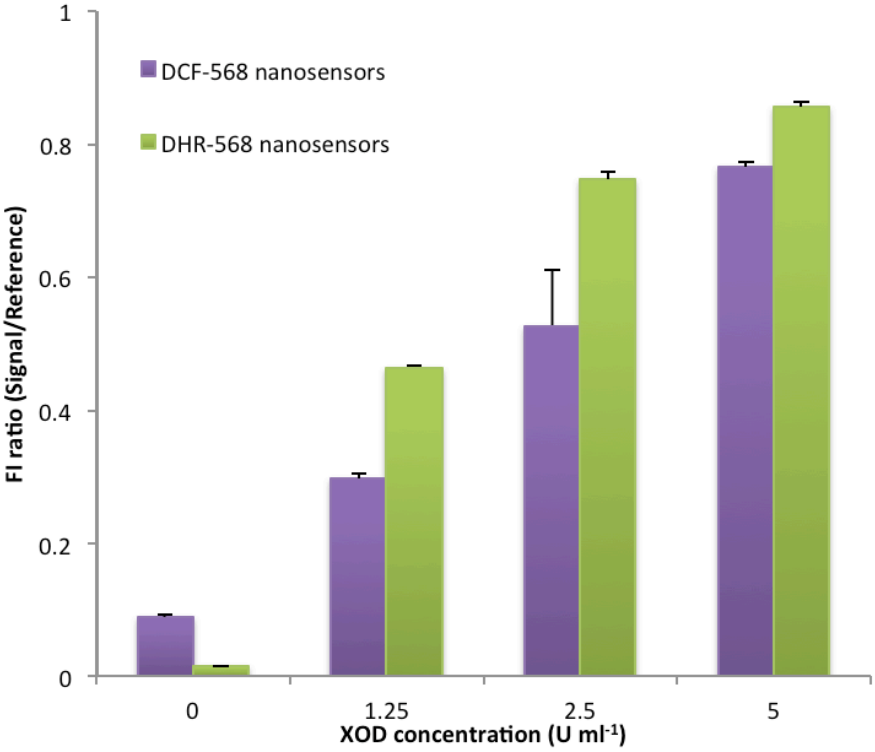

**Figure 3.1:** Differential reporting of enzymatically generated $O_2^-$ by both DHR568 and DCF568 containing nanosensors. Both types of demonstrated FI ratios that were dose dependent on XOD concentration, however the DCF568 nanosensors exhibited a much higher baseline FI in the presence of XOD and greater variation of response than the DHR568 nanosensors. Data presented ± SEM, n=4.

### 3.3.2 Cell mediated nanosensor delivery optimisation

NR8383 macrophage cells were incubated overnight with 10 $mgml^{-1}$ and 20 $mgml^{-1}$ concentrations of nanosensors. Nanosensors appeared to be successfully internalised via phagocytosis as demonstrated by the images displayed in Figure 3.2. An increase in nanosensor concentration resulted in an increase in FI for both dyes proportionally meaning the FI ratio was stable between treatment concentrations. This suggested that while the concentration of nanosensors within the cell is increased, the nanosensors were reporting similar environmental conditions.

Macrophages incubated with 10 $mgml^{-1}$ nanosensors were then assessed using confocal microscopy to confirm the internalisation of the nanosensors. The images shown in Figure 3.3 represented a 5-step Z stack of images taken at 5 µm intervals thorough the cells. The nanosensors appeared to be widely distributed throughout the cells with bright circular areas representing nanosensors located within an intact phagosome.

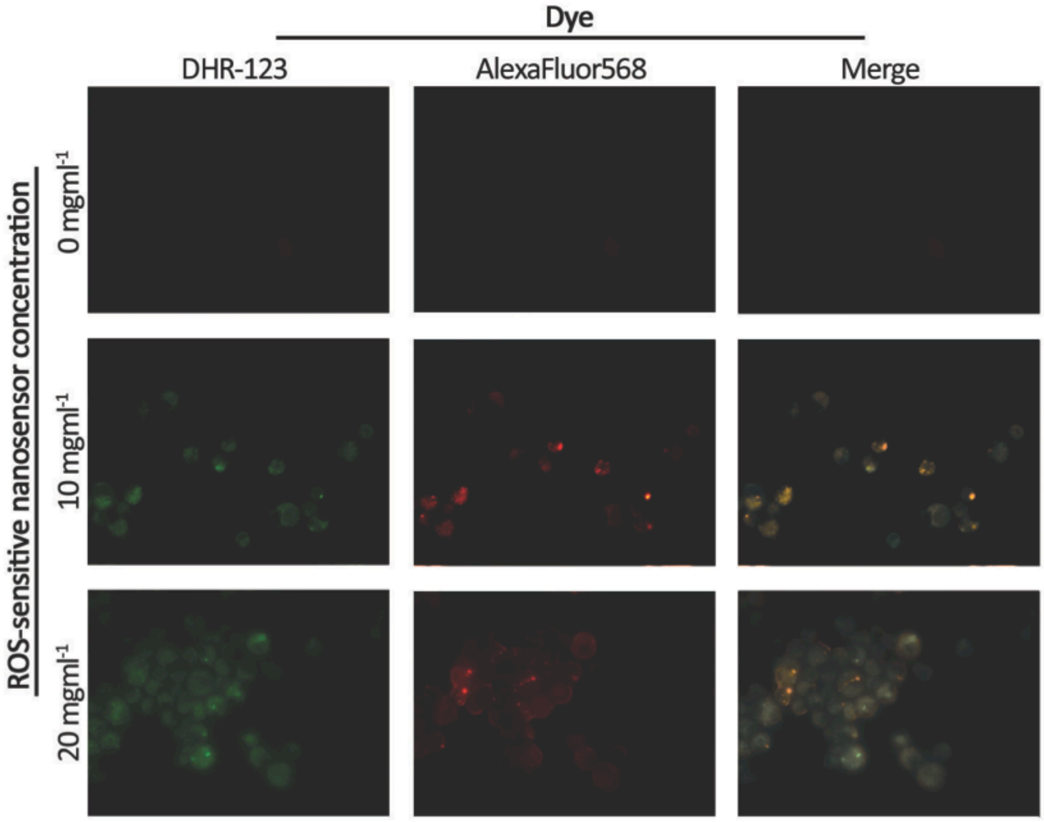

**Figure 3.2:** NR8383 macrophage cells treated with 10 and 20 $mgml^{-1}$ DHR568 nanosensors observed alongside cells without nanosensor treatment. Negligible fluorescence was observed for the negative control cells, whilst and increase in fluorescence was associated with increased nanosensor concentration.

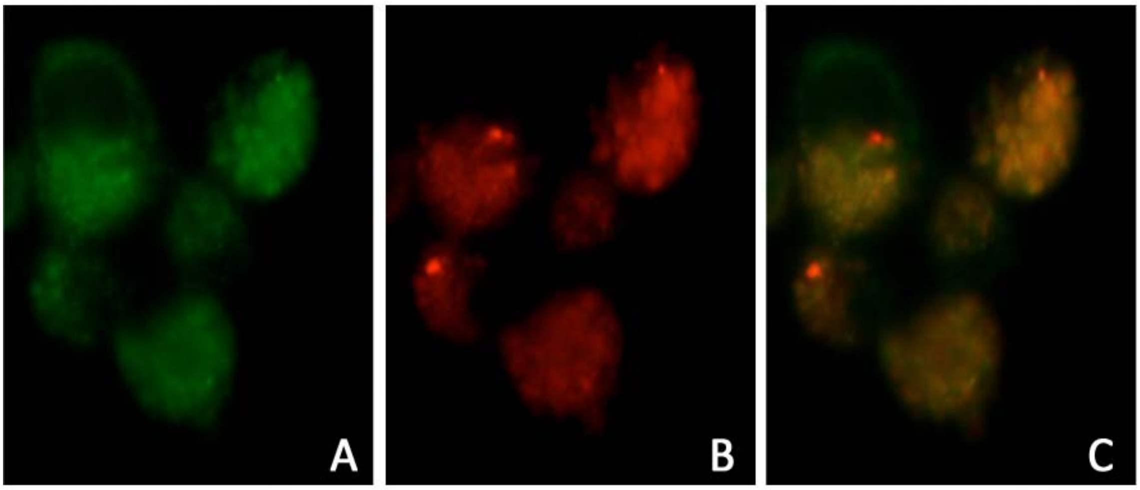

**Figure 3.3:** Confocal microscopy was used to confirm the phagocytic internalisation of ROS-sensitive nanosensor with the NR8383 macrophage cells. The above image represent DHR123 fluorescence (A) AlexaFluor568 fluorescence (B) and a merged image demonstrating dye colocalisation. The images were taken as transverse cross sections though the cells using a 5 step Z-stack at 5 µm intervals.

### 3.3.3 Effects of nanosensor loading upon cell viability

The effects of nanosensor loading upon cell respiration and viability were assessed using an MTT assay. An average cellular viability of 96.7% (±10.8%) compared to untreated control cells was observed for macrophages incubated with 10 mgml$^{-1}$ nanosensors. Incubating cells with 5 mgml$^{-1}$ nanosensors resulted in an average observed viability of 101.2% (±7.9%) *vs.* controls. Neither 5 nor 10 mgml$^{-1}$ treatments exerted a significant effect upon cell viability. Loading with 20 mgml$^{-1}$ nanosensors however elicited a 14.3% drop in cellular viability (±1.1%).

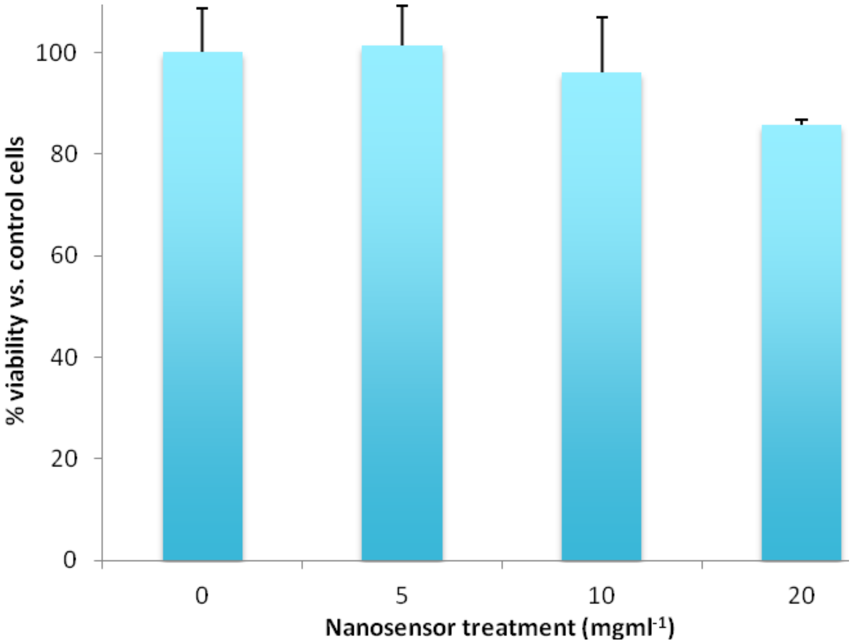

**Figure 3.4:** Assessment of the effects of nanosensor loading upon cellular viability was achieved using an MTT assay. Results are expressed as a percentage of untreated control cell viability. Only treatment with 20 mgml$^{-1}$ resulted in a significant reduction of cellular viability (14.3% ±1.1%, $p<0.005$). The data is presented ±SD, n=6)

### 3.3.4 Effect of nanosensor loading upon extracellular NO and $H_2O_2$ flux

The macrophage ability to produce NO$^{\bullet}$ and $H_2O_2$ following nanosensor internalisation was assessed using extracellular amperometric analyte specific electrodes. PMA dose-dependent increase in $H_2O_2$ and NO$^{\bullet}$ flux were observed for both nanosensor treated and untreated populations.

NO• flux from cells simulated with 1 µgml$^{-1}$ PMA generated mean peak currents of 792pA (±72pA) and 725pA (±68pA) with and without nanosensor preloading respectively. Stimulating nanosensor treated and untreated populations of cells with 5 µgml$^{-1}$ PMA generated mean peak currents 3.8 and 3.7 times larger than observed for stimulation with 1 µgml$^{-1}$ PMA respectively.

Like NO$^{\bullet}$ flux, $H_2O_2$ flux was not significantly different between nanosensor treated and untreated populations. Mean peak current responses of 1871pA (±469pA) and 5150 pA (±765pA) were observed from cells that were not treated with nanosensors following stimulation with 1 and 5 µgml$^{-1}$ PMA respectively. Nanosensor loaded cells generated mean peak current responses of 1641 pA (±150pA) and 4350 pA (±1387pA) in response to stimulation with 1 and 5 µgml$^{-1}$ PMA respectively. Both $H_2O_2$ and NO• were observed simultaneously. Nanosensor loading exerted no significant effects upon the cells' capacity to generate either molecule in response to PMA stimulation.

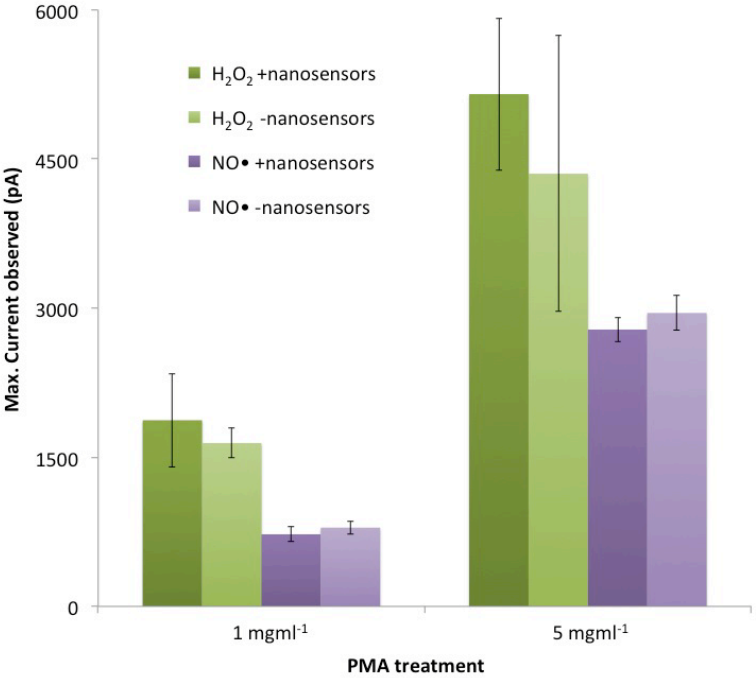

**Figure 3.5:** The effects of nanosensor loading upon a cell population's capability to generate $H_2O_2$ and NO• were investigated using amperometric extracellular electrodes. Nanosensor loading exerted no significant effects upon the observed peak currents generated by $H_2O_2$ or NO$^{\bullet}$ flux from cells stimulated with either 1 µgml$^{-1}$ or 5 µgml$^{-1}$ PMA. The data is presented ± SD, n=3.

### 3.3.5 Nanosensor reported PMA induced ROS responses

NR8383 macrophage cells were loaded with ROS sensitive nanosensor via cell-mediated delivery. One population of cells was treated with 5 µgml$^{-1}$ whilst the other received a PBS; both were monitored for 20 min post-addition. Measurements for both DHR123 and AlexaFluor568 FI were recorded to allow calculation of normalised ratiometric ROS response values. Cells treated with PMA exhibited a shift in FI ratio of +0.449 (±0.125), which was sustained over the remaining time-course of monitoring. The cells that received PBS in place of PMA did not exhibit a ROS response, and maintained a stable FI ratio of 0.422 (±0.012) over the entire time-course of monitoring.

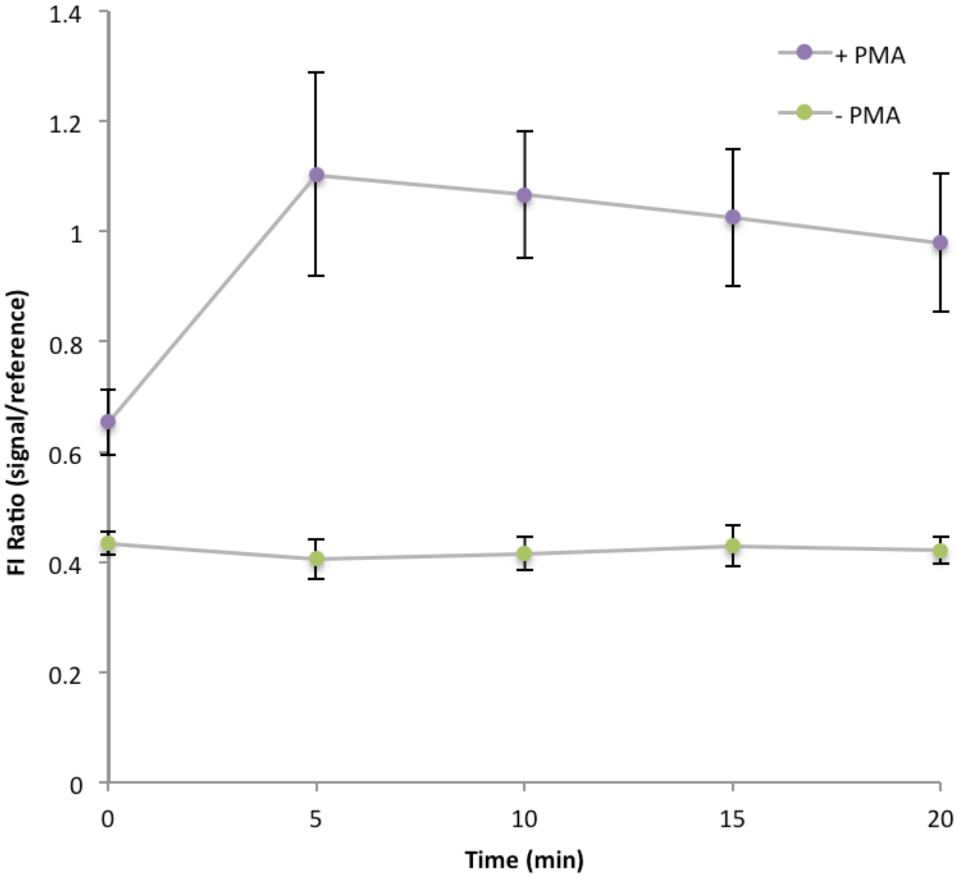

**Figure 3.6:** Nanosensor loaded NR8383 macrophage cells were monitored following treatment with either 10 µgml$^{-1}$ PMA or PBS. Cells that received PMA stimulation displayed a large increase in FI ratio. Conversely, cells that received no PMA treatment maintained a stable baseline response for the entire course of experimentation. The data is presented ±SEM, n=3. *** denotes $p<0.005$.

## 3.4 Discussion

In Chapter 2 of this thesis, the inherent difficulties of using native dyes to investigate real-time changes in intracellular ROS production were discussed. In this study, both DHR123 and DCF-DA were investigated to identify their potential to report ROS changes from within a polyacrylamide nanosensor matrix. Both dyes responded to $O_2^-$ and $H_2O_2$ generated through the enzymatic decomposition of xanthine by XOD. Their respective FI vales were monitored in conjunction with that of a stable reference dye co-immobilised within the nanosensor matrix. This ratiometric monitoring compensated for any variation that may have been caused by slight nanosensor concentration differences, temperature or photobleaching. DCF-DA nanosensors exhibited higher baseline FI ratio values and greater result deviation in response to enzymatically generated ROS than DHR123 (see Figure 3.1), and as such the latter was chosen to be the sensing element in the ROS sensitive nanosensors fabricated for this study.

The ROS-sensitive nanosensors were delivered to the intracellular environment of macrophage cells through cell-mediated uptake. This mode of nanosensor deliver has been previously reported (Henderson *et al*, 2009) however due to the low concentration of nanosensors used by Henderson and co-workers, the consistent monitoring of reference AlexaFluor568 was hindered and ratiometric measurements could not be made from the internalised nanosensors. A balance was required between nanosensor observability, cell viability and nanosensor economy. Nanosensor fabrication is a batch-based process, with each batch theoretically capable of producing ~700mg nanosensors. During this study, a single batch produced ~550-620mg of sensors. Seal leaks, oxygen intrusion, improper argon purging and incomplete polymerisation are all inhibitory factors to a maximum sensor yield. To enhance the observation of the reference dye, a greater concentration of nanosensors was incubated with the cells during the loading stage to increase uptake (10 $mgml^{-1}$ compared with 5 $mgml^{-1}$). Incubating cells with 10 $mgml^{-1}$ nanosensors allowed approximately 11 cell treatments with a single batch of sensors alongside repeated calibrations. Treating cells with a greater concentration would inherently reduce the number of treatments each batch could be used for, reducing the confidence in the results obtained using each batch and as result could not be readily corroborated through subsequent repetition with nanosensors from the same fabrication batch. The results presented in section 3.3.2 showed that the uptake of nanosensors at 10 mgml$^{-1}$ conferred stable measureable fluorescence from the reference dye co-localised with the ROS-sensitive dye. Incubation with 20 mgml$^{-1}$ nanosensors did increase the observed reference fluorescence however as incubation with a lower concentration resulted in observable nanosensor uptake, the use of a higher concentration during routine investigation would have been excessive and wasteful. It was also observed that incubation with 20 mgml$^{-1}$ nanosensors caused a significant drop in cell viability (see Figure 3.4). Coupland and co-workers also reported this increase in cell death when delivering pH nanosensors to non-phagocytic mesenchymal stem cells (Coupland *et al*. 2008). Although Coupland and co-workers conjugated the HIV-1 derived 'Tat' cell penetrating peptide to the nanosensors to induce internalisation, it was acknowledged within the report that cell loading limits exist where the volume of nanosensors delivered to the cells caused unsupportable levels of perturbation, leading to cell death. This could explain the reduction in viability described by the MTT assays when a comparatively highly concentrated 20 mgml$^{-1}$ nanosensor solution is employed (see Figure 3.4) and again reinforces the decision to routinely use a 10 mgml$^{-1}$ nanosensor solution during macrophage delivery over the course of this study.

Although the results of the cell viability assay demonstrated no significant changes in cell viability when exposed to up to 10 mgml$^{-1}$ nanosensors there was still the possibility that internalisation of foreign particulate may affect normal cell processes. To investigate this and to also assess any variation in ROS production in the presence of nanosensors, the extracellular flux of $NO^{\bullet}$ and $H_2O_2$ were monitored in both nanosensor treated and untreated cell populations in response to PMA stimulation. The flux elicited from cells did not appear to be dependent upon the loading of nanosensors. $H_2O_2$ and $NO^{\bullet}$-generated mean peak current magnitude was shown to be dependent upon PMA dose, but current responses of similar magnitude were generated in both the presence and absence of nanosensors. This added confidence that normal cellular functions are not impaired or affected by the internalisation of nanosensors.

Once internalised, the nanosensors recorded the PMA-induced intracellular generation of ROS in real time. A significant increase in FI ratio was observed following 5 min exposure (see Figure 3.6). This was sustained over the course of observation, and is in line with the increase in ROS generation observed following PMA stimulation previously reported (Chang *et al*. 2005a; Chang *et al*. 2005b; Manning *et al*. 1998). The change in FI ratio following stimulation may have been in response to $O_2^-$ generation induced by the activation of protein kinase C (PKC) and subsequent NADPH activity. This is initiated by a release of diacylglycerol and inositol trisphosphate by PKC following receptor mediated stimulation, in this study by PMA, causing phosphorylation of cytosolic components of NADPH oxidase, particularly p47$^{phox}$ (Giron-Calle and Forman 2000). Generation of $O_2^-$ will continue as long as NADPH oxidase remains in a phosphorylated state. The sustained increase in nanosensor FI ratio in the stimulated cells suggests that $O_2^-$ generation is prolonged following treatment. This corroborated data reported regarding the selective extracellular monitoring of $O_2^-$ using an amperometric technique (Chang *et al*, 2005b) where extracellular $O_2^-$ flux first generated a large initial peak in current followed by a second phase progressive increase in $O_2^-$ over a longer time period. This could be representative of a sudden $O_2^-$ burst to the extracellular space followed by the gradual flux of $O_2^-$ through the plasma membrane. Cells with internalised nanosensors but no PMA stimulation reported no change in FI ratio over the course of experimentation providing a baseline ratio representing normal cell oxidative state. Photobleaching was not an issue as exemplified by the stable measurements collected from the control cells over the course of experimentation.

In terms of the ultimate goal of integration of optical nanosensor sensing technology with amperometric measurements it has been demonstrated in this study that internalised nanosensors do not physically impede current measurements made using extracellular $H_2O_2$ and $NO^\bullet$ selective electrodes. This adds further confidence that the two sensing techniques are highly compatible and that full integration can be achieved. As a commercially available free radical analyser was employed to monitor extracellular flux, it was not possible to use the $O_2^-$ selective gold electrode discussed in Chapter 1 with the system. Prior to integrating this technology with the nanosensors it would be important to assess the compatibility of the gold electrodes with the optical measurements to ensure no technique cross-talk or interference occurs.  A recent study regarding the simultaneous measurement of intra- and extracellular ROS flux using free dyes and the aforementioned $O_2^-$ selective electrode system did not report any difficulties or anomalous effects whilst integrating the two techniques (Chang *et al*, 2005a). As the nanosensors will be completely internalised there should be no opportunity for interference with the electrodes.

This study represents the first ratiometric observations of real-time intracellular ROS generation using polyacrylamide ‘PEBBLE’ nanosensors. Although only very preliminary data has been presented, ample proof of concept is demonstrated. It must be observed that all data recorded from internalised nanosensors in this study was representative of nanosensors trapped within phagosomes. It is possible that some phagosomes may have lysed within the cell and as such the nanosensors were free within the cytoplasm; the images Figure 3.3 do appear to show a good spread of co-localised fluorescence from both DHR123 and AleaFluor568 throughout the cell. There are, however, many well defined circular areas of bright fluorescence that most likely represent phagosome-bound nanosensors. Investigation regarding the internalisation of nanosensors within non-phagocytic cells would be the next iterative stage of development as phagocytosis is not a natural feature of most clinically relevant cell models of disease. By establishing a reliable and non-cytotoxic method of delivering the nanosensors to the cytoplasm of non-phagocytic cells the investigation of the role of ROS in a variety of cell model could be expanded. Many methods have been reported with varying levels of success, for example bead loading, biolistic ‘GeneGun’ bombardment, lipofection and cell penetrating protein conjugation (Coupland *et al*. 2009; Webster *et al*. 2005; Webster *et al*. 2007; Xu *et al*. 2001).

## 3.5 References

Amatore, C., Arbault, S., Bouton, C., Drapier, J.C., Ghandour, H., Koh, A.C., 2008. Real-time amperometric analysis of reactive oxygen and nitrogen species released by single immunostimulated macrophages. Chembiochem 9(9), 1472-1480.

Boulton, S., Anderson, A., Swalwell, H., Henderson, J.R., Manning, P., Birch-Machin, M.A., 2011. Implications of using the fluorescent probes, dihydrorhodamine 123 and 2',7'-dichlorodihydrofluorescein diacetate, for the detection of UVA-induced reactive oxygen species. Free Radical Research 45(2), 139-146.

Buck, S.M., Koo, Y.E., Park, E., Xu, H., Philbert, M.A., Brasuel, M.A., Kopelman, R., 2004. Optochemical nanosensor PEBBLEs: photonic explorers for bioanalysis with biologically localised embedding. Current Opinion in Chemical Biology 8(5), 540-546.

Chang, S.C., Pereira-Rodrigues, N., Henderson, J.R., Cole, A., Bedioui, F., McNeil, C.J., 2005a. An electrochemical sensor array system for the direct, simultaneous *in vitro* monitoring of nitric oxide and superoxide production by cultured cells. Biosensors & Bioelectronics 21(6), 917-922.

Chang, S.C., Rodrigues, N.P., Zurgil, N., Henderson, J.R., Bedioui, F., McNeil, C.J., Deutsch, M., 2005b. Simultaneous intra- and extracellular superoxide monitoring using an integrated optical and electrochemical sensor system. Biochemical & Biophysical Research Communications 327(4), 979-984.

Chen, X., Zhong, Z., Xu, Z., Chen, L., Wang, Y., 2010. 2',7'-Dichlorodihydrofluorescein as a fluorescent probe for reactive oxygen species measurement: Forty years of application and controversy. Free Radic Res 44(6), 587-604.

Clark, H.A., Hoyer, M., Philbert, M.A., Kopelman, R., 1999. Optical nanosensors for chemical analysis inside single living cells. 1. Fabrication, characterization, and methods for intracellular delivery of PEBBLE sensors. Analytical Chemistry 71(21), 4831-4836.

Coupland, P.G., Fisher, K.A., Jones, D.R., Aylott, J.W., 2008. Internalisation of polymeric nanosensors in mesenchymal stem cells: analysis by flow cytometry and confocal microscopy. Journal of Controlled Release 130(2), 115-120.

Coupland, P.G., Briddon, S.J., Aylott, J.W., 2009. Using fluorescent pH-sensitive nanosensors to report their intracellular location after Tat-mediated delivery. Integr Biol (Camb) 1(4), 318-323.

Craig, M., Slauch, J.M., Craig, M., Slauch, J.M., 2009. Phagocytic superoxide specifically damages an extracytoplasmic target to inhibit or kill Salmonella. PLoS ONE 4(3), e4975.

Gautam, D., Misro, M., Chaki, S., Sehgal, N., 2006. $H_2O_2$ at physiological concentrations modulates Leydig cell function inducing oxidative stress and apoptosis. Apoptosis 11(1), 39-46.

Giron-Calle, J., Forman, H.J., 2000. Phospholipase D and priming of the respiratory burst by $H_2O_2$ in NR8383 alveolar macrophages. American Journal of Respiratory Cell and Molecular Biology 23(6), 748-754.

Graber, M.L., DiLillo, D.C., Friedman, B.L., Pastoriza-Munoz, E., 1986. Characteristics of fluoroprobes for measuring intracellular pH. Analytical Biochemistry 156(1), 202-212.

Hammond, V.J., Aylott, J.W., Greenway, G.M., Watts, P., Webster, A., Wiles, C., 2008. An optical sensor for reactive oxygen species: encapsulation of functionalised silica nanoparticles into silicate nanoprobes to reduce fluorophore leaching. Analyst 133(1), 71-75.

Hartley, A., Stone, J.M., Heron, C., Cooper, J.M., Schapira, A.H.V., 1994. Complex I inhibitors induce dose-dependent apoptosis in PC12 cells: relevance to Parkinson's Disease. Journal of Neurochemistry 63(5), 1987-1990.

Henderson, J.R., Fulton, D.A., McNeil, C.J., Manning, P., 2009. The development and *in vitro* characterisation of an intracellular nanosensor responsive to reactive oxygen species. Biosensors & Bioelectronics 24(12), 3608-3614.

Henderson, L.M., Chappell, J.B., 1993. Dihydrorhodamine 123: a fluorescent probe for superoxide generation? European Journal of Biochemistry 217(3), 973-980.

Koo, Y.E., Cao, Y., Kopelman, R., Koo, S.M., Brasuel, M., Philbert, M.A., 2004. Real-time measurements of dissolved oxygen inside live cells by organically modified silicate fluorescent nanosensors. Analytical Chemistry 76(9), 2498-2505.

Kurauchi, Y., Hisatsune, A., Isohama, Y., Katsuki, H., 2009. Nitric oxide-cyclic GMP signaling pathway limits inflammatory degeneration of midbrain dopaminergic neurons: cell type-specific regulation of heme oxygenase-1 expression. Neuroscience 158(2), 856-866.

Langer, D.A., Das, A., Semela, D., Kang-Decker, N., Hendrickson, H., Bronk, S.F., Katusic, Z.S., Gores, G.J., Shah, V.H., 2008. Nitric oxide promotes caspase-independent hepatic stellate cell apoptosis through the generation of reactive oxygen species. Hepatology 47(6), 1983-1993.

Liu, S.L., Li, Y.H., Shi, G.Y., Tang, S.H., Jiang, S.J., Huang, C.W., Liu, P.Y., Hong, J.S., Wu, H.L., 2009. Dextromethorphan reduces oxidative stress and inhibits atherosclerosis and neointima formation in mice. Cardiovascular Research 82(1), 161-169.

Manning, P., McNeil, C.J., Cooper, J.M., Hillhouse, E.W., 1998. Direct, real-time sensing of free radical production by activated human glioblastoma cells. Free Radical Biology & Medicine 24(7-8), 1304-1309.

Park, E.J., Brasuel, M., Behrend, C., Philbert, M.A., Kopelman, R., 2003. Ratiometric optical PEBBLE nanosensors for real-time magnesium ion concentrations inside viable cells. Anal Chem 75(15), 3784-3791.

Rinna, A., Torres, M., Forman, H.J., 2006. Stimulation of the alveolar macrophage respiratory burst by ADP causes selective glutathionylation of protein tyrosine phosphatase 1B. Free Radical Biology & Medicine 41(1), 86-91.

Rota, C., Chignell, C.F., Mason, R.P., 1999. Evidence for free radical formation during the oxidation of 2’-7’-dichlorofluorescin to the fluorescent dye 2’-7’-dichlorofluorescein by horseradish peroxidise:: Possible implications for oxidative stress measurements. Free Radical Biology & Medicine 27(7-8), 873-881.

Sumner, J.P., Aylott, J.W., Monson, E., Kopelman, R., 2002. A fluorescent PEBBLE nanosensor for intracellular free zinc. Analyst 127(1), 11-16.

Tobi, S.E., Paul, N., McMillan, T.J., 2000. Glutathione modulates the level of free radicals produced in UVA-irradiated cells. Journal of Photochemistry and Photobiology B 57(2-3), 102-112.

Webster, A., Compton, S.J., Aylott, J.W., 2005. Optical calcium sensors: development of a generic method for their introduction to the cell using conjugated cell penetrating peptides. Analyst 130(2), 163-170.

Webster, A., Coupland, P., Houghton, F.D., Leese, H.J., Aylott, J.W., Webster, A., Coupland, P., Houghton, F.D., Leese, H.J., Aylott, J.W., 2007. The delivery of PEBBLE nanosensors to measure the intracellular environment. Biochemical Society Transactions 35(Pt 3), 538-543.

Xu, H., Aylott, J.W., Kopelman, R., 2002. Fluorescent nano-PEBBLE sensors designed for intracellular glucose imaging. Analyst 127(11), 1471-1477.

Xu, H., Aylott, J.W., Kopelman, R., Miller, T.J., Philbert, M.A., 2001. A real-time ratiometric method for the determination of molecular oxygen inside living cells using sol-gel-based spherical optical nanosensors with applications to rat C6 glioma. Analytical Chemistry 73(17), 4124-4133

Zurgil, N., Shafran, Y., Afrimzon, E., Fixler, D., Shainberg, A., Deutsch, M., 2006. Concomitant real-time monitoring of intracellular reactive oxygen species and mitochondrial membrane potential in individual living promonocytic cells. Journal of Immunological Methods 316(1-2), 27-41.

# Chapter 4. Application of pH-sensitive nanosensors to primary cell models of Chronic Fatigue Syndrome

## 4.1 Introduction

This study aimed to investigate the capacity of pH-sensitive nanosensors to report changes in $pH_i$ dynamics within myoblasts and was carried out in collaboration with Dr Audrey Brown from the Diabetes Research Group at Newcastle University. Dr Brown supplied the primary myoblasts used throughout the investigation. CFS is a complex and debilitating disease state that is poorly understood. There is currently much debate as to whether the CFS manifests in patients through purely psychological means or whether there is an underlying physiological basis for the disorder. Preliminary work proposing that muscle acidosis during exercise and subsequent poor recovery may be a factor in the manifestation of CFS has recently been reported (Jones *et al*. 2010). Acidosis is a common feature of many metabolic disorders, including Leigh's disease, dystonia and Diabetes mellitus (Randolph *et al*. 2011; Robergs *et al*. 2004; Robinson 2006). Reduced intramuscular pH recovery time and reduced proton efflux in CFS patients has been reported (Jones *et al*. 2010). This could be related to modified functionality of the lactic acid metabolic pathway in CFS state myoblasts. Pyruvate dehydrogenase complex (PDC) is a 3-protein complex responsible for the conversion of pyruvate to acetyl coenzyme A during aerobic respiration. When functionality of this complex is reduced, pyruvate generated by glycolysis accumulates within cells and is metabolised anaerobically to lactic acid, the accumulation of which, due to inefficient aerobic respiration, causes a drop in pH and concurrent deterioration of muscle functionality. In brief, dichloroacetate (DCA) is a pyruvate analogue that promotes the clearing of lactic acid in cells by inhibiting the pyruvate dehydrogenase kinase (PDK) responsible for inactivating PDC (Fouque *et al*. 2003). By promoting the active state of PDC kinase, intracellularly accumulated lactic acid can be converted to pyruvate and metabolised aerobically assuming adequate ventilation and perfusion, resulting in a return to physiologically normal pH.

To investigate the possible acidosis-induced pathophysiological rationale of CFS manifestation, cells were cultured from donor muscle biopsies taken from the *Vastus lateralis*, the position of which is demonstrated by Figure 4.1. The cells were subsequently cultured and divided into two subpopulations. One subpopulation represented ‘disease state’ patients that had previously been diagnosed with CFS (‘CFS cells’). The other subpopulation represented patients who did not present with any symptoms of any metabolic disorder (‘non-CFS cells’). The *Vastus lateralis* was chosen as the point of biopsy due to the ease of access and as previously acquired control muscle samples were harvested from this region.

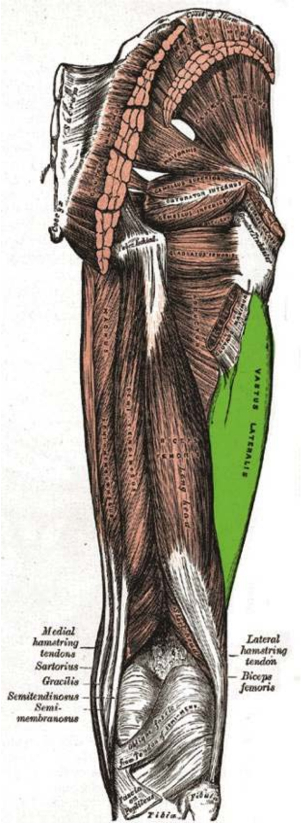

**Figure 4.1:** An image adapted from Grey’s Anatomy showing the position of the *Vastus lateralis*. This muscle forms the largest part of the *Quadriceps femoralis.*

Initial investigations were carried out using immortalised primary myoblasts as they were readily available in large numbers. These cells were also harvested from the *Vastus lateralus* of an asymptomatic patient but were transfected with the temperature-dependant SV40 large T antigen gene. This gene conferred an indefinite proliferative ability to the cells when cultured at 33° C. When cultured at 37° C like all other cells in this investigation proliferation was suspended.

The nanosensor platform confers many benefits over the use of free FITC, two of the most prominent being the ease of nanosensor calibration compared to free dye, which is prone to cells leaching and uneven loading, and increased selectivity of FITC for pH by preventing interactions with the intracellular proteins by size exclusion. The effects of intracellular environment upon un-encapsulated internalised free dye can make obtaining reliable data extremely difficult; for example, reactions with the sulphydryl and amine groups of endogenous proteins can lead to dye quenching (Graber *et al*. 1986). Preventing unspecific interactions through entrapment within a polymer matrix has been reported to improve the responses of analyte-responsive fluorescent dyes by preventing unspecific oxidation (Srivastava and Krishnamoorthy 1997). Once internalised, the nanosensors make up approximately one part per billion of the cell volume (Buck *et al*. 2004) allowing cell monitoring with a minimum of cell perturbation in comparison with other $pH_i$ techniques such as opto-chemical techniques using matrix functionalised fibre optic probes or intracellular microelectrodes (Coupland *et al*. 2009; Schweining 1999). Both of these techniques require penetration of the cell membrane in order to make intracellular measurements as well as a physical connection to an optical or electrical detecting device. Only one cell can be monitored at any time with microelectrodes or optodes. Monitoring a whole population of cells simultaneously would require a vast number of devices, one for each cell monitored. A maximum of 3 or 4 electrodes could be used on one cell before membrane integrity was completely compromised, meaning the spatial resolution of measurement within single cells is limited (Schweining 1999). The pH-responsive nanosensors offer the cellular distribution properties of a free dye due to their negligible size in comparison to a mammalian cell, whilst also conferring the dye protection and interference prevention benefits of an optode matrix. Nanosensors also avoid the encumbrances of a physical connection with the fluorescence detecting device, making the platform highly compatible with other cell monitoring techniques for simultaneous measurement.

In this study, the nanosensor technology previously discussed in Chapter 3 was adapted to confer pH sensitivity in place of ROS-sensitivity. A lipofection-based internalisation technique was used to deliver a nanosensor cargo to the intracellular environment of both CFS and non-CFS primary myoblasts. Using confocal microscopy it was possible to assess the success of the internalisation technique and confirm the intracellular position of the delivered nanosensors. Ratiometric measurements were acquired from the nanosensor-doped cells following treatment with the PDH kinase inhibitor DCA, allowing differential effects in CFS and non CFS cells to be observed.

## 4.2 Materials and methods

### 4.2.1 Cell culture and preparation

Both diseased and non-diseased subpopulations of primary myoblasts were routinely cultured using antibiotic free Ham's F10 medium supplemented with 20% FCS and 2% Chick embryo extract. (PAA, UK). Cells were maintained in a humidified environment containing 5% (v/v) $CO_2$ at 37˚C throughout. Cells were grown to ~80% confluence and did not exceed passage 9 during the course of experimentation. Transformed primary myoblasts were cultured using the same medium and environment however the temperature of the incubator was set to 35˚C to allow cell proliferation.

### 4.2.2 pH-sensitive nanosensor fabrication

Nanosensors comprising pH sensitive dye FITC and stable reference dye AlexaFluor568 co-localised within a porous polyacrylamide matrix were fabricated using a slightly modified method of that described in Chapter 3. An organic phase was prepared by doping 42 ml hexane with SDS and Brij30 to control nanosensor pore size. An aqueous solution of monomers was prepared by dissolving powdered acrylamide (3.8 M) and N,N-methylenebisacrylamide (0.5 M) in 2 ml water. FITC and AlexaFluor568 were added to the monomer solution to a concentration of 100 $\mu gml^{-1}$ immediately prior to dispersal within the hexane/surfactant mixture to form a reverse phase micro-emulsion. Whilst under constant stirring, polymerisation was initiated by the addition of 15 µl TMED and 30 µl 10% APS solution. Polymerisation was continued for at least 2 h. Hexane was rotovaporated from the emulsion to yield a nanosensor-containing slurry. Surfactants were removed by washing in absolute ethanol. Nanosensors were finally retrieved from suspension using a vacuum filtration system in conjunction with 20nm pore-size Whatman anodisc filters. Dry sensors were stored at -20°C and protected from light by wrapping with aluminium foil.

### 4.2.3 Lipofection-mediated nanosensor delivery

During all stages of preparation and internalisation the sensors were protected from light-induced dye autoxidation as far as possible by covering containers with aluminium foil. Sensor solutions of 100 $mgml^{-1}$ were prepared in PBS then used to make a 10x concentration mixture of nanosensors and Lipofectamine 2000 transfection reagent (Invitrogen, UK) in a foil-wrapped Eppendorf tube. This mixture was allowed to complex for 15 min at room temperature prior to use. Meanwhile, cells at 80% confluence in routine culture flasks were washed twice with pre-warmed PBS and covered with growth medium containing no supplements. The nanosensor/Lipofectamine 2000 complex was diluted 1:10 into the flasks and allowed to incubate overnight. The following morning, cells were trypsinised, washed and seeded into test plates with routine culture medium ready for experimentation.

### 4.2.4 Preparation for confocal microscopy

The nanosensor-doped cells were seeded into 24-well plates containing 16 mm diameter glass coverslips at a density of 1000 cells per well. Cells were incubated in routine culture medium for 5 h to allow attachment, after which the medium was replaced with 4% paraformaldehyde to fix the cells. The cells were then thoroughly rinsed after 15 min incubation and stored in PBS prior to imaging.

### 4.2.5 Fluorimetric measurement setup

FI was measured using a Tecan Infinite200 fluorimeter and data was acquired using the associated Magellan software. For pH nanosensors, standard settings for FITC ($\lambda_{ex}$ = 495nm $\lambda_{em}$ = 520nm) and for AlexaFluor568 ($\lambda_{ex}$ = 578nm, $\lambda_{em}$ = 603nm) were used. The gain was set to a value of 70 for all experiments unless otherwise stated.

### 4.2.6 Dichloroacetate treatment regime

Prior to seeding into a black walled 96 well plate, nanosensors were delivered into the cells by incubating with 10 mgml$^{-1}$ pH-sensitive nanosensor complex made with 0.03% Lipofectamine 2000 transfection reagent in unmodified Ham’s F10 medium for overnight, after which they were trypsinised, washed and seeded into at a density of 100 cells per well. The following morning, treatment was initiated by replacing the medium with DCA-doped medium at various concentrations from 100mM to 16µM. pH was ascertained by fluorimetrically interrogating the plates in the Infinite M200 fluorimeter as described in section 4.2.5. The resulting ratio of signal to reference fluorescence ratio was converted to a pH reading using the linear regression analysis of a previously generated nanosensor calibration curve. Plates were interrogated immediately after treatment then once every 30-60 min that the DCA treatment remained on the cells (5-6 h).

## 4.3 Results

### 4.3.1 Nanosensor delivery optimisation and confirmation

Confocal microscopy was used to confirm the success of both cell mediated and lipofection intracellular delivery techniques. An increase in Lipofectamine 2000 concentration resulted in an increase in the detachment of cells from the cover slips, meaning there were fewer cells available for observation. Incubation with 0.03% Lipofectamine 2000 gave the highest density of nanosensors within cells and displayed the highest retention of cells on the cover slips examined. The 0.05% Lipofectamine 2000 treated samples displayed good internalisation properties however there was substantial detachment of cells from the cover slip. Lipofectamine 2000 (0.1%) displayed very low sensor uptake and a very high loss of cells.

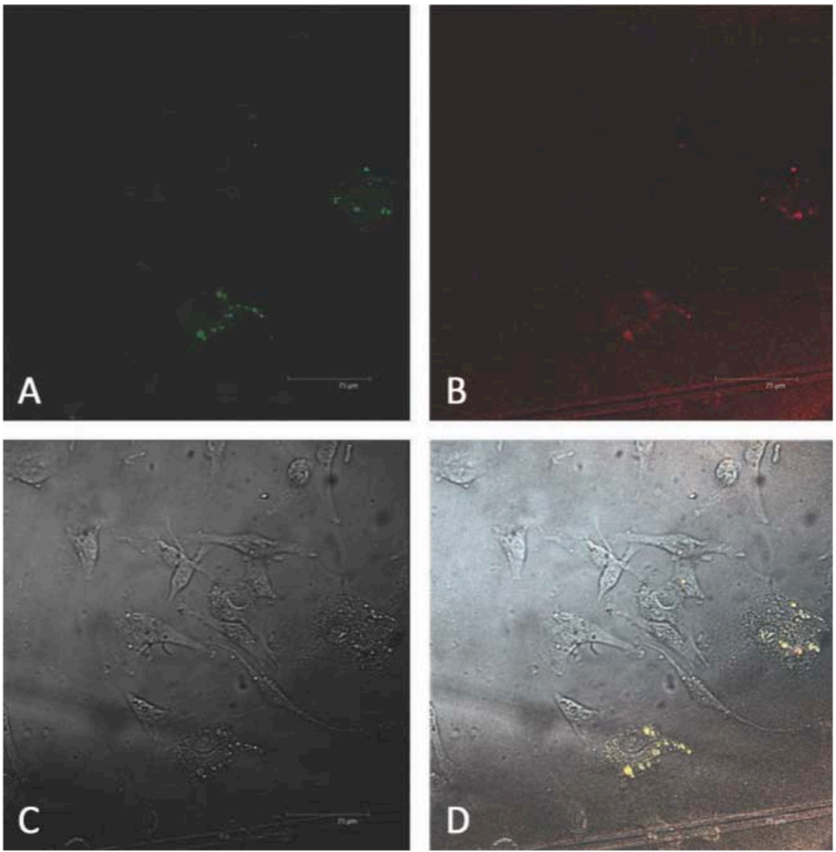

**Figure 4.2:** I5B1 immortalised myoblasts were treated with 10 mgml$^{-1}$ pH-sensitive nanosensor complexes made with 0.1% Lipofectamine 2000. Images represent a 5-step Z stack of images taken at 5 µm intervals. As can be observed from the bright-field image (C) here was a low population density of cells on the cover slip. The merged images of FITC fluorescence (A), AlexaFluor568 fluorescence (B) and the bright-field image show that nanosensors were internalised within the remaining cells.

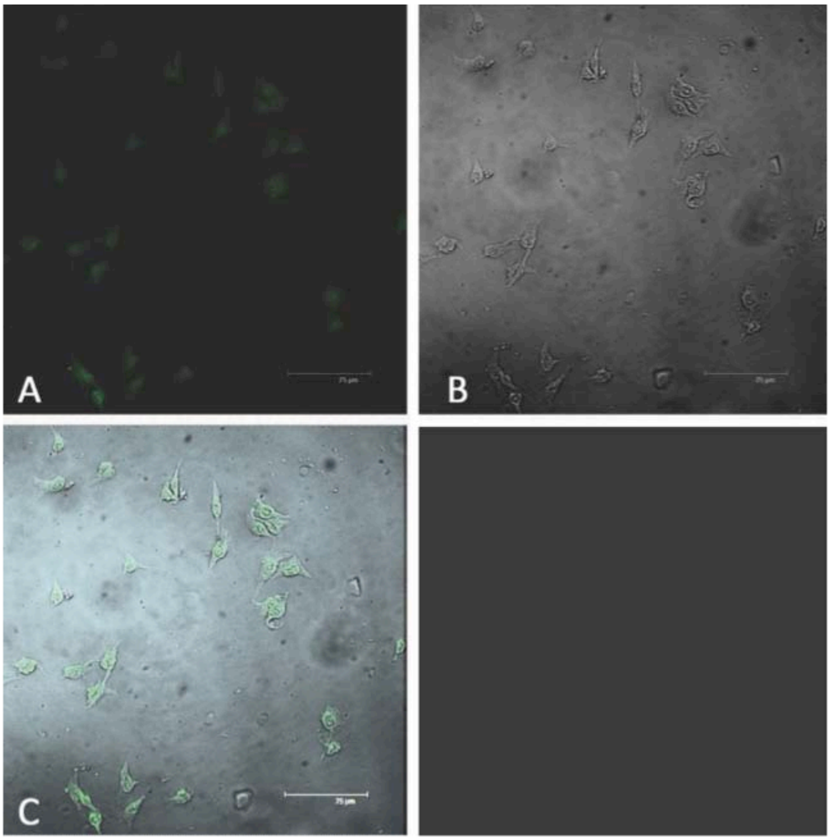

**Figure 4.3:** I5B1 immortalised myoblasts were treated with 10 mgml$^{-1}$ pH-sensitive nanosensor complexes made with 0.05% Lipofectamine 2000. Images represent a 5-step Z stack of images taken at 5 µm intervals. As can be observed from the bright-field image (B) the cell population of the cover slip was sparse. Images of FITC fluorescence can be observed in image A and a merged image confirming FITC fluorescence only occurs within the confines of the cell membranes is shown in image C.

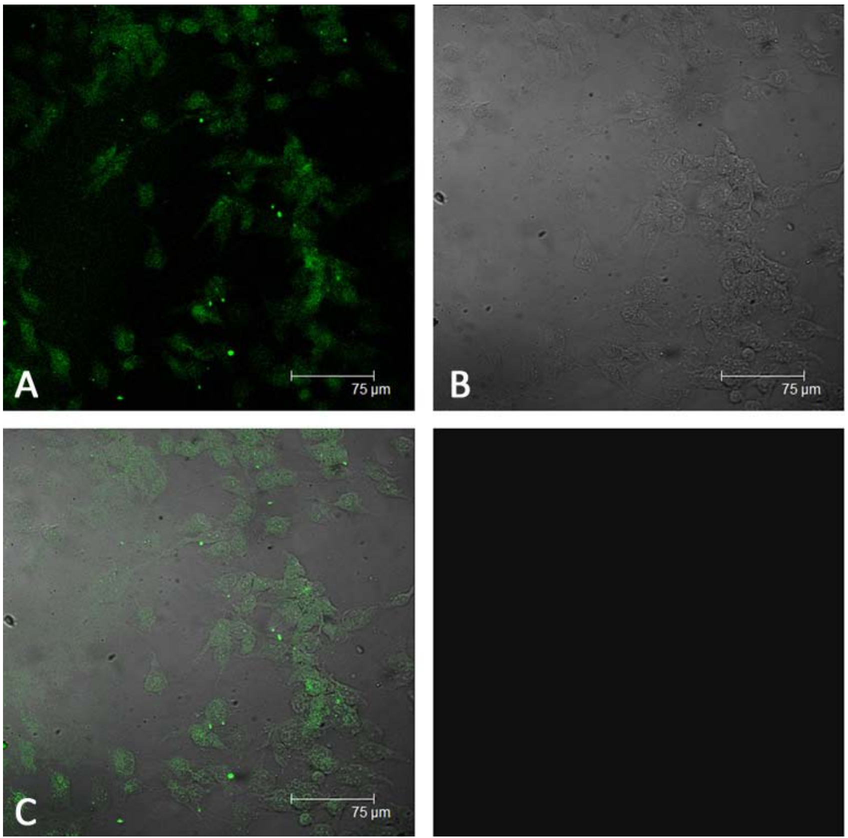

**Figure 4.4:** I5B1 immortalised myoblasts were treated with 5 mgml$^{-1}$ pH-sensitive nanosensor complexes made with 0.05% Lipofectamine 2000. Images represent a 5-step Z stack of images taken at 5 µm intervals. As can be observed from the bright-field image (B) the cell population of the cover slip was sparse. Images of FITC fluorescence can be observed in image A and a merged image confirming FITC fluorescence only occurs within the confines of the cell membranes is shown in image C.

To confirm that the nanosensor internalisation protocol was transferable to non-immortalised primary myoblasts, a sample of CFS representative cells (CF10) were treated with 10 mgml$^{-1}$ nanosensor complex made with 0.03% Lipofectamine 2000. Both FITC and AlexaFluor568 fluorescence was observed within the cells. Fluorescence was distributed throughout the whole cells with no membrane association.

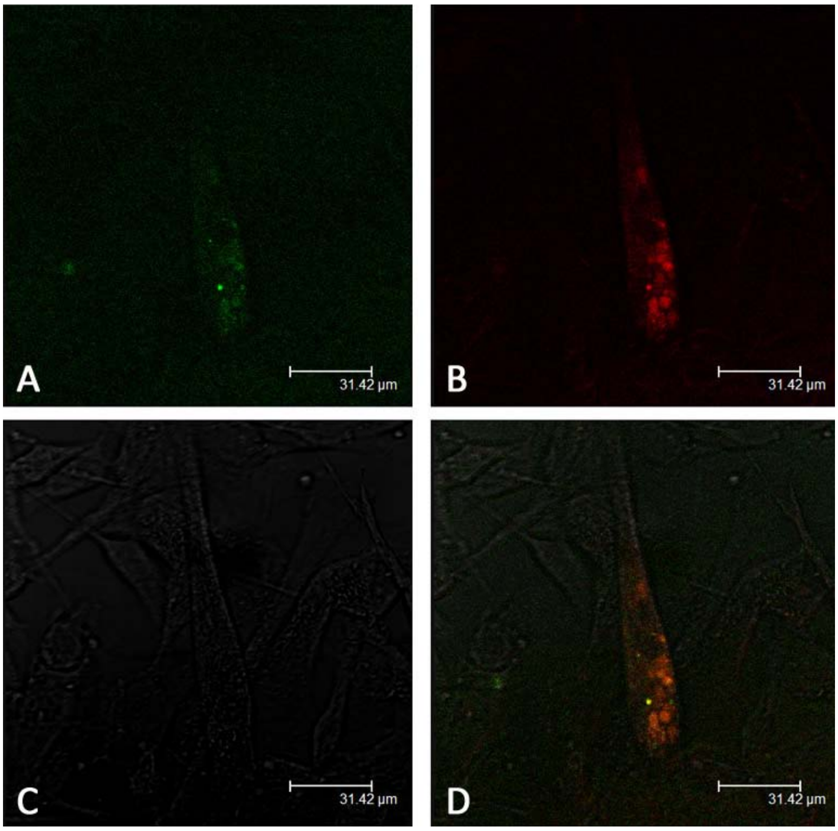

**Figure 4.5:** Confocal imaging of a discreet Z-slice though a non-CFS muscle cell gives conclusive information regarding the location of nanosensors within the cell. A fair distribution of nanosensors throughout the cell can be observed. FITC fluorescence (A) Alexafluor568 fluorescence (B) bright-field (C) and merged (D) images confirm the co-localisation of the two dyes within the cell, verifying the successful delivery of nanosensors to the intracellular environment.

### 4.3.2 pH-sensitive nanosensor calibration

Nanosensors at 1 mgml$^{-1}$ were dissolved in 100 mM phosphate buffer over a range of different pH values. FI measurements for both FITC and AlexaFluor568 were acquired and average FI ratios for each sample group were calculated and averaged. It was observed that an increase in mean FI ratio was linearly dependent upon the pH of the buffer solution ($y=2.2109x-10.636$, $r=0.996$, $n=5$). The linear regression of the calibration curve was then employed to calculate pH$_i$ values from the FI ratios collected from nanosensor-doped cells. The data is presented in Figure 4.6.

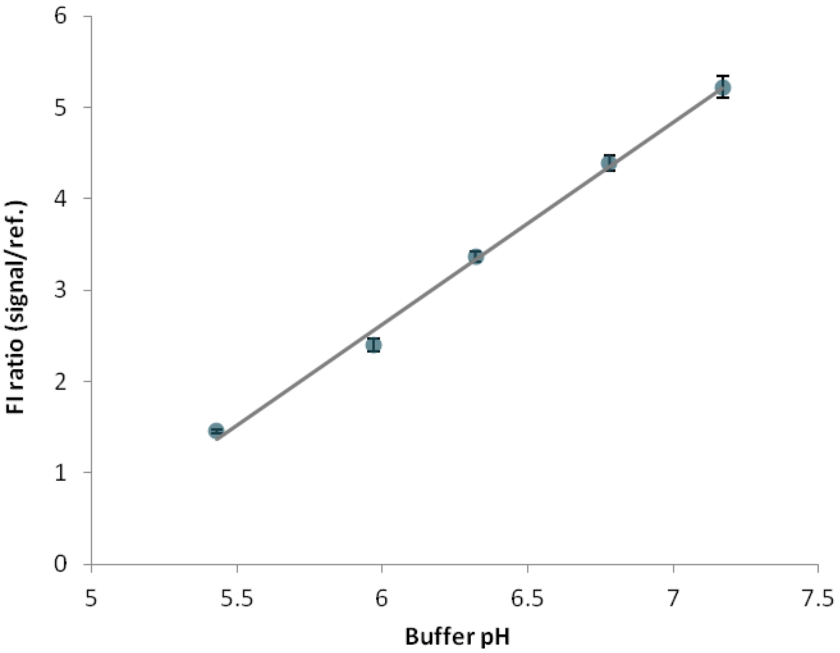

**Figure 4.6:** Calibration curve of pH sensitive nanosensors with 100 mM phosphate buffer of varying pH. The ratio of FITC to AlexaFluor568 fluorescence was shown to be linearly dependent on pH within physiological range (y=2.2109x-10.636). The data is presented ±SEM, n=4, r=0.996

### 4.3.3 Intracellular monitoring using internalised pH-responsive nanosensors

pH responsive nanosensors were delivered within cultured primary myoblasts from both CFS and non-CFS subpopulations. The cells were treated with DCA-doped culture medium at 16 µM, and any changes in $pH_i$ were monitored for 90 minutes thereafter. As shown in Figure 4.7, non-CFS cells did not show a significant change in $pH_i$ following treatment with DCA, with both treated and untreated cells maintaining a $pH_i$ of 6.54 (SD=0.0947). There was a significant difference in $pH_i$ between DCA treated and untreated CFS cells, with an average difference of +0.77 pH units (SD=0.0177, p<0.0005). Untreated CFS cells displayed a $pH_i$ that was significantly lower than that measured in non-CFS cells (p<0.0005), while treated cells demonstrated a $pH_i$ value higher than any observed in non-CFS cells (p<0.005).

The investigation was repeated to expand the range of DCA concentrations tested to investigate whether a dose-dependent effect could be observed. Samples of both CFS and non-CFS cells were treated with culture medium doped with 0-40 µM DCA. FI ratio values were acquired from the nanosensors as described in the materials and methods section of this chapter over a period of 3 hr, then were converted to pH values using the previously established calibration curve (see Figure 4.6) and plotted as a function of time (data shown in Figures 4.8 and 4.9 for CFS and non-CFS cells respectively. Data collected from CFS cells demonstrated significant changes in $pH_i$ between the different treatment groups. CFS cells treated with 20 µM DCA exhibited an average difference of 0.38 pH units at each time point *vs.* untreated CFS cells. The 10 and 40 µM treatment groups demonstrated significant difference from the control cells ($p<0.0005$) however they show no significant difference from each other. The non-CFS cells however showed no significant pH changes in response to DCA. pH values for each DCA treatment group show standard deviation of less than 0.09 pH units at each time point.

Data from both the CFS and non-CFS cells lines was combined in Figure 4.10 to aid comparison between the two cell types. It is clear that the untreated CFS cells are much lower in $pH_i$ than the non-CFS cells. It is interesting however that CFS cells treated with 20 µM DCA exhibited $pH_i$ values that are not significantly different from the values calculated from the non-CFS cells. This suggests that treatment with DCA is capable of boosting the $pH_i$

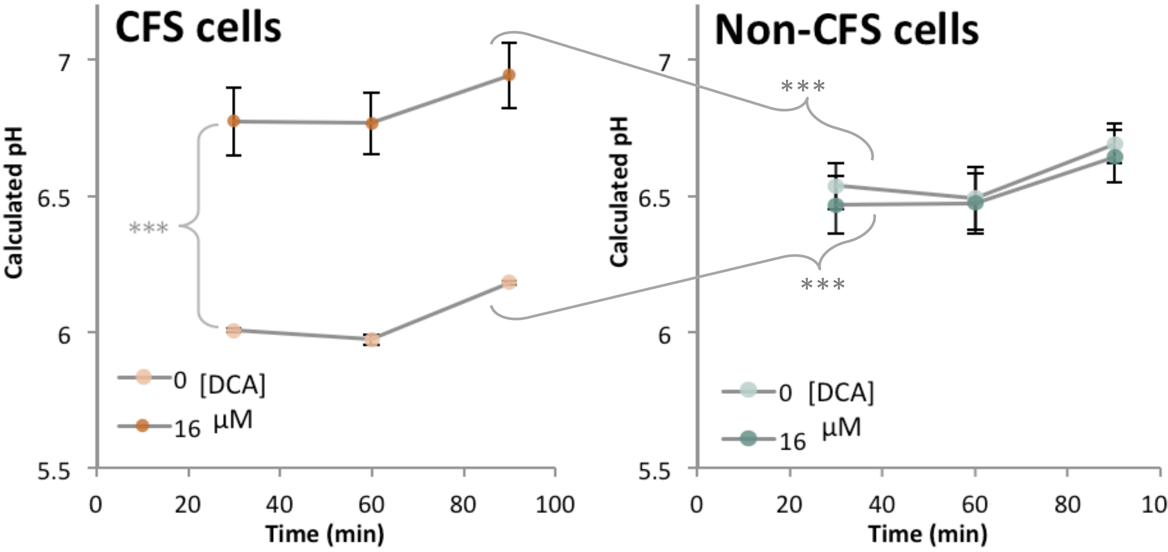

**Figure 4.7:** Cultured primary muscle cell lines CF01 (CFS cells) and PO13 (non-CFS cells) were treated with DCA at 16µM. No significant changes in pH were observed between treated and untreated populations of control PO13 myoblasts. Conversely, DCA boosted the pH of disease state CF01 cells beyond the baseline level of normal myoblasts while untreated disease state cells remained at a significantly lower pH (the data is presented ±SEM, n=4, *** denotes p< 0.005).

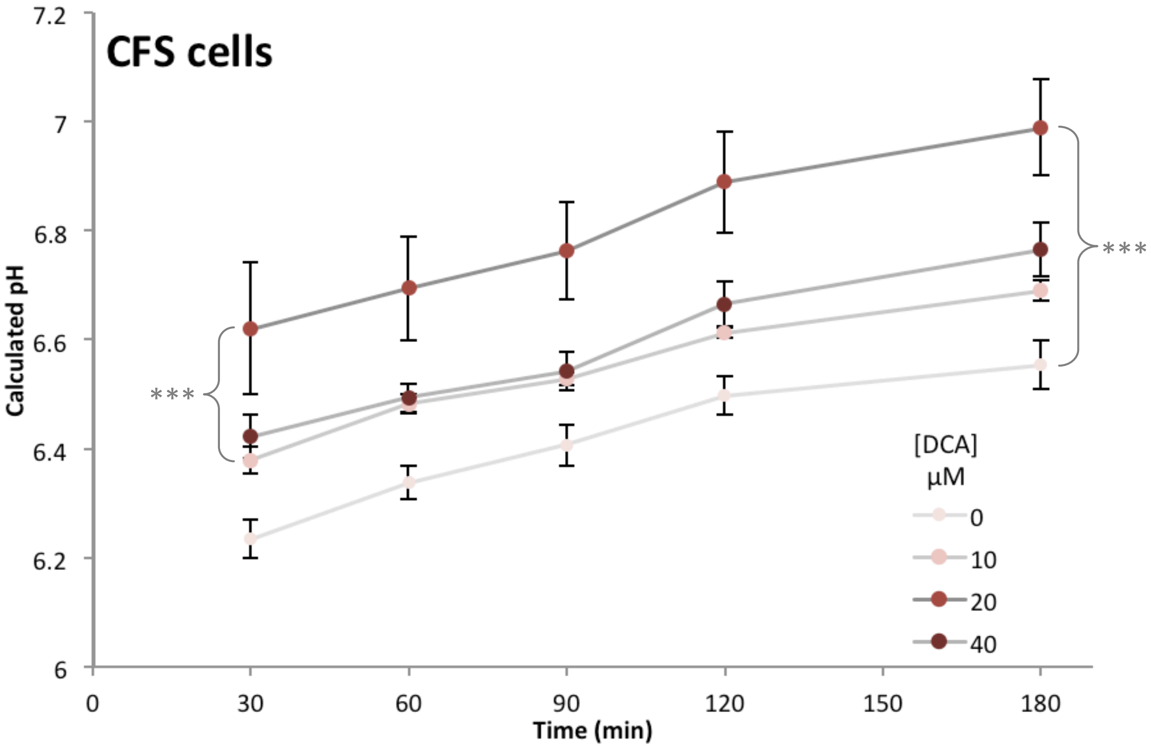

**Figure 4.8:** Primary myoblasts cultured from a biopsy of a patient diagnosed with CFS were doped with pH-responsive nanosensors and treated with various concentrations of the PDHK inhibitor DCA ranging from 0-40 µM (the data is presented ±SEM, n=4. *** denotes p<0.0005).

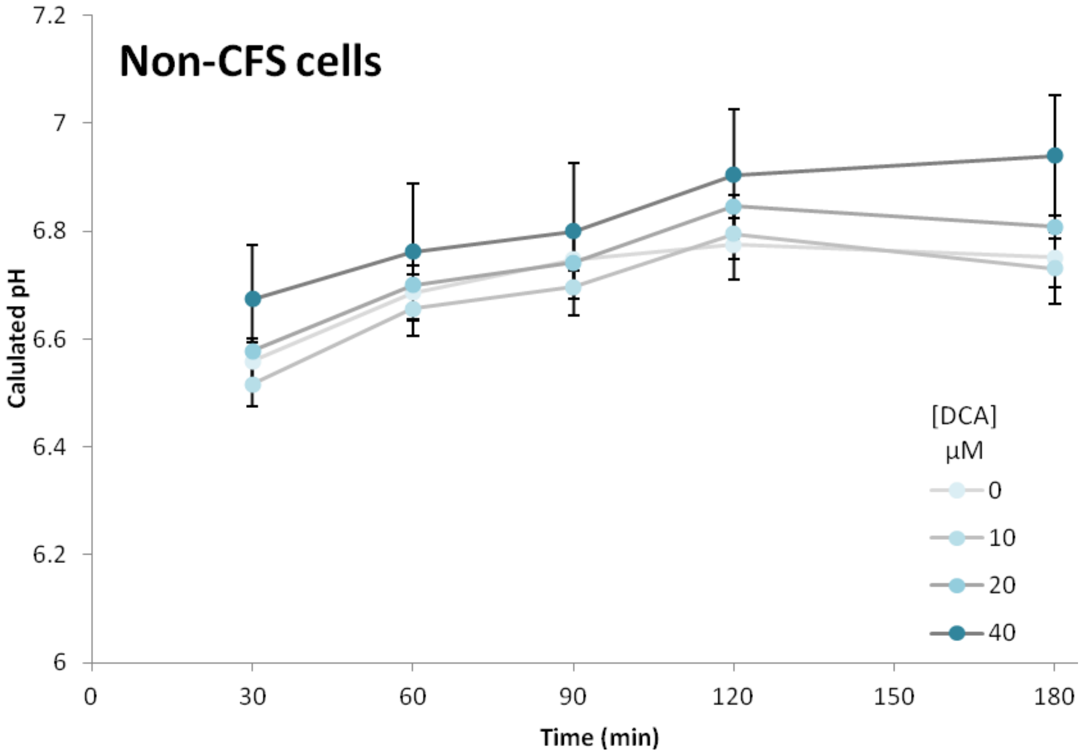

**Figure 4.9:** Primary myoblasts cultured from asymptomatic muscle tissue were doped with pH-responsive nanosensors and treated with various concentrations of the PDHK inhibitor DCA ranging from 0-40 µM. No significant differences were observed between any of the data sets (The data is presented ± SEM, n=4).

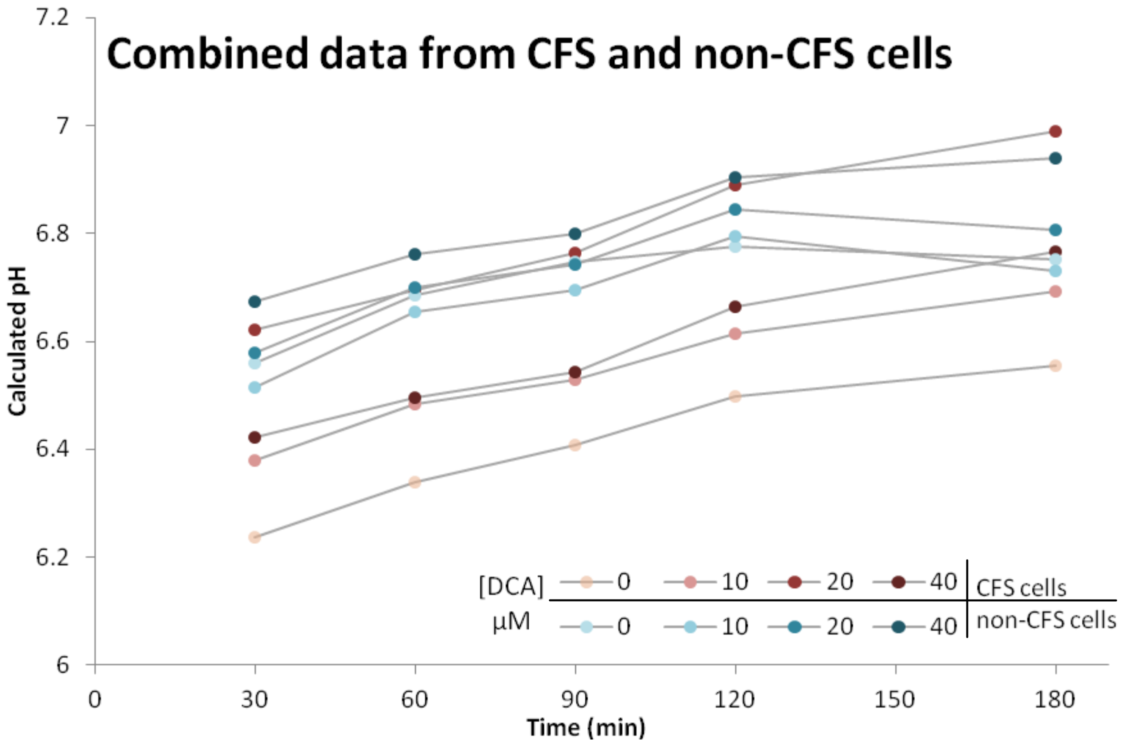

**Figure 4.10:** Data from Figures 4.8 and 4.9 are combined here to allow comparison. For ease of visualisation, error bars have been omitted. Data collected from the cells demonstrated that CFS cells treated with 20 µM DCA exhibited an increased pH that demonstrated no significant difference from the non-CFS cells.

## 4.4 Discussion

Lactic acidosis is a dangerous and potentially fatal condition associated with many metabolic disorders. Homeostatic control of muscular $pH_i$ is tightly regulated and is effectively buffered by bicarbonate and endogenous proteins. Disruption of proton efflux from cells or the metabolic pathways governing pyruvate metabolism inevitably have knock on effects upon the endogenous acidotic state. Monitoring $pH_i$ *in vivo* is can be achieved using microelectrodes (Trenholm and Baldridge 2010), magnetic reesonense spectroscopy (MRS) or as more recently demonstrated through functional magnetic resonance spectroscopy (fMRI) (Jones *et al*, 2010). All three of these techniques present their own set of challenges when working with cultured cells, with microelectrodes requiring an incredibly high level of skill and dexterity to employ with accuracy while MRS and fMRI techniques are both expensive and simply cannot be transferred to *in vitro* investigation. In this study, the $pH_i$ dynamics of both CFS and non-CFS cells were successfully assessed using pH nanosensors fabricated using a modification of the process described in Chapter 3. pH sensitivity was conferred by substituting FITC for DHR123 as the signal dye embedded alongside AlexaFluor568 within the polyacrylamide nanosensor matrix. Prior to internalisation within cells, nanosensors were calibrated using a range of pH-varied phosphate buffers to ensure a ratiometric measurement relative to pH could be made.

The pH-responsive nanosensors were successfully delivered to the intracellular environment of primary myoblasts. Lipofectamine 2000 was explored as a potential nanosensor cargo delivery vector due to its successful routine use in conjunction with the myoblasts as a transfection reagent in knockdown studies. Transfection reagents have been reported as potential delivery tools in recent literature however with varying success (Clark *et al*. 1999b; Coupland *et al*. 2008). Clarke and co-workers reported that the use of Escort4 transfection reagent used to deliver $Ca^{2+}$-sensitive nanosensors to mouse blastocysts resulted in the almost exclusive membrane association of the nanosensors with the cell membrane. This was not observed with the myoblasts, as shown in Figure 4.5, the nanosensors appeared to be distributed throughout the whole cell, with the exception of the nucleus. It is possible that the cells with the best nanosensor internalisation properties were also the cells that sustained most damage to the extracellular matrix attaching the cells to the cover slip in both the 0.05% and 0.1% challenges. Other methods of delivery that have previously been investigated include GeneGun, Tat-mediated endocytosis and pico-injection (Clark *et al*. 1999a). Due to limitations on resources and time, the investigation of these internalisation techniques was beyond the scope of the study. Pico-injection is an invasive technique that involves physical perturbation of the cell membrane to deliver sensor to the cytoplasm. As each cell must be individually tethered and injected, the technique is not only potentially damaging to the cells but very labour intensive. Genegun 'biolistic' delivery has shown promise as an internalisation method resulting in an even spread of nanosensors within the cells. The technique requires optimisation between cell lines and as it has not been investigated in cultured myoblast cells, the success rate to population loss ratio following delivery is currently unknown. Optimisation would have to be carried out on immortalised myoblasts primarily as culture pressure on the primary myoblasts may be too high to accommodate the optimisation process. Tat-mediated endocytosis of the nanosensors requires amine functionalisation of the nanosensor matrix to provide functional groups for Tat conjugation. It has been reported that following internalisation the nanosensors remain membrane bound within a lysosome and are not free within the cytoplasm (Coupland *et al*. 2008). By co-loading cells with both Tat-conjugated nanosensors and the commercially available dye Lysotracker, Coupland and coworkers observed that the intracellular vesicles formed during sensor internalisation remained intact over the course of measurement.

The use of pH-sensitive nanosensors to quantify $pH_i$ has been previously reported, however as previously mentioned the measurements achieved suggested that the nanosensors were internalised within lysosomes (Coupland *et al*, 2008; Coupland *et al*. 2009). In this study the measurements achieved seem representative of the general intracellular environment. This could be corroborated by simultaneously using an alternative technique to confirm the $pH_i$, however as previously discussed $pH_i$ measurement techniques can be difficult to employ, destructive to the cells and prone to inaccuracy. True pH-sensitive microelectrodes have been in use since first described in 1974 by R.C. Thomas (Thomas 1974). The electrode comprised recessed pH-sensitive glass encased within insulating glass in such a way that only 1-2 µm of the electrodes tip needed to be placed within a cell to make measurements. Such microelectrodes remain in use now by researchers with the required level of skill and dexterity to manufacture such fine and delicate electrodes (Trenholm and Baldridge 2010). Due to relatively slow response times (~77 ± 15 s (Willoughby *et al*. 1998)) and manufacturing difficulties liquid ion exchange microelectrodes were developed with tips less than 1 µm in diameter and subsequently much faster response times (Ammann 1986; Khuri *et al*. 1974). Both of these techniques however require physical and sustained penetration of the cell membrane to make a measurement. As measurements recorded from the pH-sensitive electrode are a summation of both $pH_i$ and membrane potential, the membrane potential must also be quantified simultaneously with a separate electrode (Schweining *et al*. 1999). This can require an additional cell penetrating electrode to be used, increasing the risk of significant cell perturbation and cytoplasm 'leaks'. Although an accurate and continuous monitoring system, the microelectrodes require much practise and skill to employ successfully. The relatively frequent failure membrane potential monitoring also renders the $pH_i$ measurements achieved inaccurate following subtraction.

*In vivo* pH measurement using fMRI was built on the theory that inorganic phosphate (Pi) and phosphocreatine (pCr) display differential spectral resonances depending on the amount of protonation that occurs within the cells. This is known as chemical shift and is related to the pH surrounding the molecules or indeed, within the cells. The amount of chemical shift observed in pCR and Pi peaks measured using a magnetic resonance spectroscopy (MRS) technique, (such as nuclear magnetic resonance (NMR) or fMRI), can be used to calculate the intracellular pH (Madden et al, 1989). Unfortunately, the prohibitively high cost of fMRI analysis renders the technique redundant for *in vitro* investigations and the small mass of cultured cells means that fMRI cannot be practically employed. Recent advances regarding 'in-cell NMR' however may well provide a reliable albeit highly specialised and expensive method for intracellular pH measurement (Serber and Dötsch, 2001).

The $pH_i$ values reported by the nanosensors appear to be slightly lower than previously reported, ranging from 6.5 – 7 in non-CFS cells, as opposed to 7 – 7.4 as previously described by other methods (Jones *et al*. 2010; Juel 2008). The Jones *et al* study however is concerned with monitoring *in vivo* intramuscular $pH_i$ using a fMRI based technique. When measuring cultured cells, the extracellular environment is very static, with neither active perfusion to carry away effluxed protons nor the high buffering capacity of blood plasma or interstitial fluid to aid homeostatic control. It is possible that this lack of proton clearing worked to keep the $pH_i$ values observed artificially low. In Figures 4.8 and 4.9 a general, if not significant, upwards trend was observed for pH measurements from all treatment groups, including the controls. This could have been brought about simply by refreshing the culture medium at the beginning of the experiment, clearing effluxed protons that had accumulated since the previous culture medium change. Steps to combat this issue could be taken though the integration of the cell testing platform with a simple continuous microfluidic perfusion system that would clear spent medium and reduce the risk of static cell acidosis as a consequence of culture technique.

The fact that pH changes following treatment of CFS cells with DCA were observed suggests that in the culture tested there may be some malfunction of normal pyruvate metabolism. Considering that DCA prevents the phosphorylation of PDC though inhibition of PDH kinase, increasing the turnover of PDC as a consequence, the issue may lie in reduced functionality of PDH within PDC, or over-activity of PDH kinase. Both of these conditions would lead to reduced pyruvate metabolism and an accumulation of lactic acid within the affected cells.

In summary, ratiometric pH-sensitive nanosensors were readily internalised by the cells using a simple, minimally destructive and relatively cost effective technique, offering a facile and minimally invasive alternative to microelectrodes. It would be useful however to compare the $pH_i$ measurements made using the nanosensors with those made using a $pH_i$ microelectrode from the primary myoblasts used in this study. This would give the unique opportunity to corroborate and potentially intracellularly calibrate the pH nanosensors. The optical and electrical systems are highly compatible, there is scope to monitor $pH_i$ with both a microelectrode and nanosensors simultaneously providing the two techniques are spatially compatible.

## 4.5 References

Ammann, D., 1986. Ion-selective microelectrodes. Springer-Verlag, Berlin.

Buck, S.M., Koo, Y.E., Park, E., Xu, H., Philbert, M.A., Brasuel, M.A., Kopelman, R., 2004. Optochemical nanosensor PEBBLEs: photonic explorers for bioanalysis with biologically localised embedding. Current Opinion in Chemical Biology 8(5), 540-546.

Christof, J.S., S. Egginton, E.W.T., Raven, J.A., 1999. Measurement of intracellular pH: a comparison between ion-sensitive microelectrodes and fluorescent dyes in the regulation of tissue pH in plants and animals. Cambridge University Press.

Clark, H.A., Hoyer, M., Philbert, M.A., Kopelman, R., 1999a. Optical nanosensors for chemical analysis inside single living cells. 1. Fabrication, characterization, and methods for intracellular delivery of PEBBLE sensors. Analytical Chemistry 71(21), 4831-4836.

Clark, H.A., Kopelman, R., Tjalkens, R., Philbert, M.A., 1999b. Optical nanosensors for chemical analysis inside single living cells. 2. Sensors for pH and calcium and the intracellular application of PEBBLE sensors. Analytical Chemistry 71(21), 4837-4843.

Coupland, P.G., Fisher, K.A., Jones, D.R., Aylott, J.W., 2008. Internalisation of polymeric nanosensors in mesenchymal stem cells: analysis by flow cytometry and confocal microscopy. Journal of Controlled Release 130(2), 115-120.

Coupland, P.G., Briddon, S.J., Aylott, J.W., 2009. Using fluorescent pH-sensitive nanosensors to report their intracellular location after Tat-mediated delivery. Integrative Biology 1(4), 318-323.

Fouque, F.O., Brivet, M., Boutron, A., Vequaud, C., Marsac, C.C., Zabot, A.N.D.M.-T.R.S., Benelli, C., 2003. Differential effect of DCA treatment on the pyruvate dehydrogenase complex in patients with severe PDHC deficiency. Pediatric Research 53(5), 793-799.

Graber, M.L., DiLillo, D.C., Friedman, B.L., Pastoriza-Munoz, E., 1986. Characteristics of fluoroprobes for measuring intracellular pH. Analytical Biochemistry 156(1), 202-212.

Jones, D.E.J., Hollingsworth, K.G., Taylor, R., Blamire, A.M., Newton, J.L., 2010. Abnormalities in pH handling by peripheral muscle and potential regulation by the autonomic nervous system in chronic fatigue syndrome. Journal of Internal Medicine 267(4), 394-401.

Juel, C., 2008. Regulation of pH in human skeletal muscle: adaptations to physical activity. Acta Physiologica 193(1), 17-24.

Khuri, R.N., Bogharian, K.K., Agulian, S.K., 1974. Intracellular bicarbonate in single skeletal muscle fibers. European Journal of Physiology 349(4), 285-294.

Madden, A., Leech, M.O., Collins, D.J., 1989. pH calibration curve at 1.5 Tesla. Physical and Medical Biology 34(9), 1289-1293

Randolph, L.M., Jackson, H.A., Wang, J., Shimada, H., Sanchez-Lara, P.A., Wong, D.A., Wong, L.-J., Boles, R.G., 2011. Fatal infantile lactic acidosis and a novel homozygous mutation in the SUCLG1 gene: A mitochondrial DNA depletion disorder. Molecular Genetics and Metabolism 102(2), 149-152.

Robergs, R.A., Ghiasvand, F., Parker, D., 2004. Biochemistry of exercise-induced metabolic acidosis. American Journal of Physiology - Regulatory, Integrative and Comparative Physiology 287(3), R502-R516.

Robinson, B., 2006. Lactic acidaemia and mitochondrial disease. Molecular Genetics and Metabolism 89(1-2), 3-13.

Schweining, C.J., 1999. Measurement of intracellular pH: a comparison between ion-sensitive microelectrodes and fluorescent dyes. In: Egginton, S., Taylor, E. W., Raven J. A. (Ed.), Regulation of tissue pH in plants and animals: a reappraisal of current techniques pp. 1-12. Cambridge University Press, Cambridge.

Serber, Z., Dötsch, V,. 2001. In cell NRM spectroscopy. Biochemistry 40, 14317-14323.

Srivastava, A., Krishnamoorthy, G., 1997. Time-resolved fluorescence microscopy could correct for probe binding while estimating intracellular pH. Analytical Biochemistry 249(2), 140-146.

Thomas, R.C., 1974. Intracellular pH of snail neurones measured with a new pH-sensitive glass micro-electrode. Journal of Physiology 238(1), 159-180.

Trenholm, S., Baldridge, W.H., 2010. The effect of aminosulfonate buffers on the light responses and intracellular pH of goldfish retinal horizontal cells. Journal of Neurochemistry 115(1), 102-111.

Willoughby, D., Thomas, R.C., Schwiening, C.J., 1998. Comparison of simultaneous pH measurements made with 8-hydroxypyrene-1,3,6-trisulphonic acid (HPTS) and pH-sensitive microelectrodes in snail neurones. European Journal of Physiology 436(4), 615-622.

# Chapter 5. Direct, real-time monitoring of superoxide generation in isolated mitochondria

**JR Henderson, H Swalwell, SJ Boulton, P Manning, CJ McNeil, MA Birch-Machin**

*Free Radical Research, September 2009; 43(9): 1-7*

## 5.1 Introduction

The primary function of mitochondria is to carry out oxidative phosphorylation. Complexes I-IV of the mitochondrial electron transport chain (mETC) transfer electrons from reduced substrates to oxygen, coupled to the creation of a proton gradient across the inner mitochondrial membrane (Chance and Mela 1966a, b, c). It is well established that the mETC is the major cellular generator of superoxide ($O_2^-$) as a result of leakage of single electrons, which reduce $O_2$ to form $O_2^-$ (Murphy 2009). Superoxide is the proximal reactive oxygen species (ROS) generated in mitochondria (Beckman and Ames 1998) and it can be readily converted into other ROS, as summarised in Figure 4.1. Reactive oxygen species are involved in a number of cellular processes under normal physiological conditions, such as cell signalling (Thannickal and Fanburg 2000). However, when cellular production of ROS exceeds the antioxidant capacity, $O_2^-$ and other ROS become a major cause of cellular oxidative damage. This ‘oxidative stress’ causes damage to macromolecules such as lipids, proteins and DNA (Orrenius *et al*. 2007) and it is a mechanism that has significance in many degenerative diseases as well as ageing (Brand *et al*. 2004). ROS within cells are known to act as secondary messengers in intracellular signalling cascades, which can induce and maintain the oncogenic phenotype of cancer cells (Cheeseman, 1993). Redox imbalances have been found to be present in many cancer cells compared with normal cells (Valko *et al*. 2006). Thus, redox imbalance may be related to oncogenic stimulation. There is evidence that most of the $O_2^-$ generated by the mETC originates from Complexes I and III (Raha and Robinson 2000), although the relative contribution of these Complexes to $O_2^-$ production and the possible involvement of other Complexes remains to be fully elucidated (Murphy 2009). Since $O_2^-$ is involved in many cellular processes both physiological and pathophysiological, direct, real-time monitoring of its production offers greater insight into the temporal and spatial aspects of $O_2^-$ generation in biological systems. A number of methods have been employed to monitor $O_2^-$ production *in vitro* including fluorescence (Chang *et al*. 2005b; Henderson and

Chappell 1993) and electrochemical techniques (Cooper *et al*. 1993; Manning *et al*. 1998; Aitken *et al*. 2007).

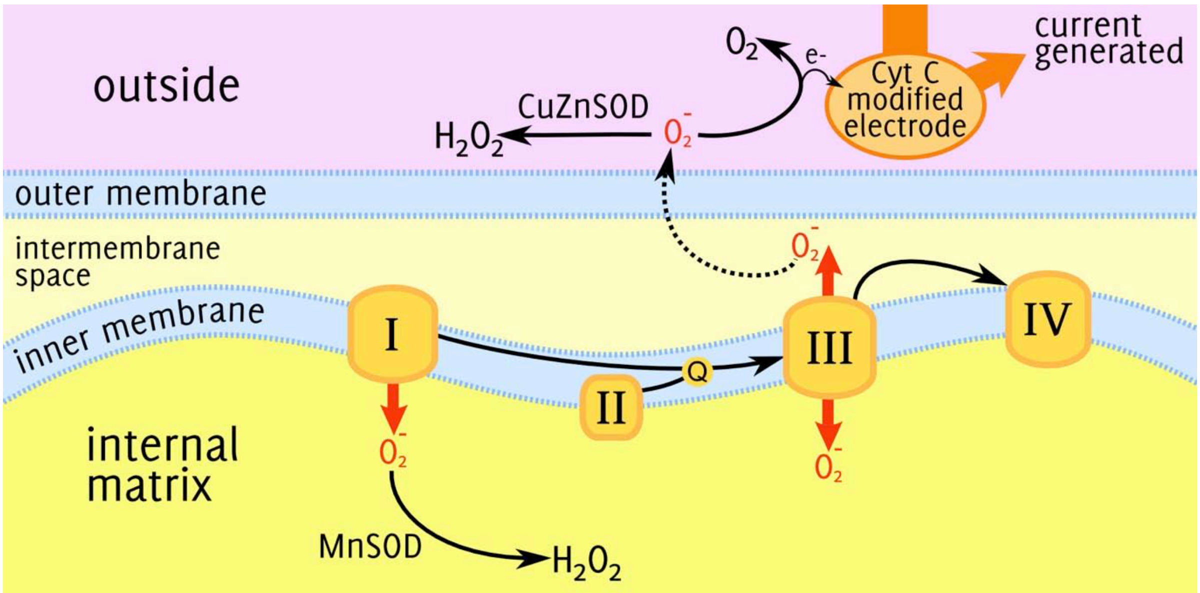

**Figure 5.1:** Generation of $O_2^-$ and other reactive oxygen species in the mitochondrial electron transport chain.

Mitochondria are the predominant source of $O_2^-$ generated in mammalian cells and, as such, monitoring the organelles directly offers the potential to enhance the understanding of cellular damage following increased $O_2^-$ production. The application of both fluorescence and electroparamagnetic resonance (EPR) methods have been used to monitor $O_2^-$ production in isolated mitochondria (Du *et al*. 1998; Elks *et al*. 2009; Mariappan *et al*. 2009; Xu and Arriaga 2009). However, amperometric sensors have not been used routinely for the direct, real-time monitoring of $O_2^-$ generation in isolated mitochondrial fractions. The covalent attachment of the redox protein cytochrome *c* to the surface of gold electrodes has been reported extensively for qualitative monitoring of $O_2^-$ dynamics *in vitro* (McNeil *et al*. 1989; Manning *et al*. 1998; Chang *et al*. 2005a; Chang *et al*. 2005b; Aitken *et al*. 2007). Such an approach offers a number of significant advantages over spectrophotometric or chemiluminescent methods. The principle advantage of this technique is the ability to measure $O_2^-$ production from whole cells or isolated organelles directly and in real-time. This overcomes the limitations of more traditional 'end-point' analyses that rely on the measurement of reaction products or adducts. In addition the high degree of selectivity that the amperometric electrode shows for $O_2^-$ in the presence of non-specific reducing agents such as ascorbic acid has been extensively reported (McNeil *et al*. 1989; Manning *et al*. 1998; Chang *et al*. 2005a; Chang *et al*. 2005b; Aitken *et al*. 2007). This selectivity has been primarily attributed to a low operating potential of

+100 mV *vs.* an Ag/AgCl reference electrode (McNeil *et al*. 1989; Manning *et al*. 1998). Additionally, measurements made with the electrode do not involve the addition of dyes or substrates into the cellular environment, which could adversely influence cellular observations. This Chapter reports the use of chronoamperometry to specifically detect, directly and in real-time $O_2^-$ production from the mitochondrial electron transport chain. A greater understanding of the role of mitochondrial $O_2^-$ production may ultimately lead to a fuller understanding of many important disease pathways and the identification of novel targets for drug therapy. The data presented herein clearly demonstrate the potential of a cytochrome *c* functionalised sensor to delineate these pathways.

## 5.2 Materials and methods

### 5.2.1 Reagents

Antimycin A, cytochrome *c*, rotenone, superoxide dismutase (SOD), xanthine and XOD were purchased from Sigma-Aldrich (Poole, UK). 3,3'-Dithiobis(sulphosuccinimidylpropionate) (DTSSP) was supplied by Pierce (Chester, UK).

### 5.2.2 Cell culture

The melanoma cell line FM55 (a kind gift from Professor Des Tobin, Bradford University, UK) was cultured in Dulbecco's modified Eagle's medium (Luna, UK) supplemented with 10% foetal calf serum, 100 $Uml^{-1}$ streptomycin (Invitrogen, UK), and 0.1 $mgml^{-1}$ penicillin (Invitrogen, UK), in a humidified atmosphere with 5% (v/v) $CO_2$ at 37˚C. The medium was changed every 2-3 days. Cells were grown to near confluence in $150cm^2$ flasks to six passages prior to isolation of mitochondria.

### 5.2.3 Mitochondrial fraction preparation

An enriched mitochondrial fraction was isolated from cultured cells by physical homogenization, differential centrifugation and treatment with hypotonic buffer. Cultured cells were harvested and washed with PBS. All subsequent procedures were carried out on ice or at 48˚C. The washed pellet was resuspended in 1ml of a sucrose rich mitoprep buffer (pH7.4) containing 250mM sucrose (Sigma-Aldrich, UK), 2mM HEPES (Sigma-Aldrich, UK) and 0.1mM EGTA (Sigma-Aldrich, UK) and disrupted by 20 passes in a power-driven Teflon-glass homogenizer. The homogenate was centrifuged for 10 min at 2200 rpm at˚C4 and the supernatant collected. The supernatant was then centrifuged at 11000 rpm for 10 min at 4˚C. The resulting pellet containing the mitochondrial fraction was re-suspended in mitoprep buffer and stored in aliquots at -80˚C until use (Kirby *et al*. 2007). The protein concentration was determined using the Bradford assay (Bio-Rad, UK) exactly according to the manufacturer's instructions. The isolated mitochondria were maintained in the sucrose-rich buffer during all electrochemical measurements.

### 5.2.4 Superoxide-responsive electrode preparation

The cytochrome *c* based $O_2^-$ electrode was prepared as previously described (Manning *et al*. 1998). In brief, a 2 mm O.D. solid gold electrode (BioAnalytical Systems, Cambridgeshire, UK) was polished using 0.02 mm aluminium oxide slurry on a 'micro-cloth' cleaning platform (BioAnalytical Systems, Cambridgeshire, UK) then sonicated for 5 min in ethanol. The electrode was then incubated in a 50mM solution of DTSSP for 5 min at room temperature before being gently rinsed in distilled water. Finally, the electrode was incubated in a 2mM cytochrome *c* solution (in PBS, pH 7.4) at°C4 overnight. The modified electrode was rinsed immediately before use and calibrated using the reaction between xanthine and XOD to generate $O_2^-$ as described previously (Cooper *et al*. 1993; Manning *et al*. 1998). For all amperometric measurements the electrode was coupled with a Ag/AgCl electrode that acted as both reference and counter electrode (Harvard Apparatus, Edenbridge, UK). The electrodes were connected to an in-house potentiostat interfaced with a PC coupled with data acquisition software. All measurements were carried out at an operating potential of +100mV (*vs.* Ag/AgCl). For calibration the functionalised electrode was placed in 990µl of 10mM xanthine solution (in 100mM KOH) and a steady baseline current response was recorded. To this 10µl of varying concentrations of XOD (0.5, 1, 2, 3, 4 or 5mM) were added and any change in current recorded as a function of time.

### 5.2.5 Monitoring superoxide generation from isolated mitochondria

The same electrode set-up was used for monitoring $O_2^-$ generation from isolated mitochondria as that described for calibrating the electrode. A 10ml suspension of isolated mitochondria (0.162 mgml$^{-1}$ protein concentration) was placed into a sterile conical well and the electrode lowered directly into the suspension, completely immersing the functionalised surface of the electrode. A steady baseline current response was recorded before adding 15 µl of either 100µM antimycin A or 100µM rotenone to inhibit mitochondrial Complex III or Complex I, respectively. Any subsequent current change was recorded. To demonstrate specificity of the electrode for $O_2^-$, the electrode was placed into 100 µl of isolated mitochondria (0.487 mgml$^{-1}$ protein concentration) and 15 µl of antimycin A was added. Approximately 30 s after the addition of antimycin A 15 µl of 7500 Uml$^{-1}$ SOD in PBS was added to scavenge any $O_2^-$ generated by the sample. As a further demonstration of specificity, the electrode was lowered into a 100 µl suspension of isolated mitochondria that already contained 7500 Uml$^{-1}$ SOD. As before, a steady baseline current response was observed before 15 µl of 100mM antimycin A was added.

## 5.3 Results

### 5.3.1 Superoxide electrode calibration

The generation of $O_2^-$ by enzymatic conversion of xanthine to uric acid by XOD has previously been used to calibrate the $O_2^-$ response of cytochrome *c*-functionalised gold electrodes (Manning *et al*, 1998; Henderson *et al*, 2009). In the present study the current density at steady-state was linearly dependent on the concentration of XOD in the presence of excess substrate ($y = 804.3x - 5.4$, $r=0.98686$, $n=3$).

### 5.3.2 Monitoring superoxide generation from isolated mitochondria

The production of $O_2^-$ by isolated mitochondria was monitored successfully using the cytochrome *c* functionalised electrode. Any change in current observed was directly proportional to the amount of $O_2^-$ present. Figure 5.2 represents two typical responses following inhibition of mitochondrial Complexes I and III. The inhibition of Complex III through the addition of antimycin A brought about an immediate increase in $O_2^-$ generation leading to a rapid increase in current which peaked at 45.68 nA above the pre-addition baseline (Figure 5.2A). The current response stabilised within 120 s and a continuous current of 2nA was observed for the remainder of each experiment. In contrast, inhibition of Complex I through the addition of rotenone induced a comparatively small increase in current, reaching a maximum of 4.64 nA above the pre-addition baseline value, indicating much lower peak $O_2^-$ generation (Figure 5.2B). In addition, the response returned to pre-stimulus baseline levels within 90 s.

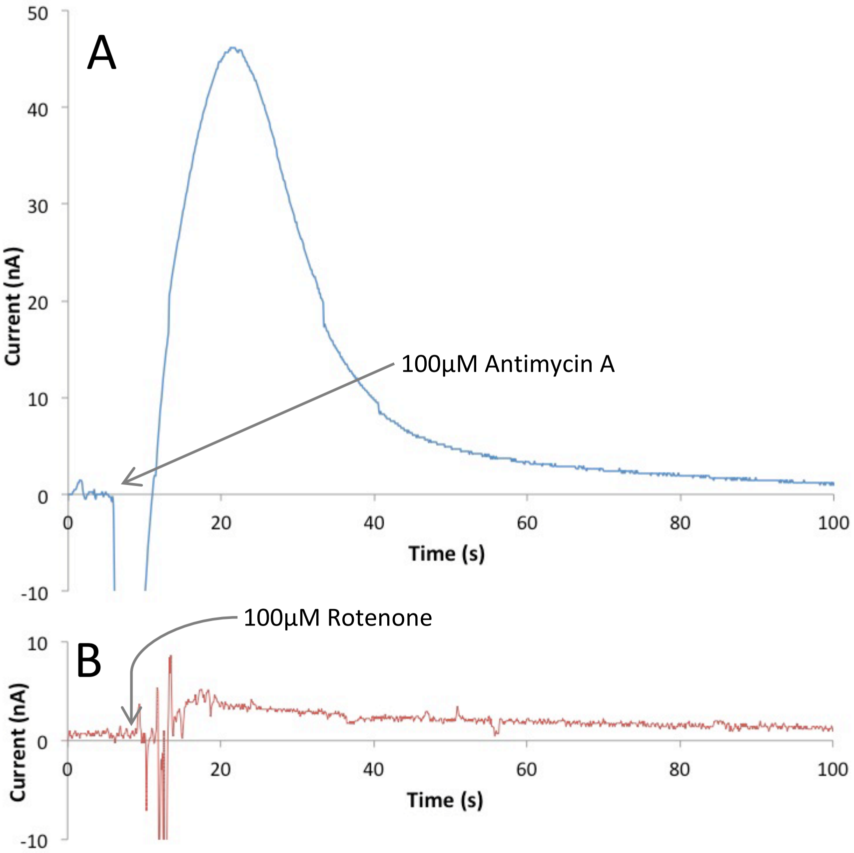

**Figure 5.2:** Respective traces of $O_2^-$ generation in isolated mitochondrial fractions following antimycin A (A) and rotenone (B) stimulation. The increase in current observed was proportional to the flux of $O_2^-$ generated during mitochondrial inhibition.

To demonstrate the specificity of the electrode for $O_2^-$, isolated mitochondria were stimulated with antimycin A, as this consistently elicited the largest $O_2^-$ response. As in Figure 5.2A, the addition of antimycin A to the isolated mitochondria sample induced a rapid increase in $O_2^-$ generation leading to a current peak 44.70nA above the pre-addition baseline. Approximately 30 s after the addition of antimycin A, 7500 U/ml SOD was added to the sample. The presence of the $O_2^-$ scavenger brought about an immediate decrease in current as the $O_2^-$ generated through the inhibition of Complex III was scavenged (Figure 5.3A). The current response re-stabilised below the original baseline value. The addition of antimycin A to mitochondrial samples already containing SOD did not induce an increase in $O_2^-$ generation detectable by the electrode (Figure 5.3B). A slight change in current was observed as the antimycin A was added to the sample, but the current returned to the baseline level within 5s.

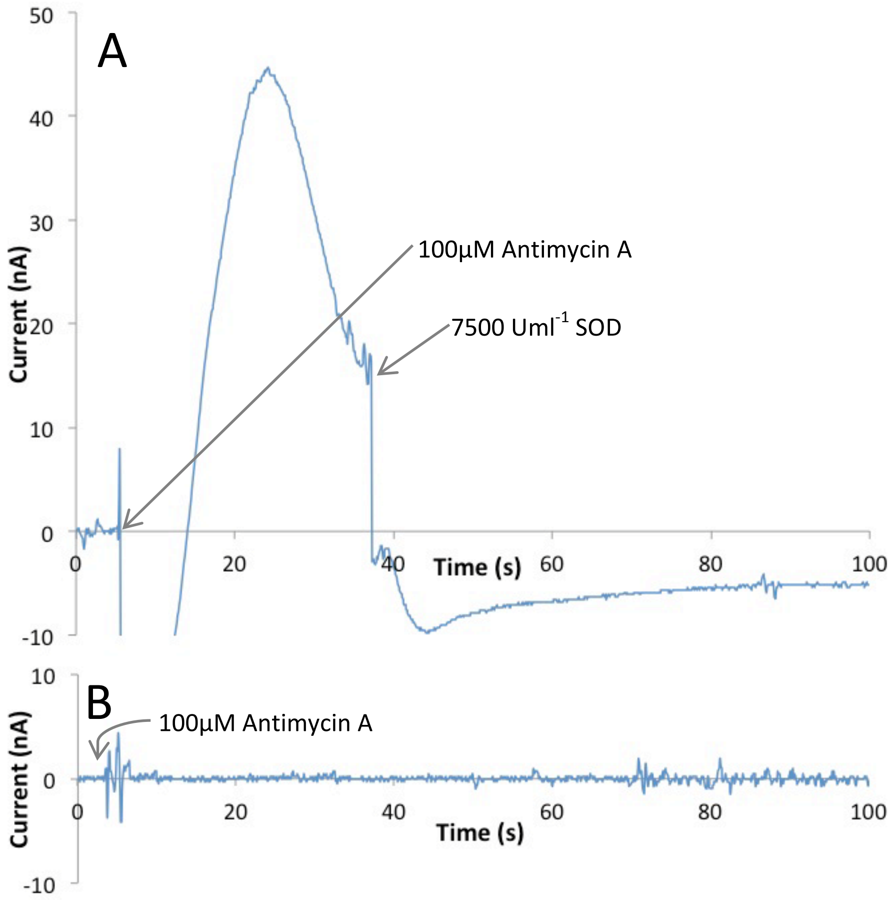

**Figure 5.3:** Scavenging of $O_2^-$ following the addition of 7500 UmL$^{-1}$ SOD to antimycin A-activated isolated mitochondria. The rapid decrease in current response following SOD addition demonstrates the specificity of the electrode for $O_2^-$ (A). No increase in $O_2^-$ generation was observed in response to antimycin A in isolated mitochondria samples that already contained SOD (B).

## 5.4 Discussion

In this study the application of a cytochrome *c* functionalised gold electrode to monitor $O_2^-$ production in isolated mitochondria has been reported. This method allowed the dynamics of mitochondrial $O_2^-$ release following the specific inhibition of Complex I and Complex III of the mETC to be examined comparatively and in real-time. Antimycin A is known to inhibit Complex III by binding to the Complex at centre 'I' and blocking the electron transfer from centre 'o' of the Q cycle, forming semi-quinone that reduces oxygen to $O_2^-$ (Brand *et al*. 2004). The large and immediate increase in $O_2^-$ production observed during the inhibition of Complex III with antimycin A (Figure 5.3A) is in keeping with this previously reported work (Brand *et al*. 2004; Muller *et al*. 2004; Xu and Arriaga 2009). Complex III is known to asymmetrically generate $O_2^-$ that passes both into the matrix and into the inter-membrane space of the mitochondrion. However, once formed, anionic $O_2^-$ is too strongly charged to readily cross the mitochondrial inner membrane (Han *et al*. 2001; Muller *et al*. 2004). Thus, superoxide production exhibits a distinct membrane sidedness or 'topology'. In addition, the electron acceptor associated with Complex III is cytochrome *c*, which is located on the outer part of the inner membrane and, therefore, explains the superoxide production into the inter-membrane space (Figure 5.1). Furthermore, it has been known for some time that partial turnover of the cyt bc1 components within Complex III in the presence of antimycin A, a Q(i) site inhibitor, results in accumulation of a semiquinone at the Q(o) site, which can result in superoxide production on the outer aspect of the inner membrane adjacent to the inter-membrane space (Birch-Machin and Turnbull 1993; Birch-Machin 2008). As a result of these combined features the $O_2^-$ detected by the electrode will be that released outside the inner membrane (Figure 5.1). This sidedness or topology of $O_2^-$ production is the basis for the measurement of $O_2^-$ production at Complex III using the end-point EPR spin trap, 5,5-dimethyl-1-pyrroline N-oxide (DMPO), which, like the gold electrode employed in these studies, is external to the mitochondria and detects increased $O_2^-$ production effluxed outward following addition of antimycin A (O'Malley *et al*. 2006). Superoxide generation at Complex I can be attributed to electron leakage at the quinone binding site (Lambert and Brand 2004) and in the presence of a Q-site inhibitor (such as rotenone) the rate of $O_2^-$ production can increase 10-30-fold (Lambert and Brand 2004). In detail, rotenone is believed to block electron transfer from the N2 iron-sulphur cluster to ubiquinone

(Ohnishi *et al*. 2005). However, $O_2^-$ generated at Complex I was released exclusively into the mitochondrial matrix (St-Pierre *et al*. 2002; Lambert and Brand 2004; Raijmakers *et al*. 2004b). This resulted in the observation of a much reduced $O_2^-$ flux from the mitochondria following treatment with rotenone due to not only the additional diffusional barrier imposed by the inner membrane, but also the membrane's relative impermeability to highly charged molecules compared with the outer membrane. The low permeability of the mitochondrial membrane to $O_2^-$ would suggest that no $O_2^-$ would be detected by the electrode following the addition of rotenone, yet the change in current observed demonstrates that some $O_2^-$ was produced (Figure 5.2B). Dispite the asymmetry of rotenone induced $O_2^-$ flux the increase in current observed should have been proportional to the flux of $O_2^-$ generated during mitochondrial inhibition that could be detected by the electrochemical method. Consistent with this, inhibition of Complex I by rotenone (Figure 5.2B) produced a much smaller change in current than that observed during Complex III inhibition (Figure 5.2A). The $O_2^-$ detected following the addition of rotenone may have been generated from upstream sites in Complex I, as the site of action for rotenone is thought to be in the distal position of the complex (O'Malley *et al*. 2006). In this respect there is good evidence from inhibitor analysis studies (Doughan and Dikalov 2007) showing efficient redox cycling at two sites within Complex I, one proximal and one distal to the putative rotenone binding site. Alternatively, the $O_2^-$ produced could be derived from semi-quinone formation at Complex III, as reported by O'Malley *et al*. (2006). Further investigation into the mechanisms of Complex I-associated $O_2^-$ production may clarify the findings reported in these studies. The *in vitro* specificity of the electrode for $O_2^-$ has been reported previously (Manning *et al*. 1998; Chang *et al*. 2005a; Chang *et al*. 2005b) and this was confirmed in this study through the addition of SOD before and after induction of $O_2^-$ generation (Figure 5.3A and B). The re-stabilization of the current response at a level below the pre-inhibition baseline observed in Figure 5.3A can be accounted for by the presence of $O_2^-$ in the sample prior to antimycin A addition. Electrons would have been 'leaking' from the mETC at low levels, therefore generating small amounts of $O_2^-$ in the mitochondrial sample as the electrode was polarizing to a steady baseline current response. As SOD has such a high affinity for $O_2^-$, scavenging of the radical would have been comprehensive leading to a decrease in current response below the initial baseline value as most of the $O_2^-$ present in the sample was completely scavenged. The specificity of the electrode was further confirmed by the presence of SOD prior to induction of $O_2^-$ generation (Figure 5.4B). By including SOD in the sample before inhibiting the mETC, any $O_2^-$ generated would be scavenged before reaching the cytochrome *c* immobilised at the electrode surface, hence no change in current response was recorded. Importantly, the addition of SOD also demonstrated that the electrode was not responsive to $H_2O_2$, which is spontaneously generated during the dismutation of $O_2^-$. It is worth noting that the current response observed following the addition of both rotenone and antimycin A to isolated mitochondria was much larger than would be expected in whole cell samples (Manning *et al*. 1998; Chang *et al*. 2005a; Aitken *et al*. 2007). This is not surprising considering that the antioxidant mechanisms that exist in cellular systems are not present in the mitochondrial fractions and $O_2^-$ is rapidly converted to $H_2O_2$ by MnSOD in the mitochondrial matrix (Fridovich 1995) or by Cu/ZnSOD in the intermembranal space and cytosol (Okado-Matsumoto and Fridovich 2001). All cytosolic SOD was removed when the mitochondria were isolated from their normal cellular environment and there is evidence to suggest that any residual Cu/ZnSOD becomes inactive in isolated mitochondria (Inarrea *et al*. 2005; Meany *et al*. 2007). It is therefore important to stress that all $O_2^-$ production observed in this study was representative of the mitochondria as the $O_2^-$ released should not be converted to $H_2O_2$ nor can it have been associated with other cellular $O_2^-$ generating processes such as NADPH oxidase, cytochrome P-450 or XOD (Raijmakers *et al*. 2004a, Griendling *et al*, 2003, Stokes *et al*, 2001).

In conclusion, amperometric $O_2^-$ detection has been successfully applied to isolated mitochondrial fractions. The rapid decrease in current response following SOD addition demonstrated the specificity of the electrode for $O_2^-$ (Figure 5.4A). No increase in $O_2^-$ generation was observed in response to antimycin A in isolated mitochondria samples that already contained SOD (Figure 5.4B). Generation of $O_2^-$ following specific inhibition of mitochondrial Complex I and Complex III was performed and the observations were in keeping with previous studies (Taylor *et al*. 1994; Han *et al*. 2001; Muller *et al*. 2004; Ohnishi *et al*. 2005; Xu and Arriaga 2009). A possible future application of this detection method would be to examine $O_2^-$ profiles of disease state cells *vs.* wild-type cells *in vitro* and through the use of isolated mitochondrial fractions. However, it must be stressed that the capacity of cells or tissues to generate $O_2^-$ will vary and this is influenced by factors such as age and localised concentrations of $O_2^-$ producing enzymes. In addition, future studies must also consider the degree of control that the activity of the individual enzyme complex (i.e. Complex I *vs.* Complex III) exerts on the whole pathway of electron transfer along the respiratory chain in the mitochondria. Using inhibitor analysis studies, it has been shown previously that Complex III exerts a different degree of control even between different cell types (muscle *vs.* liver) (Taylor *et al*. 1994). It is, therefore, very difficult to extrapolate $O_2^-$ generation data acquired from isolated mitochondrial fractions into *in vitro* $O_2^-$ production. However, the data presented in this study has clearly demonstrated the analytical capabilities of amperometric sensing for the direct, real-time analysis of qualitative $O_2^-$ generation from isolated mitochondria following the chemical modulation of electron transport complexes. This sensing technology has clear potential to greatly improve the current understanding of $O_2^-$ flux *in vitro*.

## 5.5 References

Aitken, G.R., Henderson, J.R., Chang, S.C., McNeil, C.J., Birch-Machin, M.A., Direct monitoring of UV-induced free radical generation in HaCaT keratinocytes. Clinical and Experimental Dermatology 32(6), 722-727.

Beckman, K.B., Ames, B.N., 1998. The free radical theory of aging matures. Physiological Reviews 78(2), 547-581.

Birch-Machin M.A., Turnbull D.M., 1993. Methods in Toxicology. In: Jones D, L.L. (Ed.), Defects at coupling site II, pp. 324-336. Wiley, San Diego.

Birch-Machin, M.A., 2008. Assessment of mitochondrial respiratory function *in vitro* and *in vivo*. Drug-Induced Mitochondrial Dysfunction, pp. 383-395. John Wiley and Sons, Inc.

Brand, M.D., Affourtit, C., Esteves, T.C., Green, K., Lambert, A.J., Miwa, S., Pakay, J.L., Parker, N., 2004. Mitochondrial superoxide: production, biological effects, and activation of uncoupling proteins. Free Radical Biology & Medicine 37(6), 755-767.

Chance, B., Mela, L., 1966a. Hydrogen ion concentration changes in mitochondrial membranes. Journal of Biological Chemistry 241(20), 4588-4599.

Chance, B., Mela, L., 1966b. A hydrogen ion concentration gradient in a mitochondrial membrane. Nature 212(5060), 369-372.

Chance, B., Mela, L., 1966c. Proton movements in mitochondrial membranes. Nature 212(5060), 372-376.

Chang, S.C., Pereira-Rodrigues, N., Henderson, J.R., Cole, A., Bedioui, F., McNeil, C.J., 2005a. An electrochemical sensor array system for the direct, simultaneous *in vitro* monitoring of nitric oxide and superoxide production by cultured cells. Biosensors & Bioelectronics 21(6), 917-922.

Chang, S.C., Rodrigues, N.P., Zurgil, N., Henderson, J.R., Bedioui, F., McNeil, C.J., Deutsch, M., 2005b. Simultaneous intra- and extracellular superoxide monitoring using an integrated optical and electrochemical sensor system. Biochemical & Biophysical Research Communications 327(4), 979-984.

Cheeseman, K.H., 1993, Mechanisms and effects of lipid peroxidation. Molecular Aspects of Medicine 14(3), 191-7.

Cooper, J.M., Greenough, K.R., McNeil, C.J., 1993. Direct electron transfer reactions between immobilised cytochrome *c* and modified gold electrodes. Journal of Electroanalytical Chemistry 347(1-2), 267-275.

Doughan, A.K., Dikalov, S.I., 2007. Mitochondrial redox cycling of mitoquinone leads to superoxide production and cellular apoptosis. Antioxidants & Redox Signaling 9(11), 1825-1836.

Du, G., Mouithys-Mickalad, A., Sluse, F.E., 1998. Generation of superoxide anion by mitochondria and impairment of their functions during anoxia and reoxygenation *in vitro*. Free Radical Biology & Medicine 25(9), 1066-1074.

Elks, C.M., Mariappan, N., Haque, M., Guggilam, A., Majid, D.S., Francis, J., 2009. Chronic NF-κB blockade reduces cytosolic and mitochondrial oxidative stress and attenuates renal injury and hypertension in SHR. American Journal of Physiology: Renal Physiology 296(2), 298-305.

Fridovich, I., 1995. Superoxide radical and superoxide dismutases. Annual Review of Biochemistry 64, 97-112.

Griendling K.K., FitzGerald G.A., 2003. Oxidative stress and cardiovascular injury: part I: Basic mechanisms and *in vivo* monitoring of ROS. Circulation 108,1912-1916.

Han, D., Williams, E., Cadenas, E., 2001. Mitochondrial respiratory chain-dependent generation of superoxide anion and its release into the intermembrane space. Biochemical Journal 353(2), 411-416.

Henderson, L.M., Chappell, J.B., 1993. Dihydrorhodamine 123: a fluorescent probe for superoxide generation? European Journal of Biochemistry 217(3), 973-980.

Inarrea, P., Moini, H., Rettori, D., Han, D., Martinez, J., Garcia, I., Fernandez-Vizarra, E., Iturralde, M., Cadenas, E., 2005. Redox activation of mitochondrial intermembrane space Cu,Zn-superoxide dismutase. Biochemical Journal 387(1), 203-209.

Kirby, D.M., Thorburn, D.R., Turnbull, D.M., Taylor, R.W., 2007. Biochemical assays of respiratory chain complex activity. Methods in Cell Biology 80, 93-119.

Lambert, A.J., Brand, M.D., 2004. Inhibitors of the quinone-binding site allow rapid superoxide production from mitochondrial NADH:ubiquinone oxidoreductase (Complex I). Journal of Biological Chemistry 297, 39414-39420.

Manning, P., McNeil, C.J., Cooper, J.M., Hillhouse, E.W., 1998. Direct, real-time sensing of free radical production by activated human glioblastoma cells. Free Radical Biology & Medicine 24(7-8), 1304-1309.

Mariappan, N., Elks, C.M., Fink, B., Francis, J., 2009. TNF-induced mitochondrial damage: a link between mitochondrial Complex I activity and left ventricular dysfunction. Free Radical Biology & Medicine 46(4), 462-470.

McNeil, C.J., Smith, K.A., Bellavite, P., Bannister, J.V., 1989. Application of the electrochemistry of cytochrome *c* to the measurement of superoxide radical production. Free Radical Research Communications 7(2), 89-96.

Meany, D.L., Thompson, L., Arriaga, E.A., 2007. Simultaneously monitoring the superoxide in the mitochondrial matrix and extramitochondrial space by micellar electrokinetic chromatography with laser-induced fluorescence. Analytical Chemistry 79(12), 4588-4594.

Muller, F.L., Liu, Y., Van Remmen, H., 2004. Complex III releases superoxide to both sides of the inner mitochondrial membrane. Journal of Biological Chemistry 279(47) 49064-49073.

Murphy, M.P., 2009. How mitochondria produce reactive oxygen species. Biochemical Journal 417(1), 1-13.

O'Malley, Y., Fink, B.D., Ross, N.C., Prisinzano, T.E., Sivitz, W.I., 2006. Reactive oxygen and targeted antioxidant administration in endothelial cell mitochondria. Journal of Biological Chemistry 281(52), 39766-39775.

Ohnishi, S.T., Ohnishi, T., Muranaka, S., Fujita, H., Kimura, H., Uemura, K., Yoshida, K.-i., Utsumi, K., 2005. A possible site of superoxide generation in the Complex I segment of rat heart mitochondria. Journal of Bioenergetics & Biomembranes 37(1), 1-15.

Okado-Matsumoto, A., Fridovich, I., 2001. Subcellular distribution of superoxide dismutases (SOD) in rat liver: Cu,Zn-SOD in mitochondria. Journal of Biological Chemistry 276(42), 38388-38393.

Orrenius, S., Gogvadze, V., Zhivotovsky, B., 2007. Mitochondrial oxidative stress: implications for cell death. Annual Reviews in Pharmacological Toxicology 47, 143-183.

Raha, S., Robinson, B.H., 2000. Mitochondria, oxygen free radicals, disease and ageing. Trends Biochemical Science 25(10), 502-508.

Raijmakers, M.T., Peters, W.H., Steegers, E.A., Poston, L., 2004a. NAD(P)H oxidase associated superoxide production in human placenta from normotensive and pre-eclamptic women. Placenta 25 (Suppl A), S85-89.

Raijmakers, M.T., van Tits, B.J., Hak-Lemmers, H.L., Roes, E.M., Steegers, E.A., Peters, W.H., 2004b. Low plasma levels of oxidised low density lipoprotein in preeclampsia. Acta Obstetricia et Gynecologica Scandinavica 83(12), 1173-1177.

St-Pierre, J., Buckingham, J.A., Roebuck, S.J., Brand, M.D., 2002. Topology of Superoxide Production from Different Sites in the Mitochondrial Electron Transport Chain. Journal of Biological Chemistry 277(47), 44784-44790.

Stokes K.Y., Clanton E.C., Russell J.M., Ross C.R., Granger D.N., 2001. NAD(P)H oxidase-derived superoxide mediates hypercholes-terolemia-induced leukocyte-endothelial cell adhesion. Circulation Research 88,499-505

Taylor, R.W., Birch-Machin, M.A., Bartlett, K., Lowerson, S.A., Turnbull, D.M., 1994. The control of mitochondrial oxidations by Complex III in rat muscle and liver mitochondria. Implications for our understanding of mitochondrial cytopathies in man. Journal of Biological Chemistry 269: 3523-3528.

Thannickal, V.J., Fanburg, B.L., 2000. Reactive oxygen species in cell signaling. American Journal of Physiology -Lung Cell & Molecular Physiology 279(6), L1005-1028.

Valko, M., Rhodes, C.J., Moncol, J., Izakovic, M., Mazur, M., 2006. Free radicals, metals and antioxidants in oxidative stress-induced cancer. Chemico-Biological Interactions 160(1), 1-40.

Xu, X., Arriaga, E.A., 2009. Qualitative determination of superoxide release at both sides of the mitochondrial inner membrane by capillary electrophoretic analysis of the oxidation products of triphenylphosphonium hydroethidine. Free Radical Biology & Medicine 46(7), 905-913.

# Chapter 6. Real-time monitoring of superoxide generation and cytotoxicity in neuroblastoma mitochondria induced by 1-trichloromethyl-1,2,3,4-tetrahydro-beta-carboline.

**S. Boulton, P. Keane, C. Morris, C.J. McNeil, P. Manning**

*Manuscript submitted for consideration to Redox Report, December 2011*

## 6.1 Introduction

The mechanisms underlying the long-term progenesis of Parkinson's disease (PD) are not fully understood, although recent research has provided evidence for the involvement of a host of exogenous compounds and their endogenously generated metabolites (Langston and Ballard, 1984). A loss of dopaminergic neurons in the *substantia nigra pars compacta* is characteristic of the progressive neurodegeneration intrinsic to the PD phenotype (German *et al*, 1989). It is now widely accepted that 1-methyl-4-phenyl-1,2,3,6-tetrahydropyridine (MPTP), an impurity found in illicitly prepared caches of meperidine, can cause selective neural damage in the nigrostriatum (Langston and Ballard, 1983). Selective uptake of the MPTP metabolite $MPP^+$ by the plasma membrane dopamine transporter (DAT) concentrates the toxin within dopaminergic neurons (Javitch at el, 1985) where it is capable of causing massive oxidative damage to DNA and cellular proteins via inhibition of Complex I of the mETC (Cleeter *et al*, 1992; Hartley *et al*, 1994; Swerdlow *et al*, 1996) This discovery promoted the investigation of chemically similar potentially neurotoxic compounds in an attempt to establishing a link between environmental toxin exposure and the PD phenotype. Chloral hydrate and trichloroethylene are two such compounds that were identified as having neurotoxic potential due to their metabolism to chloral after administration. Although the precise mechanism by which chloral induces CNS depression has not yet been fully elucidated, metabolic investigations have uncovered the generation of species with mitochondria disrupting potential, one of which was 1-trichloromethyl-1,2,3,4-tetrahydro-beta-carboline (TaClo). TaClo is formed *in vivo* through the spontaneous reaction of endogenous tryptamine (‘Ta’) with chloral (trichloroacetaldehyde; ‘Clo’). TaClo has been shown in many recent publications to inhibit Complex I of the mETC in a manner comparable to $MPP^+$ (Janetzky *et al*, 1999; Bringmann *et al*, 1995; Kochen *et al*, 2003; Akundi *et al*, 2004) and DPI (Majander *et al*, 1994), a chemical to which TaClo bears striking structural similarity (Figure 6.1), resulting in an increase in cellular damage through the generation of large amounts of ROS. Complexes I and III of the mETC have previously been shown to generate $O_2^-$ immediately following exposure to known inhibitors rotenone and antimycin A (Henderson *et al*, 2009). All studies to date pertaining to the quantification of TaClo mediated mitochondrial ROS generation have been reliant on endpoint studies of the effects of ROS upon cellular components such as DNA, glutathione and enzyme up-regulation (Storch *et al*, 2006). These studies were limited by their inability to monitor the generation of potentially cytotoxic ROS directly and in real-time making temporal resolution of their production very challenging. Additionally, traditional measurement techniques do not allow differentiation between the various ROS produced by the mitochondria.

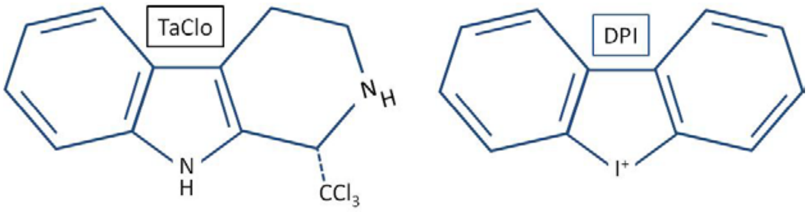

**Figure 6.1** Structural similarity between known Complex I inhibitor DPI and proposed neurotoxin TaClo corroborated the ability of TaClo to act as a mETC inhibitor.

The current study aimed to demonstrate whether TaClo was capable of eliciting measureable $O_2^-$ production in cultured neuroblastoma cells. The study focussed on changes in whole cell respiration as well as the real-time detection of $O_2^-$ flux from isolated mitochondria exposed to TaClo and other Complex I inhibitors. Many studies cite the timescale of action of TaClo as being up to 72 h post-administration before significant effects are observed (Storch *et al*, 2006), however other mETC inhibitors such as rotenone and antimycin A have been shown to act upon the mitochondria within seconds (Storch *et al*, 2006). The vital dye resazurin was used in the current study to assess the ability of TaClo to affect whole cell respiration. Unlike more conventional regents used in assessing cell respiration and viability (e.g. (3-(4,5-dimethylthiazol-2-yl)-2,5-diphenyltetrazolium bromide (MTT)), resorufin, the product of resazurin metabolism, is soluble and non-toxic. This eliminated the need for dye solubilisation prior to reading and reduced result ambiguity caused by toxic intracellular dye generation (O'Brien *et al*, 2000). The use of resazurin thus provided an ideal method with which real-time cellular respiratory rates in intact cells could be measured.

Using an $O_2^-$ selective electrode it was also possible to monitor in real-time the flux of $O_2^-$ generated from isolated mitochondria following treatment with TaClo. This technique has been previously used to monitor the ability of both rotenone and antimycin A to elicit $O_2^-$ production from human melanocyte derived mitochondria (Henderson *et al*, 2009). Electrochemical monitoring of $O_2^-$ offers many advantages over more indirect and non-specific methods, for example the use of chemiluminescent dyes and end-point assays, which relate primarily to the high selectivity of the electrode for $O_2^-$ (Tammeveski *et al*, 1998). Unlike various luminescent and fluorescent dyes, the electrode is capable of discriminating between reactive oxygen species (ROS) and can only generate a measureable current through interaction with $O_2^-$. The functionalisation of gold electrodes with the redox protein cytochrome *c* has been extensively used to monitor $O_2^-$ flux *in vitro* (Henderson *et al*, 2009, Chang *et al*, 2005, Manning *et al*, 2001). Previous studies have attributed $O_2^-$ specificity to the site-directed immobilization of the protein and the low operating potential used to re-oxidize the cytochrome *c* (Tammeveski *et al*, 1998).

The current study used a vital dye based optical detection method to continuously monitor the short-term effects of TaClo upon neuroblastoma whole cell respiration in conjunction with an amperometric $O_2^-$ detection technique which was used to selectively monitor TaClo induced $O_2^-$ flux from isolated mitochondria. The integration of these data sets has provided new evidence for the involvement of TaClo in the cumulative oxidative damage observed in progressive neurodegenerative disorders.

## 6.2 Materials and methods

### 6.2.1 Reagents

Cell culture reagents were all purchased from PAA (Somerset, UK). The thiol cross-linker 3-3'-dithiobis(sulphosuccinimidylpropionate) (DTSSP) was supplied by Pierce (Chester, UK). TaClo was purchased from Exclusive Chemistry Ltd. (Obninsk, Russia). All other reagents were purchased from Sigma Aldrich (Poole, UK).

### 6.2.2 Cell culture

The three times cloned human neuroblastoma cell line SH-SY5Y was routinely cultured using antibiotic-free Dulbecco's Modified Eagles Medium supplemented with 10% foetal calf serum (FCS) and 1% non essential amino acids (PAA, UK). Cells were maintained in a humidified environment containing 5% (v/v) $CO_2$ at 37°C throughout. Cells were grown to 80% confluence and were passaged five times over the course of experimentation, with mitochondrial isolation occurring at the third and fifth passage.

### 6.2.3 Real-time assessment of whole cell respiratory rate

Cells were seeded into black-walled, clear-bottomed 96 well plates at a density of $1x10^3$ cells/well and allowed to attach overnight. The growth medium was subsequently replaced with either 0.001% (w/v) resazurin salt in PBS or 0.001% (w/v) resazurin salt in PBS doped with 100 µM TaClo. An initial baseline fluorescence measurement was made immediately after medium replacement ($\lambda_{ex}$ 530 nm, $\lambda_{em}$ 590 nm) using an Infinite M200 fluorimeter (Tecan, UK) with associated Magellan control software. After 1 h incubation, fluorescence measurements were taken using the same parameters. This was repeated on an hourly basis for two further measurements. The cells were kept in the routine culture environment between readings.

### 6.2.4 Mitochondrial fraction preparation

Mitochondrial fractions were prepared as previously reported by Henderson *et al* (Henderson *et al*, 2009). Briefly, cells grown to 80% confluence were trypsinised and washed in phosphate buffered saline (PBS). After resuspension in sucrose-rich mitoprep buffer (250 mM sucrose, 2 mM HEPES and 0.1 mM EGTA, pH 7.4), the outer cell membranes were disrupted using 20 passes with a power driven Teflon-glass homogenizer. The resulting homogenate was centrifuged at 2200 rpm and 4°C for 10 min, after which the supernatant was decanted and further centrifuged at 11000 rpm and 4°C for 10 min. The resulting mitochondria -containing pellet was re-suspended in fresh mitoprep buffer then snap frozen in liquid nitrogen and stored at -80°C in 20 µl aliquots until required. Prior to use, the protein concentration of the mitochondria-containing sample was determined using a Bradford assay (Bio-Rad, UK) as per the manufacturer's instructions. Mitochondria were kept in sucrose-rich buffer throughout all electrochemical experiments.

### 6.2.5 Preparation of $O_2^-$ specific electrode

The electrode was functionalised as previously described (Manning *et al*, 1998). The surface of a 2 mm diameter gold electrode (BioAnalytical Systems, Cambridgeshire, UK) was polished using 0.02 µm aluminium oxide crystal slurry on a micro-cleaning cloth (BioAnalytical Systems, Cambridgeshire, UK). The electrode surface was further cleaned by sonication in 100% ethanol for 5 min. After rinsing with deionised water, the electrode was first incubated in 50 mM DTSSP for 5 min at room temperature, then thoroughly rinsed and incubated overnight in 2 mM cytochrome *c* at 4°C. After thorough rinsing to remove unbound protein, the electrode was ready for use. For all experiments, the electrode was poised at an operating potential of +100mV versus a Ag/AgCl reference electrode (Pierce, UK), which also served as the counter electrode. A bespoke 2-channel potentiostat was used and data was acquired using PicoLog datalogging software. The electrode was calibrated as previously reported using $O_2^-$ generated as a product of the catalytic decomposition of xanthine by XOD (Tammeveski *et al*, 1998).

### 6.2.6 Monitoring of TaClo induced $O_2^-$ flux from isolated mitochondria

The protein concentration of the mitochondrial suspension was determined to be 3.45 µgml$^{-1}$. Aliquots of the thawed mitochondrial suspension were diluted 1:5 to 0.69 µgml$^{-1}$ in mitoprep buffer to ensure sufficient samples were available over the course of experimentation. A conical dish was used to present a 100 µl sample of the mitochondrial suspension to the $O_2^-$ electrode. Once a stable baseline current response was established, serial additions of 10 µM TaClo in mitoprep buffer were made to the cell. Any current change following addition was recorded for 1 min before the next addition was made. Dosing continued until a steady-state response was achieved that remained unchanged following further TaClo addition.

### 6.2.7 Comparison of known mETC complex inhibitors to TaClo

Prior to use, 100 µM solutions of rotenone, antimycin A and TaClo were prepared separately in mitoprep buffer. Inhibitors were investigated in sequence, with only one inhibitor being used per mitochondrial sample. Aliquots of the mitochondrial suspension were diluted to 0.69 µgml$^{-1}$ in mitoprep buffer. The electrode setup was the same as used to investigate the TaClo dose response. A 100 µl sample of mitochondrial suspension was introduced to the electrode and the current responses recorded. Once a stable baseline current response was observed, 10 µl of a particular inhibitor was added. The changes in current response were recorded for 3 min following inhibitor addition. Fresh aliquots of mitochondrial suspension were used for each inhibitor challenge with thorough cleaning of the electrodes and conical dish between tests. Three current traces were acquired for each inhibitor.

## 6.3 Results

### 6.3.1 Electrode calibration

The generation of $O_2^-$ by enzymatic conversion of xanthine to uric acid by XOD has previously been used to calibrate the $O_2^-$ response of cytochrome *c* functionalised gold electrodes. In the present study the current density at steady-state was linearly dependent on the concentration of XOD in the presence of excess substrate ($y = 804.3x - 5.4$, $r=0.98686$, $n=3$).

### 6.3.2 Effect of TaClo upon mitochondrial function

After 1 h incubation with resazurin, data from both TaClo-treated and untreated populations demonstrated that the FI at $\lambda_{em}$ 590 nm was linearly dependent upon incubation time (TaClo untreated cells: $y=0.4249x-0.2803$, $r=0.9993$, $n=4$; cells treated with 100 µM TaClo: $y=0.2063x-0.0788$, $r=0.9873$, $n=4$). The rate of FI change was significantly higher in TaClo untreated cells *vs.* treated cells after 3 h incubation, indicating metabolic processes became significantly impeded in treated cells after just 3 h exposure ($p \leq 0.05$).

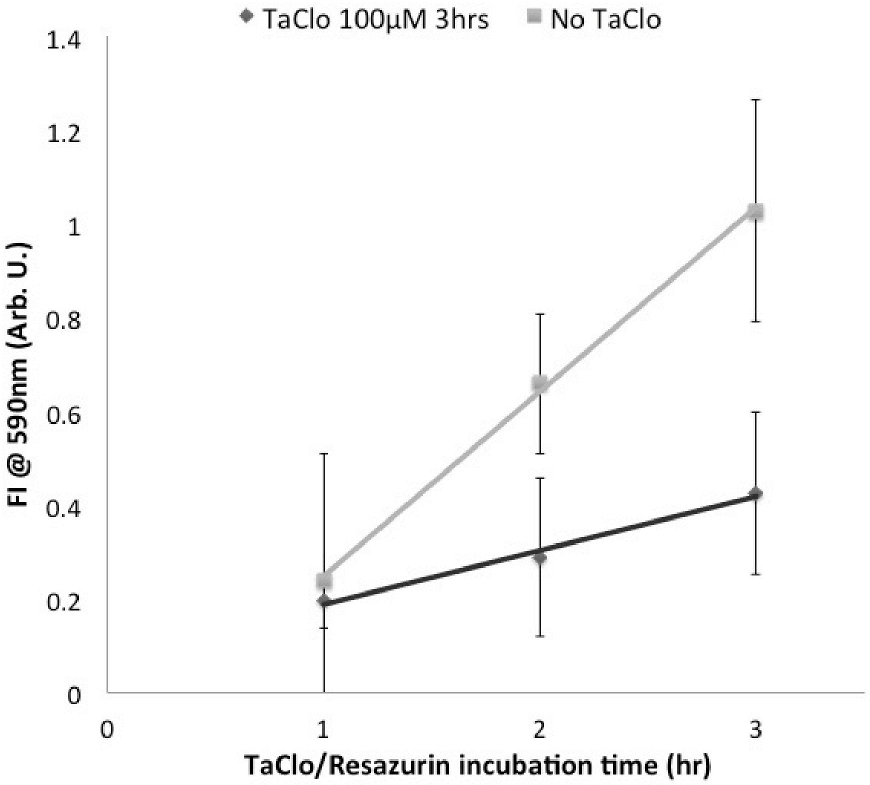

**Figure 6.2:** TaClo mediated changes in resazurin metabolism were monitored in real-time as an assessment of cell viability. Cells exposed to 100µM TaClo exhibited lower FI at 590nm following 2 h incubation compared with control cells suggesting TaClo compromised the metabolic capacity of the cells within this timeframe (The data is presented ± SEM, n=4).

### 6.3.3 Amperometric monitoring of $O_2^-$ generation by TaClo

A dose response curve was generated by recording the current change produced by the cumulative addition of TaClo to isolated mitochondria suspended in sucrose buffer. The change in current was directly related to the flux of $O_2^-$ from the mitochondria, which occurred immediately following TaClo addition. Linear regression analysis of the peak current observed following cumulative TaClo additions within a given sample of isolated mitochondria (nAµM$^{-1}$) described the relationship as directly proportional with the equation $y = 12.384x + 0.6697$ ($r=0.9929$, $n = 4$) where $y$ = current change and $x$ = TaClo concentration.

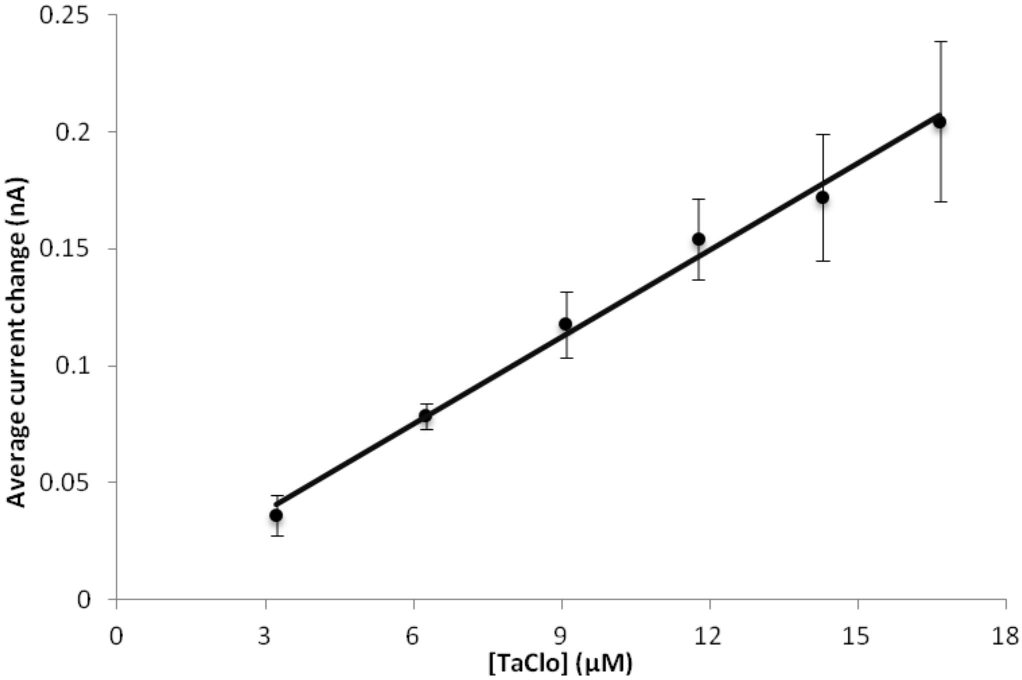

**Figure 6.3:** Peak current responses of isolated SY-5Y mitochondria to cumulative doses of TaClo. (The data is presented ± SEM, n=4).

### 6.3.4 Comparison of $O_2^-$ generation by known mETC inhibitors

All three inhibitors elicited $O_2^-$ flux from isolated mitochondria immediately following exposure, which was monitored directly and in real time using the cytochrome *c* functionalised electrode. Figure 6.4 describes the relative magnitudes of currents generated through the inhibition of the mETC with antimycin A, TaClo and rotenone, whilst Figure 6.5 shows representative traces recorded following treatment with each of the mETC inhibitors. The Complex III inhibitor antimycin A elicited the greatest current change of the three inhibitors studied, on average producing a peak current of

239.85 pA (±24.65 pA, n=4), while the Complex I inhibitors TaClo and rotenone produced peak currents of 122.75 pA (±20.49 pA, n=4) and 118.23 pA (±15.64 pA, n=4) respectively. There was a distinct difference in the size and time-course of $O_2^-$ current generated by the different mETC inhibitors as shown by both igures 6.4 and 6.5. Both of the Complex I inhibitors generated an initial current peak lasting between 10-15 s which then decayed to the baseline current response that was recorded pre-stimulation. This did not occur for the Complex III inhibitor which induced rapid current increases that repeatedly reached a plateau at a sustained mean value of +165 pA above the baseline response (±56 pA, n=4).

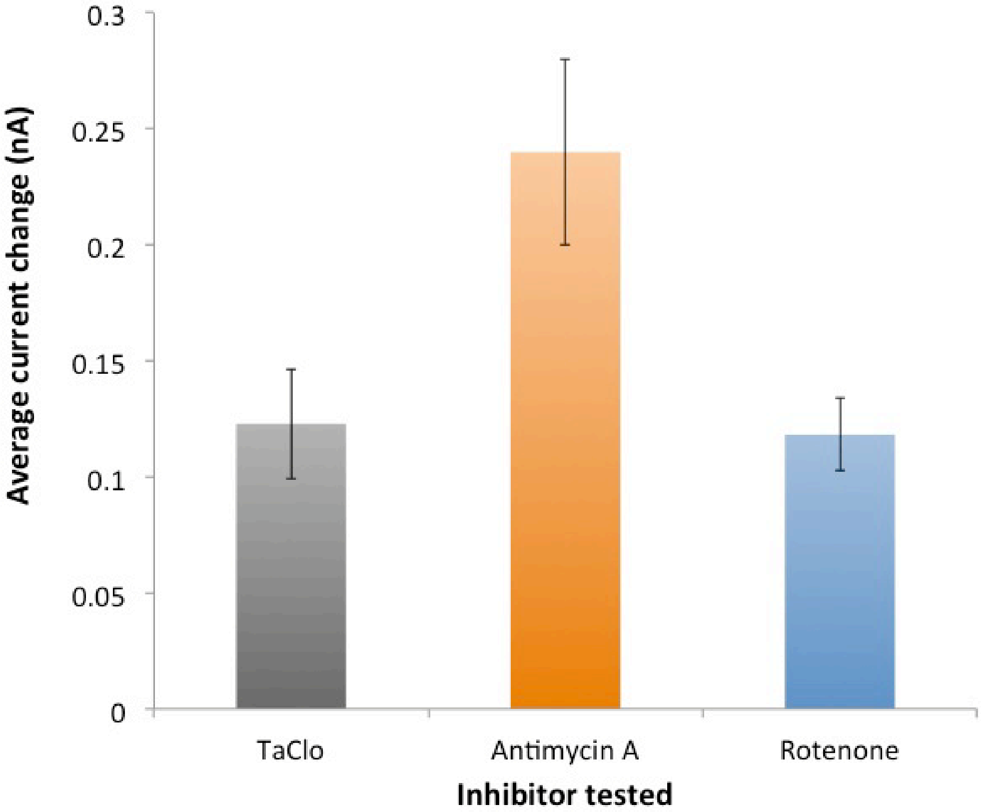

**Figure 6.4:** Comparison of current responses generated by the addition of 100µM mETC inhibitors TaClo, rotenone and antimycin A (final concentration 3.2µM) to isolated mitochondria from SY5Y-SH cells (The data is presented ± SEM , n=4).

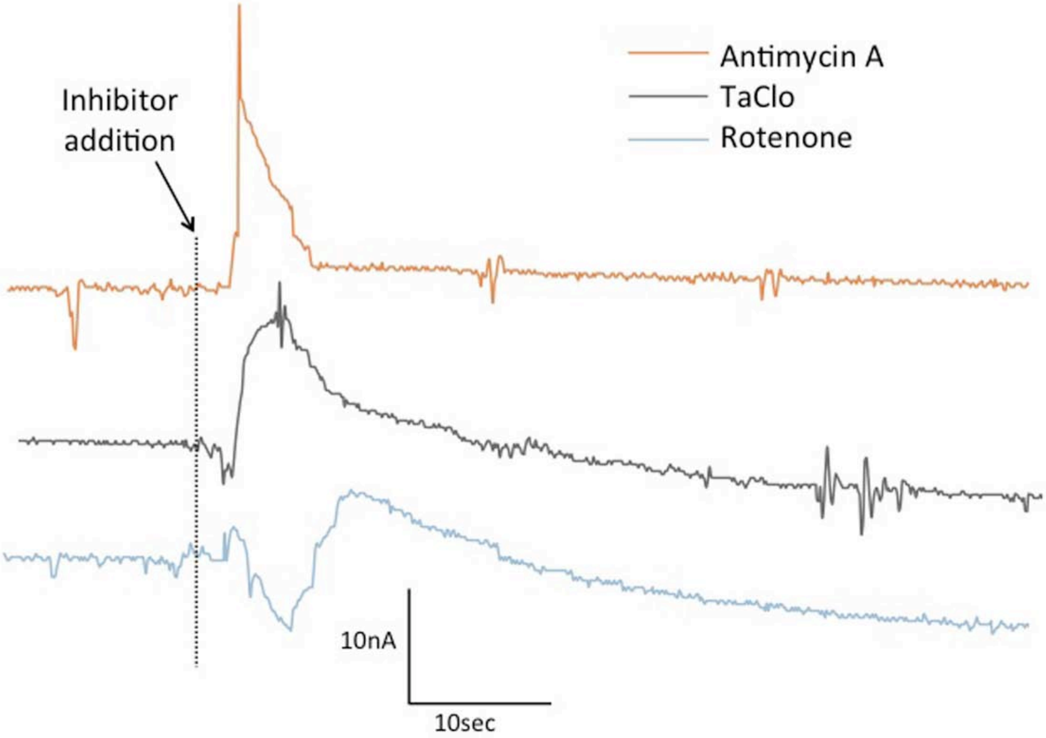

**Figure 6.4:** Comparison of respective traces elicited from the addition of 100µM mETC inhibitor to isolated mitochondria from SY5Y-SH cells. The traces shown are representive of a single inhibitor challenge with a single sample of isolated mitochondria.

## 6.4 Discussion

TaClo is an endogenously generated metabolite of the hypnotic agent chloral hydrate. It has been described as a neurotoxin and has been reported as a causative factor in the degeneration of the *substantia nigra pars compacta*, which is a defining feature of Parkinson's disease (German *et al*, 1989; Langston and Ballard, 1983; Liu *et al*, 2010, Fearnley *et al*, 1991). It has been proposed that the mechanism of TaClo induced neurotoxicity involves increased ROS flux from the mitochondria over the course of TaClo accumulation (Liu *et al*, 2010). All previous studies that have tried to assess the link between TaClo induced cell toxicity and ROS production have exposed cells to TaClo for at least 72 h before assessing cellular damage. It was, therefore, the primary aim of this study to show whether the Complex I inhibitor TaClo was capable of eliciting acute cytotoxic effects in SH-SY5Y neuroblastoma cells, and to show with temporal resolution the real-time flux of $O_2^-$ from isolated SH-SY5Y mitochondria after TaClo exposure. The work presented in this paper has clearly shown, for the first time, that the generation of $O_2^-$ is an immediate consequence of mitochondrial complex inhibition by TaClo. This gives new insight into the timescale over which TaClo-dependent cell damage may occur.

Initially, preliminary investigations to support this work were concerned with ascertaining whether the $O_2^-$ flux could be monitored from whole cells following TaClo exposure. Following many attempts, it was found that no $O_2^-$ flux could be observed from intact cells. When considering its presence in mammalian systems, TaClo is a β-carboline compound produced through the intracellular reaction of trichloroacetaldehyde and tryptamine. As such, cells would theoretically not be exposed exogenously to TaClo, more the product would accumulate within the trichloroacetaldehyde exposed cells over time. In light of this, acute phase stuies such the present implementing a whole cell treatment regimen to investigate ROS production from the mitochondria may well not be fully physiologically relevant. It was suggested that a more direct approach to investigating mitochondrial ROS production following TaClo exposure would be more relevant and useful through the implementation of the isolated mitochondria protocol discussed in Chapter 5 and recently published (Henderson et al. 2009).

Dispite these caveats, data from continuous whole cell respiratory assessment using a resazurin-based viability assay demonstrated that TaClo was capable of significantly impeding cell respiration within 2 h of incubation. When the isolated mitochondria from SY5Y-SH cells were investigated using an $O_2^-$ selective functionalised gold electrode, it was found that rapid flux of $O_2^-$ from the mitochondria was measurable in real-time immediately following exposure to the inhibitor. The amperometric technique demonstrated that $O_2^-$ flux following TaClo treatment was comparable with that of two other known mETC inhibitors antimycin A and rotenone. The dynamics of the different responses demonstrated that TaClo exerted an effect on Complex I of the mETC and provided evidence that the toxic effects of the compound are mediated through the generation of ROS.

TaClo has been shown to cause considerable and significant cell death in many neuronal studies (Janetzky *et al*, 1999; Kochen *et al*, 2003; Storch *et al*, 2006; Bringmann *et al*, 2000) The study by Bringmann *et al* (Bringmann *et al*, 2000) in particular suggested that despite TaClo being taken up into neuronal cells within 15 min of incubation, no measurable effect on cell viability could be observed. This may have been due to the Trypan blue dye exclusion assay that the authors used to assess viability. Trypan blue assays rely upon the loss of cell membrane integrity as a measure of damage, whereas resazurin assessment is a measure of the reductive capability of the intracellular environment (Gonzalez *et al*, 2001). Resazurin has been established as a tool for the assessment of cell cytotoxicity (O'Brien *et al*, 2000, Fields *et al*, 1993). The reduction of resazurin to fluorescent resorufin by metabolic activity, generally mitochondrial reduction reactions, allowed the comparative assessment of changes in metabolic function between populations of live cells. Unlike MTT assays, the resorufin product of resazurin metabolism is soluble, removing the need to lyse the cells and solubilise the product in order to read the assay outcome. This facilitated the measurement of cumulative resorufin product generation, therefore allowing the continuous assessment of any acute metabolic effects in response to TaClo exposure. The resazurin viability method is known to have inherent weaknesses which mainly relate to the non-specific reduction of the reagent in the cytosol, however compared with rate to reduction reactions carried out at the mitochondria, the non-specific cytosolic effects are thought to be negligible (O'Brien *et al*, 2000). The ability to continuously measure viability which was facilitated by the technique made it the most appropriate tool for monitoring the acute effects of the neurotoxin in these studies. The timescale over which TaClo was shown to exhibit significant effects upon the cells was a novel observation. With resazurin, respiratory depression was observed within 2 h whereas many other studies incubate with TaClo for up to 72 h before viability assessment begins. Due to the length of time needed to employ more traditional cell viability techniques such as Trypan blue, and coupled with the rapid onset of ROS generation and highly developed antioxidant processes, the acute effects of many mitochondrial inhibitors have not yet been fully investigated. The real-time and direct nature of monitoring $O_2^-$ generation from the isolated mitochondria with an electrode circumvented the time and selectivity complications surrounding other modes of ROS quantification such as the use of fluorescent dyes dihydroethidium bromide (DHE) or dihydrodichlorofluorescein diactetate (DCF-DA).

The observation that antimycin generated the largest flux of $O_2^-$ of the three inhibitors investigated was in keeping with current literature regarding complex-specific $O_2^-$ generation (Henderson *et al*, 2009, Brand *et al*, 2004). Inhibition of Complex III is known to cause asymmetric generation of $O_2^-$ both into the inter-membrane space where it can freely diffuse and interact with the electrode, and into the mitochondrial matrix where the charged molecule is trapped due to the relative impermeability of the inner mitochondrial membrane (St-Pierre *et al*, 2002). The $O_2^-$ flux observed from isolated mitochondria following treatment with rotenone may be caused by an interaction between TaClo and the NADH-ubiquinone oxidoreductase of Complex I. Normal transfer between the iron-sulphur cluster N2 and ubiquinone of Complex I is reported to be the site of unavoidable electron leakage from the mETC, causing local high $O_2^-$ flux (Lambert and Brand, 2004). TaClo is thought to inhibit electron transfer from Complex I to ubiquinone through interaction with the quinone binding site on the Complex I oxidoreductase (Majander *et al*, 1994). The inherent lipophilicity of TaClo would permit the molecules access to this membrane embedded site of the protein, (Bringmann *et al*, 1996) much like DPI (Majander *et al*, 1994). The similarity between the modes of superoxide flux of TaClo and rotenone suggested that the compounds elicited effects by similar means, corroborating recent literature regarding TaClo-induced inhibition (Bringmann *et al*, 2000). Both inhibitors resulted in the current response decaying towards the baseline level following an initial increase, as displayed in Figure 6.5. This may have been due to the point at which the mETC inhibition occurred. It is known that mitochondria generate a basal level of $O_2^-$ as a consequence of the high turnover of electrons by the mETC. The baseline current at which amperometric monitoring started is representative of this basal $O_2^-$ production. When the mETC was blocked at Complex I, the downstream flow of electrons was decreased, resulting in the turnover of electrons at Complex III being much lower (despite electrons still transferring between Complexes II and III). After initial high efflux of electrons from the mETC and subsequent bolus of generated $O_2^-$, the basal level of mitochondrial metabolism was decreased. Furthermore, $O_2^-$ generated by Complex I is released to the matrix side of the inner membrane (St-Pierre *et al*, 2002, Lambert and Brand, 2004) and, coupled with the reduced electron flow through the mETC, the outcome observed was a decrease in the $O_2^-$ available for detection.

In conclusion, this study provided evidence that TaClo is capable of eliciting changes in cell metabolism in less than 2 h and that the inhibition of mETC by TaClo results in instant and reproducible flux of $O_2^-$ from isolated mitochondria. The rapid action with which TaClo affects the mitochondria is in line with other mitochondrial inhibitors such as rotenone and antimycin A, and further supports the involvement of early stage ROS signalling in the pathology of β-carboline precursor compounds. The large TaClo induced $O_2^-$ flux observed from isolated mitochondria, coupled with new insight demonstrated in this study regarding the short timescale over which TaClo can exert respiratory effects in whole cells, further implicate ROS as an important factor in TaCo induced cytotoxicity. A recent study suggested that at low doses TaClo had a stimulatory effect on tyrosine hydroxylase, the rate limiting enzyme in neuronal catecholamine production (Riederer *et al*, 2002). The oxidation of excess catecholamines and the resultant increased production of intracellular ROS have been perhaps most prominently defined in the field of cardiac research (Costa *et al*, 2009; Mladenka *et al*, 2009; Costa *et al*, 2009). If at low doses TaClo acts as a mETC inhibitor whilst simultaneously boosting catecholamine (DA) production, it is possible that cytotoxic effects are exerted though an increase in oxidative stress from both increased dopamine oxidation and mitochondrial inhibition and, in the long term, promoting neuronal dysfunction as a consequence of destabilised cell metabolism. It has also been reported that ROS have profound effects upon striatal neuronal ability to release and take up dopamine (Bao *et al*, 2005; Milusheva *et al*, 2005). This has been demonstrated by monitoring dopamine release following the inhibition of the mETC using rotenone (Milusheva *et al*, 2005).

There are many plausible routes by which TaClo has been reported to exert cytotoxic effects, many attributed to the increased generation of ROS (Bringmann *et al*, 1995; Kochen *et al*, 2003; Akundi *et al*, 2004; Bringmann *et al*, 2000, Gerlach *et al*, 1998) which are known to be short-lived and highly reactive under certain conditions (Halliwell and Gutteridge, 2007). Recent studies have regarded an increase in ROS generation as secondary to 5-hydroxytryptamine (5HT) or DA release (Gerlach *et al*, 1998, Foley *et al*, 2000). The evidence presented by this study suggests that the uncontrolled production on $O_2^-$ by the mitochondria may be more central to the TaClo-induced pathogenesis of progressive neurodegenerative disorders than previously reported. In order to fully understand the roles of such molecules within the complex architecture of aerobic metabolism, real-time evidence is required that focuses directly upon individual species at the time-point of generation such that inferred effects may be substantiated.

## 6.5 References

Akundi R.S., Macho A., Muñoz E., Lieb K., Bringmann G., Clement H.W., Hüll M., Fiebich B.L., 2004 1-Trichloromethyl-1,2,3,4-tetrahydro-beta-carboline-induced apoptosis in the human neuroblastoma cell line SK-N-SH. Journal of Neurochemistry 91, 263-273.

Bao L., Avshalumov M.V., Rice M.E., 2005. Partial mitochondrial inhibition causes striatal dopamine release suppression and medium spiny neuron depolarization via $H_2O_2$ elevation, not ATP depletion. Journal of Neuroscience 25, 10029-10040.

Brand M.D., Affourtit C., Esteves T.C., Green K., Lambert A.J., Miwa S., Parkey J.L., Parker N., 2004. Mitochondrial superoxide: production, biological effects, and activation of uncoupling proteins. Free Radical Biology & Medicine 37, 755-767.

Bringmann G., Bruckner R., Mossner R., Feineis D., Heils A., Lesch K.P., 2005. Effect of 1-trichloromethyl-1,2,3,4-tetrahydro-beta-carboline (TaClo) on human serotonergic cells. Neurochemical Research 25, 837-843.

Bringmann G., Feineis D., God R., Fähr S., Wesemann W., Clement H.W., Grote C., Kolasiewicz W., Sontag K.-H., Heim C., Sontag T.A., Reichmann H., Janetzky B., Rausch W.-D., Abdel-Mohsen M., Koutsilieri E., Götz M.E., Gsell W., Zielke B., Riederer P., 1996. Neurotoxic effects on the dopaminergic system induced by TaClo (1-trichloromethyl-1,2,3,4-tetrahydro-β-carboline), a potential mammalian alkaloid: *in vivo* and *in vitro* studies. Biogenic Amines 12(2),83-102.

Bringmann G., God R., Feineis D., Janetzky B., Reichmann H., 1995. TaClo as a neurotoxic lead: improved synthesis, stereochemical analysis, and inhibition of the mitochondrial respiratory chain. Journal of Neural Transmission-Supplumentum. 46, 245-254.

Chang S.-C., Pereira-Rodrigues N., Henderson J.R., Cole A., Bedioui F., McNeil C.J., 2005. An electrochemical sensor array system for the direct, simultaneous *in vitro* monitoring of nitric oxide and superoxide production by cultured cells. Biosensors & Bioelectronics 21, 917-922.

Cleeter M.W.J., Cooper J.M., Schapira A.H.V., 1992. Irreversible inhibition of mitochondrial Complex I by 1-methyl-4-phenylpyridinium: evidence for free radical involvement. Journal of Neurochemistry. 58, 786-789.

Costa V.M., Carvalho F., Bastos M.L., Carvalho R.A., Carvalho M., Remiao F., 2011. Contribution of catecholamine reactive intermediates and oxidative stress to the pathologic features of heart diseases. Current Medical Chemistry. 18(15),2272-2314.

Costa V.M., Silva R., Tavares L.C., Vitorino R., Amado F., Carvalho F., Bastos Mde L, Carvalho M., Carvalho R.A., Remião F., 2009. Adrenaline and reactive oxygen species elicit proteome and energetic metabolism modifications in freshly isolated rat cardiomyocytes. Toxicology 260(1-3),84-96.

Fearnley J.M., Lees A.J., 1991. Ageing and Parkinson’s disease: *subtantia nigra* regional selectivity. Brain. 114(5),2283-2301.

Fields R.D., Lancaster M.V., 1993. Dual-attribute continuous monitoring of cell proliferation/cytotoxicity. American Biotechnology Laboratory 11(4),48-50.

Foley P., Riederer P., 2000. Influence of neurotoxins and oxidative stress on the onset and progression of Parkinson's disease. Journal of Neurology 247(Suppl 2),ii82-94.

Gerlach M., Xiao A.Y., Heim C., Lan J., God R., Feineis D., Bringmann G., Riederer P., Sontag K.-H., 1998. 1-Trichloromethyl-1,2,3,4-tetrahydro-beta-carboline increases extracellular serotonin and stimulates hydroxyl radical production in rats. Neuroscience Letters. 1257,17-20.

German D.C., Manaye K., Smith W.K., Woodward D.J., Saper C.B., 1989. Midbrain dopaminergic cell loss in Parkinson's disease: computer visualization. Annals of Neurology 26,507-514.

Gonzalez R.J., Tarloff J.B., 2001. Evaluation of hepatic subcellular fractions for Alamar blue and MTT reductase activity. Toxicology *in vitro* 15,257-259.

Halliwell B., Gutteridge, J.M.C., 2007. Free Radicals in Biology and Medicine. 4th ed. Oxford: Oxford University Press.

Hartley A., Stone J.M., Heron C., Cooper J.M., Schapira A.H.V., 1994. Complex I inhibitors induce dose-dependent apoptosis in PC12 cells: relevance to Parkinson's disease. Journal of Neurochemistry 63,1987-1990.

Henderson J.R., Swalwell H., Boulton S.J., Manning P., Birch-Machin M.A., McNeil C.J., 2009. Direct, real-time monitoring of superoxide generation in isolated mitochondria. Free Radical Research 43,1-7.

Janetzky B., Gille G., Abdel-mohsen M., God R., Rausch W.-D., Bringmann G., Reichmann H., 1999. Effect of highly halogenated β-carbolines on dopaminergic cells in culture and on mitochondrial respiration. Drug Development Research 46(1),51-56.

Javitch J.A., D'Amato R.J., Strittmatter S.M., Snyder S.H., 1985. Parkinsonism-inducing neurotoxin, N-methyl-4-phenyl-1,2,3,6-tetrahydropyridine: uptake of the metabolite N-methyl-4-phenylpyridine by dopamine neurons explains selective toxicity. Proceedings of the National Academy of Science U S A 82,2173-2177.

Kochen W., Kohlmuller D., De Biasi P., Ramsay R., 2003. The endogeneous formation of highly chlorinated tetrahydro-beta-carbolines as a possible causative mechanism in idiopathic Parkinson's disease. Advances in Experimental Medical Biology 527,253-263.

Lambert A.J., Brand M.D., 2004. Inhibitors of the quinone-binding site allow rapid superoxide production from mitochondrial NADH:ubiquinone oxidoreductase (Complex I). Journal of Biological Chemistry 297,39414-39420.

Langston J.W., Ballard P., Tetrud J.W., Irwin I., 1983. Chronic Parkinsonism in humans due to a product of meperidine-analog synthesis. Science 219,979-980.

Langston J.W., Ballard P., 1984 Parkinsonism induced by 1-methyl-4-phenyl-1,2,3,6-tetrahydropyridine (MPTP): implications for treatment and the pathogenesis of Parkinson's disease. Canadian Journal of Neurological Science 11(Suppl 1),160-165.

Liu M., Choi D.-Y., Hunter R.L., Pandya J.D., Cass W.A., Sullivan P.G., Kim H.C., Gash D.M., Bing G., 2010. Trichloroethylene induces dopaminergic neurodegeneration in Fisher 344 rats. Journal of Neurochemistry 112(3),773-783.

Majander A., Finel M., Wikström M., 1994. Diphenyleneiodonium inhibits reduction of iron-sulfur clusters in the mitochondrial NADH-ubiquinone oxidoreductase (Complex I). Journal of Biological Chemistry 269, 21037-21042.

Manning P., Cookson M.R., McNeil C.J., Figlewicz D., Shaw P.J., 2001. Superoxide-induced nitric oxide release from cultured glial cells. Brain Research 911(2),203-210.

Manning P., McNeil C.J., Cooper J.M., Hillhouse E.W., 1998. Direct, real-time sensing of free radical production by activated human glioblastoma cells. Free Radical Biology & Medicine. 24,1304-1309.

Milusheva E., Baranyi M., Kittel Á., Sperlágh B., Vizi E.S., 2005. Increased sensitivity of striatal dopamine release to $H_2O_2$ upon chronic rotenone treatment. Free Radical Biology & Medicine 39(1),133-142.

Mladenka P., Hrdina R., Bobrovová Z., Semecky V.R., Vávrová J., Holeková M., Palicka V., Mazurová Y., Nachtigal P., 2009. Cardiac biomarkers in a model of acute catecholamine cardiotoxicity. Human Experimental Toxicology 28,631-640.

O'Brien J., Wilson I., Orton T., Pognan F., 2000. Investigation of the Alamar Blue (resazurin) fluorescent dye for the assessment of mammalian cell cytotoxicity. European Journal of Biochemistry 267,5421-5426.

Riederer F., Luborzewski A., God R., Bringmann G., Scholz J., Feineis D., Moser A., 2002. Modification of tyrosine hydroxylase activity by chloral derived β-carbolines *in vitro*. Journal of Neurochemistry. 81(4),814-819.

St-Pierre J., Buckingham J.A., Roebuck S.J., Brand M.D., 2002. Topology of superoxide production from different sites in the mitochondrial electron transport chain. Journal of Biological Chemistry 277,44784-44790.

Storch A., Hwang Y.I., Bringmann G., Feineis D., Ott S., Brückner R., Schwarz J., 2006. Cytotoxicity of chloral-derived β-carbolines is not specific towards neuronal nor dopaminergic cells. Journal of Neural Transmission 113(12),1895-1901.

Swerdlow R.H., Parks J.K., Miller S.W., Tuttle J.B., Trimmer P.A., Sheehan J.P., Bennett J.P., Davis R.E., Parker W.D. 1996. Origin and functional consequences of the Complex I defect in Parkinson's disease. Annals of Neurology 40(4),663-671.

Tammeveski K., Tenno T.T., Mashirin A.A., Hillhouse E.W., Manning P., McNeil C.J., Superoxide electrode based on covalently immobilised cytochrome *c*: modelling studies. Free Radical Biology & Medicine 25,973-978.

# Chapter 7. Integration of optical and amperometric monitoring systems

## 7.1 Introduction

Reactive oxygen species are known to play any important roles in cell communication, proliferation and death however the mechanisms of these effects have not been fully elucidated. Although the development of many pathologies such as Parkinson's disease (PD) (Di Matteo *et al*. 2009), rheumatoid arthritis (Kundu *et al*. 2011) and amyotrophic lateral sclerosis (ALS) (Panov *et al*. 2011) has been linked to uncontrolled or modified ROS generation and scavenging, these assertions are founded mainly on the inferred effects of increased ROS production like an increase in DNA stand breaks or intracellular reduced glutathione concentration. The use of free ROS-sensitive dyes to monitor intracellular changes in ROS production and metabolism gives only part of the story, owing to the inherent toxicity of such dyes and also to reporting inconsistencies due to uneven loading and light sensitivities (Boulton *et al*. 2011; Chen *et al*. 2010). The extent of such issues surrounding the ROS responsive dyes DHR123 and DCF-DA was investigated at great length in Chapter 2. As discussed in Chapter 3, encapsulating dyes in a bioinert polyacrylamide matrix not only prevents loaded cells from any cytotoxic consequences of dye exposure, but conversely prevents the dye from interacting with any intracellular interfering macromolecules capable of diminishing or exaggerating appropriate dye responses (Clark *et al*. 1999). The nanosensors employed in this study comprised ROS responsive DHR123 co-localised within the nanosensor matrix with a stable reference dye AlexaFluor568. This allowed ratiometric measurements to be made regarding the nanosensors, thus eliminating the erroneous effects of photo-bleaching and uneven loading.

Coupling intracellular nanosensor measurement technology to the extracellular amperometric monitoring system provided a platform by which both cellular compartments can be assessed in terms of ROS flux in a direct and simultaneous manner. The impact of ROS communication between cells population is of great interest to many disease states where modified communication is involved in disease progression, for example in HIV infection (Olivetta *et al*. 2009). A conceptual device was conceived that provided the unique opportunity to monitor ROS generation of the internal environment and well as the $O_2^-$ flux from the same cells. Eventually this could also encompass observations of how other populations of cells respond to that extracellular $O_2^-$ flux. A diagram representing the integrated platform concept is shown in Figure 6.1.

Two iterations of the electrode array platform were designed and characterised over the course of this study, referred to as 1st and 2nd generation arrays (G1 and G2 arrays respectively). Feasibility studies regarding the independent amperometric and optical properties of the arrays were undertaken prior to integrating the two techniques. The G2 arrays were fully integrated with the optical systems allowing for the first time measurement of the intracellular environment using ratiometric ROS-responsive nanosensors alongside direct extracellular monitoring of $O_2^-$ flux from the same cells. Due to the time constraints of the project, this study represents the first preliminary investigation of a fully integrated opto-electrical device. The initial data regarding simultaneous intra- and extracellular measurements demonstrated ample proof of concept and highlighted optimisation opportunities for a 3rd generation device.

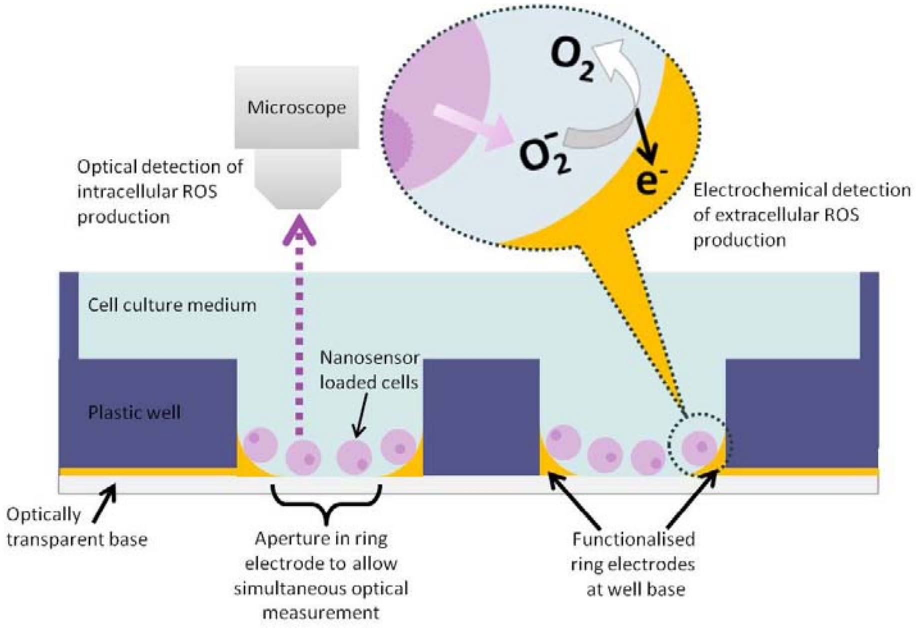

**Figure 7.1:** A diagrammatic representation of the integrated platform concept. Nanosensor loaded cells were placed into the wells of the array. The well contained a gold ring electrode that was functionalised to permit selective sensing of $O_2^-$ flux amperometrically. A fluorescence microscope was used to monitor the cells optically from above whilst the cytochrome *c* functionalised electrode monitored $O_2^-$ flux extracellularly.

## 7.2 Materials and Methods

### 7.2.1 Design of the electrode array

In consultation with the manufacturers (MiniFAB, Australia) a device was designed and fabricated to satisfy the microscope compatibility and functional criteria of the proposed system. All devices comprised two components, one gold-coated base section patterned with ring electrodes and tracking and one upper rigid section that was milled to form the well architecture. The base slide was fabricated from a 250µm thick flexible polyester that was gold-sputtered and laser-etched to define the ring electrodes and associated tracking. The upper rigid section of the cartridge was formed from two 1.5mm thick slides which were milled and sandwiched together to create the upper and lower well walls when associated with the thin electrode-containing base slide. The two sections were assembled in an alignment jig and fixed together using a thin layer of pressure sensitive adhesive (PSA). The first iteration G1 arrays were presented as ready-to-use, fully assembled cartridges with the electrode containing and well forming slides assembled into a single unit. Steel wires were attached to the contact pads of the electrodes using silver doped epoxy resin to facilitate coupling to the potentiostat. The arrays were cleaned, checked, and checked for functionality using the procedures outlined below.

Due to electrode delamination and the low signal to noise ratios observed during G1 array testing, second iteration G2 electrodes were designed and fabricated in consultation with the manufacturers. The G2 arrays were designed to be more practical and robust, each array being supplied as two separate units along with an alignment jig to be assembled as required. The conformation of the two different arrays is shown in Figure 7.2. Following definition of the electrodes on the gold spluttered slide the entire surface was rinsed of debris, dried under nitrogen and coated with a protective layer of photoresist. To assemble the components of the G2 array in preparation for functionalisation the electrode-containing slide was sonicated for 30 s in acetone, followed by rinsing with isopropanol then water to remove the protective photoresist layer. The slide was immediately dried under nitrogen and located gold side up within the assembly jig using guide pins. The backing was removed from an upper rigid section to reveal the PSA and affixed to the electrode slide, again using the guide pins to align the ring electrode apertures with the centre of the wells.

Once assembled the array was removed from the jig and checked for alignment and proper sealing of the wells. The G2 electrodes were assessed for surface cleanliness prior to functionalization and calibrated using the methods described below prior to commencing cell based investigations.

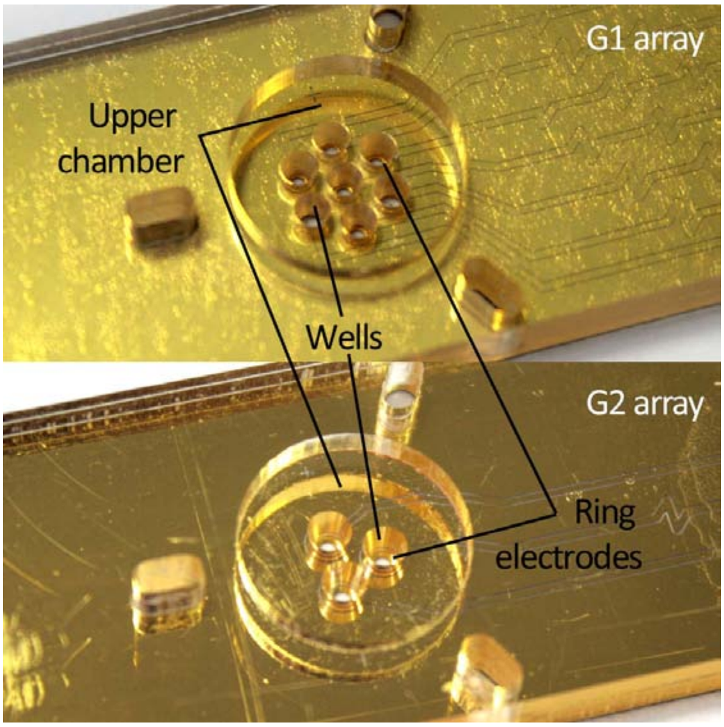

**Figure 7.2:** The assembled G1 and G2 electrode array as received from MiniFAB. Each electrode can be seen at the base of each well of the array, with the associate tracking protected beneath the rigid polycarbonate upper section. The upper and lower well walls allow the array to be flooded to facilitate the movement of solutes between wells.

***CV analysis:*** CV was used to assess the surface cleanliness of the gold electrodes in all arrays. An AutoLab PGSTAT potentiostat was used to perform all CV. A solution of 1mM potassium ferricyanide ($Fe^{iii}(CN)_6{}^{3+/2+}$) redox couple dissolved in 100mM phosphate buffer (pH 7.4) was used as the probe solution. A capillary Ag/AgCl electrode and steel wire were used as reference and counter electrodes respectively. The entire array was flooded in probe solution prior to cycling and was not agitated during measurement. Each ring electrode was interrogated individually with 10 cycles of potential sweeping from -0.3 to +0.6V with a scan rate of $100mVs^{-1}$. Scans were averaged to produce the final trace. The G2 array electrodes were interrogated using the same method, however 1mM ferrocenedimethanol dissolved in 100mM phosphate buffer (pH7.4) was used as the probe solution with sweeps ranging from -1V to +0.4V.

***Electrolytic cleaning protocol:*** An AutoLab PGSTAT potentiostat was used to perform all electrolytic cleaning procedures. A capillary Ag/AgCl electrode and steel wire were used as reference and counter electrodes respectively. The entire array was flooded with 100mM phosphate buffer (pH 7.4) prior to cleaning. Each electrode was held at a potential of 1.4V *vs.* Ag/AgCl reference for 2 min. After all electrodes had been treated, the whole array was rinsed with deionised water.

***UV- ozone cleaning protocol:*** A Novascan PSD Pro Series UV Ozone photoreactor was used for all UV ozone cleaning cycles. The array was rinsed with deionised water, dried under nitrogen and placed in the photoreactor chamber. Once sealed, the chamber was purged with $O_2$ for 1 min followed by a 5 min UV exposure. The array remained within the chamber for 30 min post-exposure before being removed, rinsed with deionised water and dried once more under nitrogen. Arrays were functionalised or otherwise processed as soon as possible following cleaning.

### 7.2.2 $O_2^-$ sensitive electrode preparation

The gold surface of each individual electrode within an array was functionalised using the same technique previously reported (Manning *et al*. 1998) and as discussed in Chapters 5 and 6. Briefly, 10µl 50mM DTSSP solution in water was added to the wells and incubated for 5 min at room temperature before being gently rinsed with distilled water. Any remaining liquid was flicked from the array before filling the electrode containing well with 2mM cytochrome *c* solution (in PBS, pH 7.4). The whole array was wrapped in Parafilm to prevent evaporation. Steel wires were affixed to the electrode contacts using silver doped epoxy resin to facilitate potentiostat coupling, then the array was incubated at 4°C. Parafilm was removed and the modified electrodes were rinsed thoroughly with deionised water immediately before use.

### 7.2.3 Electrode calibration

Functionality of all G2 arrays was first confirmed using the $O_2^-$ generated as a product of the catalytic decomposition of xanthine by XOD described previously (Cooper *et al*. 1993; Manning *et al*. 1998). Each electrode was interrogated individually using an AutoLab PGSTAT potentiostat coupled to a PC running associated control software. For all amperometric measurements the functionalised gold working electrode was coupled with a Ag/AgCl capillary reference electrode (Harvard Apparatus, Edenbridge, UK) and steel counter electrode. All measurements were carried out at an operating potential of +100mV (vs Ag/AgCl). For calibration, the entire array was flooded with 10mM xanthine solution (in 100mM KOH) and datalogging was commenced. Once a stable baseline current was observed, various concentrations of XOD were added to the selected well and any change in current was recorded as a function of time. For G1 array electrodes, 0.5 µl XOD was added, in G2 challenges, 1 µl was added to compensate for the different sized wells.

### 7.2.4 Cell culture and preparation

Rat alveolar macrophage cell line NR8383 was routinely cultured in Ham's F12 (Kaighn's modification) medium supplemented with 10% FCS and 1% NEAA. The cells were grown in a 5% $CO_2$ humidified atmosphere and were passaged no more than 4 times over the course of experimentation. Once the cells reached 70% confluence they were seeded into T25 culture flasks and allowed to settle overnight. The following day 10 $mgml^{-1}$ ROS sensitive nanosensors were introduced to the cells and mixed thoroughly with the culture medium. The nanosensors were fabricated as described in Chapter 3 (section 3.2.2) comprising ROS sensitive DHR123 and reference AlexaFluor568 dyes entrapped within a nanoscale polyacrylamide matrix. Cell mediated delivery of the nanosensors was allowed to continue overnight. The following day, cells were harvested and washed once in pre-warmed PBS to remove extracellular nanosensor debris. Re-suspension of the cell pellet in 100 µl pre-warmed culture medium yielded a suspension of ~50,000 $cells.ml^{-1}$. This cell suspension was stored in the routine culture environment until required (no longer then 3 hrs).

### 7.2.5 Functional assessment of the G2 array electrodes

Prior to full integration the optical and amperometric functional properties of the arrays were tested independently using ROS generated by PMA-stimulated macrophages. This was carried out to ensure that physiological levels of ROS could be measured both intra- and extracellularly from within the array and also to check for any interference between the two methods.

Amperometric analysis of nanosensor loaded cells was executed without optical measurement by loading 10 µl cell suspension described in section 7.2.4 into a previously functionalised array well then carefully flooding the upper chamber of the array with pre-warmed culture medium. All amperometric data was logged using an AutoLab PGSTAT potentiostat coupled to a PC running associated control software. The well selected for measurement was coupled to the potentiostat and poised to +100mV *vs.* Ag/AgCl in conjunction with a stainless steel counter electrode. Once a stable baseline current response was achieved, 1 µl PMA at 1, 5 or 10 µgml$^{-1}$ was added to the cells. Any current change was recorded for at least 300 s. Following completion of the run the whole array was rinsed with deionised water and reset as above for the next experiment.

Optical analysis of the array was carried out independently of amperometric monitoring by loading 10 µl of the same nanosensor-loaded cell suspension into a previously functionalised array well. The rest of the array chamber was then flooded with pre-warmed culture medium. Images were acquired using a Nikon Eclipse 80*i* Epi-Fluorescence microscope in conjunction with Nikon BR image acquisition and analysis software. The array was placed onto the microscope stage and secured in place. A bright-field image of the cell-containing well was acquired prior to commencing any measurements to record spatial distribution of cells. Two images of the cells were then collected, one using a B 2E/C filter (representative of DHR123 FI) and the other using a CY3 filter (representative of Alexafluor568 FI). 1 µl PMA was added to the cells (final concentration 1µgml$^{-1}$) and was allowed to incubate for 10 min, after which another set of images were collected using the same settings. The initial bright-field reference image was used to record the position of cell populations upon the electrodes surface. Data regarding the mean FI of the recorded cell regions was identified from the images acquired during the course of experimentation.

### 7.2.6 Simultaneous measurement of extra- and intracellular ROS flux

Nanosensor-loaded NR8383 macrophage cells as described in section 7.2.4 were loaded into the electrode containing wells of a functionalised G2 array. The functionalised array was used in conjunction with a capillary Ag/AgCl reference electrode and steel wire counter electrode, both of which were secured to the array cartridge to avoid electrode misplacement. The array rig was placed under the fluorescence microscope objective and secured in place. Figure 7.3 demonstrates the experiment setup used during simultaneous measurements. The same microscope, settings and filters as described in section 7.2.5 for the feasibility studies were employed for the simultaneous measurements. Prior to acquiring data, the microscope was focussed upon a ring electrode at the base of a cell containing well using the bright-field setting. A reference image was acquired to identify the position of cell populations. An in-house built potentiostat was used to poise the working electrode at +100mV *vs.* the Ag/AgCl reference and current changes were logged using a PicoLog ADC100 converter with associated software. Amperometric data was recorded continuously for the entire experiment. Once a stable baseline current response was achieved, two images of the nanosensor-loaded cells were acquired in quick succession as was executed previously. 1 µl either 1 µgml$^{-1}$ or 5 µgml$^{-1}$ PMA in PBS was then introduced to the interrogated well. As soon as possible after PMA addition, two more images were acquired is the same manner. Image acquisition was repeated periodically for 500 s, after which amperometric datalogging was also terminated. The initial bright-field reference image was used to record the position of cell populations upon the electrodes surface. Data regarding the mean FI of the recorded cell regions was identified from the images acquired during the course of experimentation.

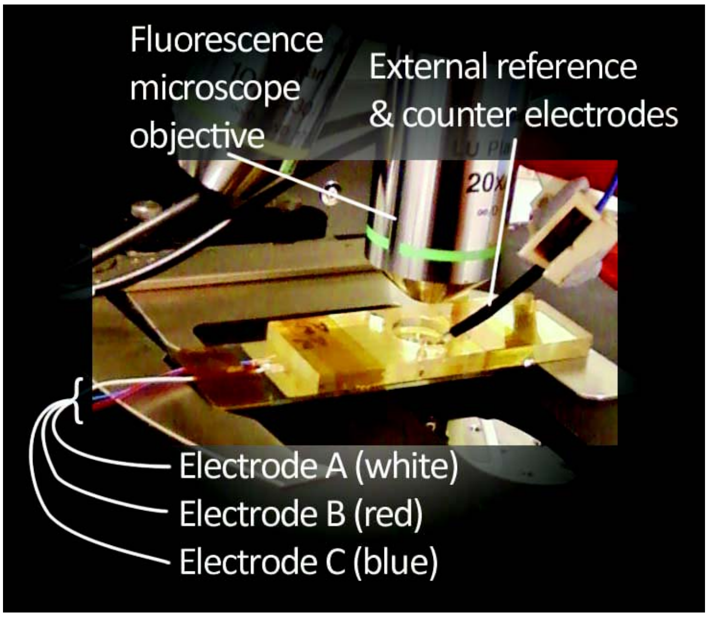

**Figure 7.3:** An image demonstrating the configuration of microscope and electrode used to acquire simultaneous optical and amperometric data. The functionalised array was secured in place by attaching the rig to a glass slide and placing this on the microscope stage. The wires attached to the array were also affixed to the microscope slide to provide additional stability, reducing the risk of a wire loosening from the array contacts. The reference and counter electrodes were clamped in place once in position.

## 7.3 Results

### 7.3.1 Assessment of G1 electrode arrays

Immediately upon receipt, a G1 array was functionalised as described above after through rinsing with DI water. No current changes were observed from any of the 7 electrodes of the array following xanthine/XOD calibration (tested XOD concentrations ranged from 20 Uml$^{-1}$ to 0.5 µUml$^{-1}$). CV investigation of an untreated new array demonstrated a lack of surface electron transfer to the probe solution while microscopic observation revealed extensive surface contamination.

To assess the plausibility of cleaning arrays prior to functionalisation, CV using potassium ferricyanide ($Fe^{3+/2+}(CN)_6$) was carried out both before and immediately after a standard electrolytic cleaning cycle. Images were taken of the electrodes after each stage to identify any visible damage. CV data highlighted increase electron transfer to the probe solution in some electrodes post-clean (Figure 7.6). Standard electrolytic stripping and UV-ozone cleaning procedures resulted in the delamination of gold from the polyester slide in most electrodes however, with some becoming completely destroyed (Figure 7.4). 3 electrodes were severely contaminated with a clear substance that coated the entire well as shown in Figure 7.5.

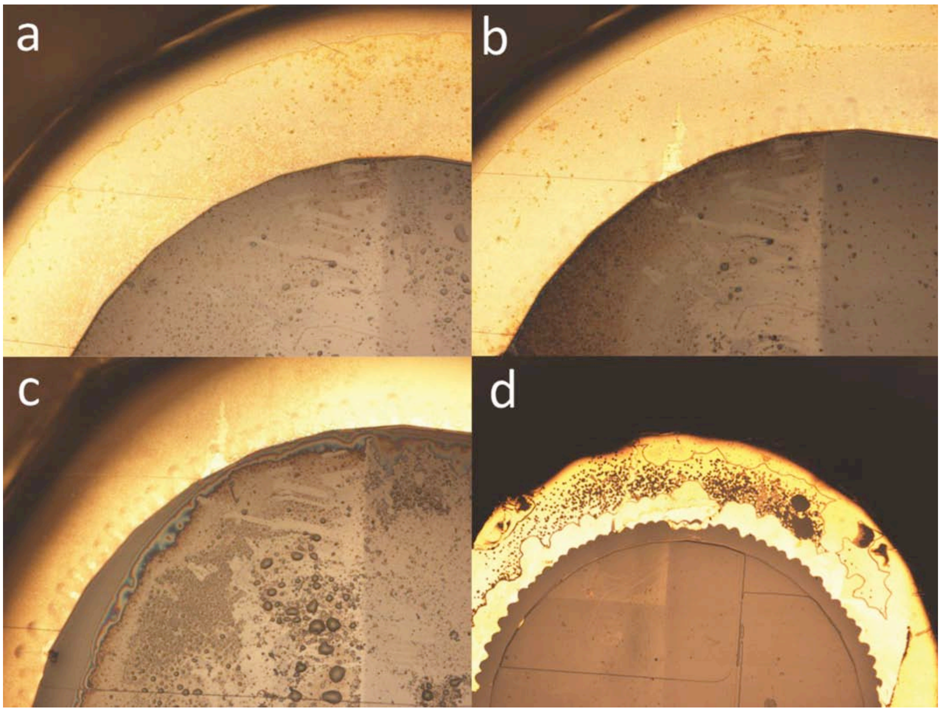

**Figure 7.4:** Observation of progressive damage to the array ring electrodes following cleaning and CV analysis. Images a, b and c were captured from a single electrode in a G1 array following one cycle of CV prior to cleaning (a) immediately after electrolytic cleaning (b) and after a second cycle of CV (c). Pitting was observed after the first CV, with delamination of the ring electrodes inner perimeter is visible as subtle fluting in image b. This became more pronounced in image c. Some electrodes were completely destroyed before the process was completed (d).

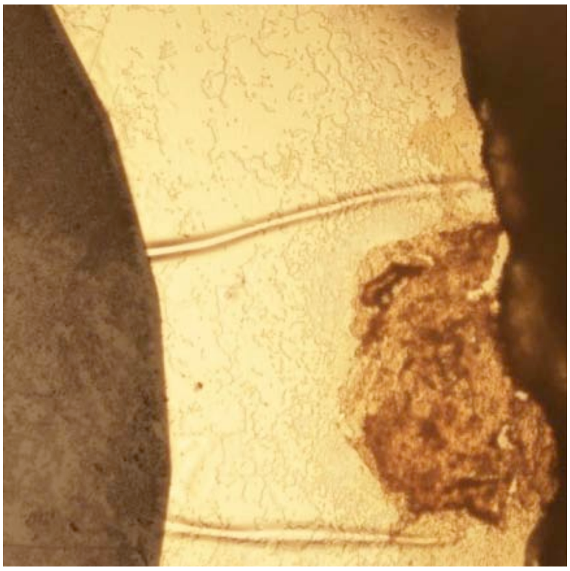

**Figure 7.5:** Bright-field microscopic observation of the G1 electrode arrays revealed extensive contamination of the wells. In this well, a clear substance covered the entire electrode and aperture. The brown patch and irregularly shaped well wall further suggested well contamination. Repeated rinsing, electrolytic cleaning or UV-zone cleaning procedures could remove neither the brown substance nor the clear coating.

In light of the damage caused by electrolytic stripping UV-ozone cleaning was tested as an alternative method. CV using potassium ferricyanide ($Fe^{3+/2+}(CN)_6$) was again carried out both before and immediately after a standard cleaning cycle. Most electrodes survived this process and exhibited a marked increase in surface electron transfer after the cleaning cycle. Microscopic observation of the arrays showed no visible damage however the substance coating the electrodes as shown in Figure 7.5 could not be removed with either UV-ozone cleaning or electrolytic stripping.

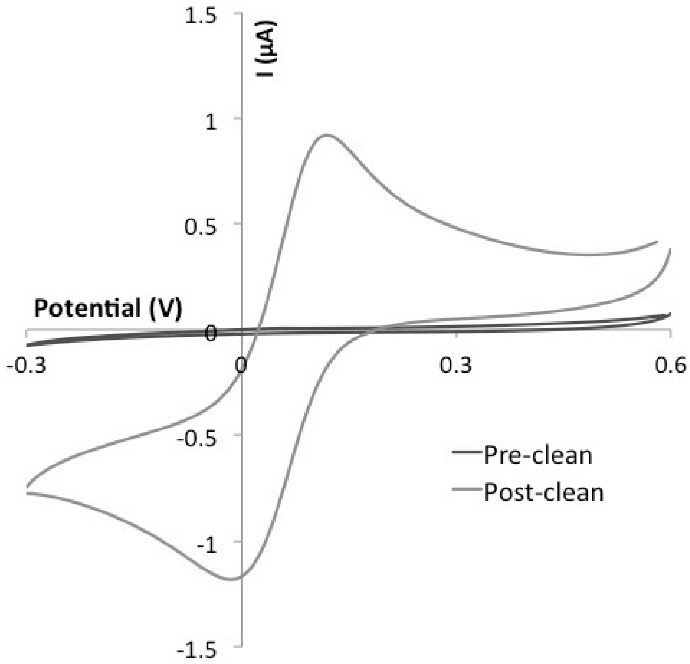

**Figure 7.6:** CV traces achieved from the G1 electrodes both before and after successful UV-ozone cleaning revealed that electron transfer to the probe solution was completely inhibited before the cleaning stage and was significantly increased afterward. This process visibly damaged most of the electrodes meaning post-clean CV sweeps could not be achieved for every well in the G1 arrays. Electrodes that appeared physically intact following the process were then functionalised with cytochrome *c*.

Electrodes that were not visibly damaged and produced an increase in electron transfer following UV-ozone cleaning were functionalised as described in section 7.2.2. Out of 21 electrodes over 3 arrays, 11 electrodes remained intact following cleaning, with 3 of the non-damaged electrodes exhibiting immovable contamination.

The generation of $O_2^-$ by enzymatic conversion of xanthine to uric acid by XOD has previously been used to calibrate the $O_2^-$ response of cytochrome *c*-functionalised gold electrodes and also detailed in Chapters 5 and 6. The current change in response to the enzymatic generation of $O_2^-$ was highly variable between electrodes. Of the remaining 7 electrodes, 3 were responsive to $O_2^-$ following functionalisation. Figure 7.7 shows 3 respective traces generated by the responsive electrodes. The traces exhibit very low signal to noise ratios, making data interpretation difficult and inferred very low signal resolution to the electrodes. The average maximum response to 1 Uml$^{-1}$ XOD in substrate-saturated conditions was 2.027 nA (± 0.321). Higher concentrations of XOD did not elicit higher responses. No signal was observed with the addition of 0.5 or 0.1 Uml$^{-1}$.

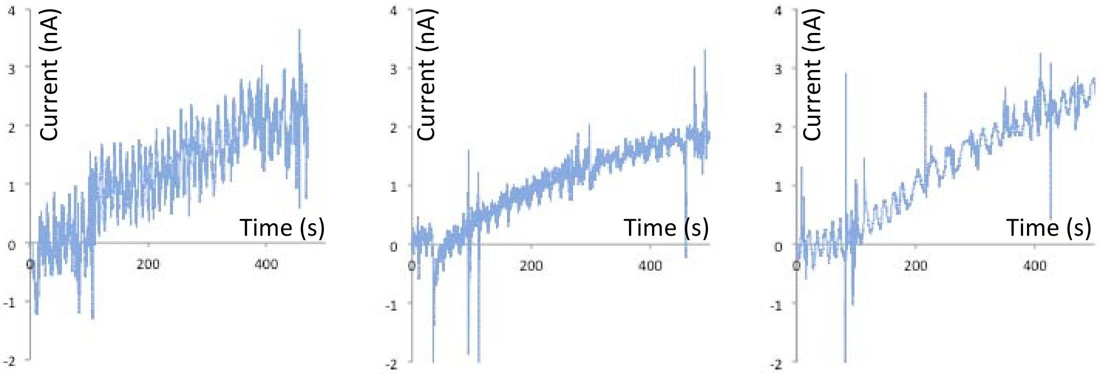

The low signal to noise ratio of the signals reduced the resolution of the electrode to report subtle differences in $O_2^-$ generation.

### 7.3.2 Enzymatic calibration of G2 electrode

The G2 electrodes did not require electrolytic or UV-ozone cleaning prior to use. Following removal of the protective photoresist layer, CV analysis of the electrodes revealed excellent electron transfer properties (Figure 7.8). Subsequent surface functionalization permitted the construction of a XOD dose response curve. The G2 electrodes displayed extreme sensitivity to $O_2^-$ generated by the XOD/xanthine decomposition; concentrations as low as 0.5 µUml$^{-1}$ generated determinable current response increases. The array electrode responses were examined using the enzymatic reaction between XOD with its substrate, xanthine, under conditions of substrate saturation to generate $O_2^-$. The change in current was observed as a function enzyme concentration. The electrode response was shown to be dependent upon XOD concentration and therefore proportional to the amount of $O_2^-$ generated. Calibration data presented in Figure 7.9 are in keeping with those reported previously (Cooper *et al*. 1993; Manning *et al*. 1998).

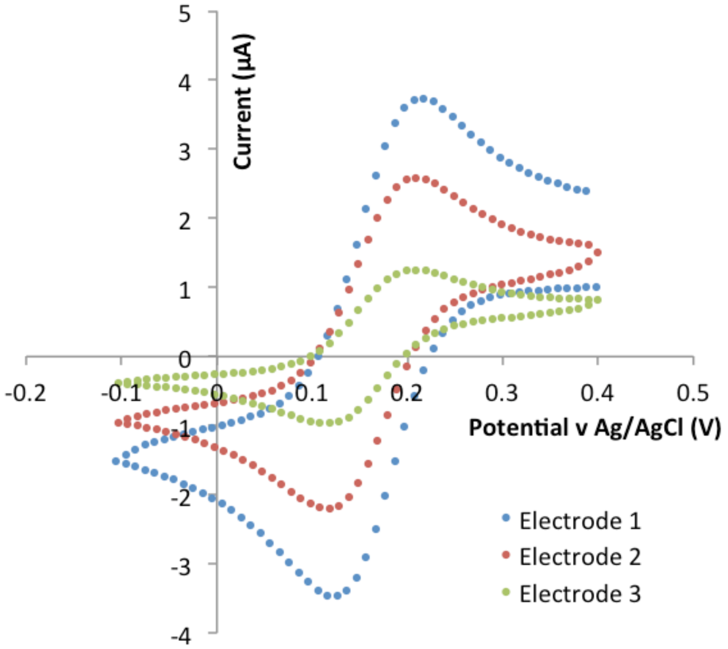

**Figure 7.8:** CV analysis of the G2 electrodes following removal of the protective photoresist layer. The electrode-patterned slide was sonicated in acetone, rinsed with isopropanol then finally rinsed with deionised water. Following assembly into a finished electrode CV was undertaken using 1mM ferrocenedimethanol in 100mM phosphate buffer. Good surface electron transfer properties were observed for all electrodes, indicating the electrodes were free from surface contamination.

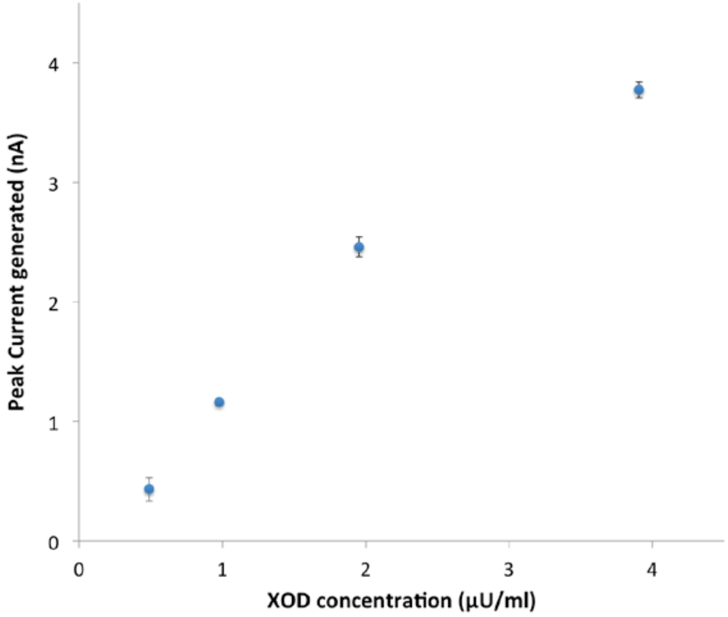

**Figure 7.9**: Calibration of the G2 array electrodes by recording the maximum current responses elicited by various concentrations of XOD in 10mM xanthine. The observed current is dependent on the enzyme concentration. The values presented are ±SEM, n=2.

### 7.3.3 Independent amperometric monitoring of cellular $O_2^-$ flux

Prior to integrating optical and amperometric measurement protocols the ability of the array electrodes to sense extracellular $O_2^-$ flux elicited by PMA stimulation of the macrophage cells was assessed. A dose response curve was constructed by stimulating populations of nanosensor loaded macrophage cells with varying concentrations of PMA and recording the peak current response generated. The current response value for each concentration challenge was taken 10 s after addition to avoid pipetting artefacts observed when PMA was added to a well containing no cells. The data from combined traces from differently stimulated cells demonstrated that the peak current response generated was linearly dependent upon PMA concentration (y=0.1841x+0.1675, r=0.9925, n=3)

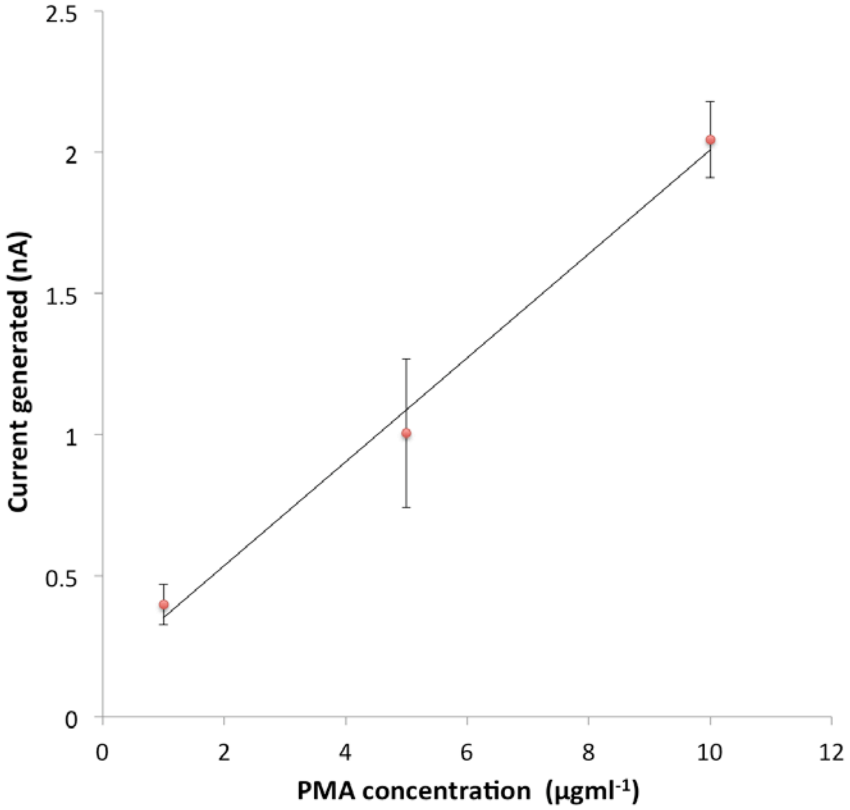

**Figure 7.10:** The maximum current generated by nanosensor loaded NR8383 macrophage cells in response to PMA stimulation was monitored with the G2 electrode array and plotted as a dose response curve. Cells were not monitored optically during experimentation. The data is presented ±SD, n=2.

### 7.3.4 Independent optical monitoring of intracellular ROS generation

Prior to integrating amperometric and optical monitoring systems, the ability to make optical measurements from within the array wells was assessed using ROS-sensitive nanosensor doped rat macrophage NR8383 cells. It was discovered that the polyester of the base slide was brightly fluorescent when viewed with the B-2E/C filter block that is used to observe DHR123. Nanosensor loaded cells were visible if they lay on top of the electrode surface but the background auto-fluorescence of the aperture was too high to allow meaningful FI measurements to be taken. Figure 7.11 displays images captured of nanosensor-doped cells within a G2 array well. When viewed with the B-2E/C filter the aperture is highly fluorescent, however no auto-fluorescence was observed with the CY3 filter. Cells resting directly upon the surface of the electrode were clearly visible.

In light of the arrays auto-fluorescence, only cells resting directly upon the electrode were included in the regions of interest optically monitored. Following treatment with 10µM PMA a 2.8 fold increase in mean FI ratio (DHR123/Alexafluor568) was observed (see 12). This is in keeping with the results shown in Chapter 3. The background fluorescence was too high and variable to allow measurements to be taken from cells resting on the aperture.

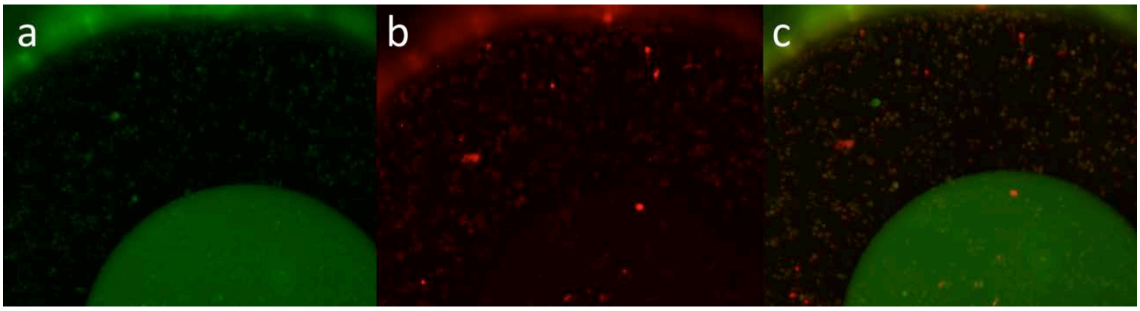

**7.11:** Nanosensor loaded NR8383 cells resting on the bottom of an array well as viewed using the B-2E/C filter (a) the CY3 filter (b) and merged (c). In image a, the auto-fluorescent aperture masks the fluorescence of the sensor loaded cells, however these can be observed clearly when resting on the electrode. There is no such interference when using the CY3 filter as shown in image b. Co-localisation of the DHR123 (a) and AlexaFluor568 (b) fluorescence is shown in image c.

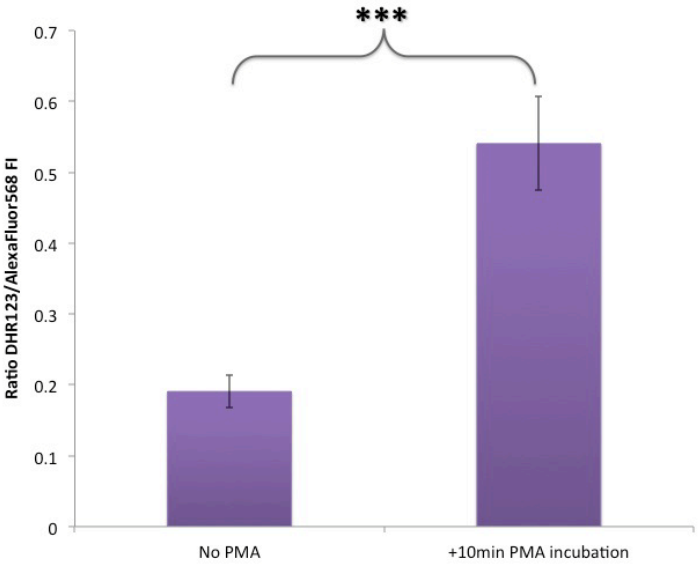

**7.12:** ROS sensitive nanosensor-doped NR8383 cells exhibited an increase in FI ratio (DHR123/AlexaFluor568) following treatment with 10 µM PMA. The data is presented ±SEM, n=5.

### 7.3.5 Simultaneous intra- and extracellular monitoring of ROS

Optical measurement of intracellular ROS generation was achieved simultaneously with the amperometric monitoring of extracellular $O_2^-$ flux following PMA stimulation. Two different concentrations of PMA were tested. ROS-sensitive nanosensor loaded cells were placed into a well on a G2 electrode array and monitored extracellularly using the functionalised ring electrode at the well's base whilst periodic optical measurements of the same cells were performed from above the array using a fluorescence microscope. Figures 7.13 and 7.14 display both optical and amperometric data for cells treated with 1 µgml$^{-1}$ and 5 µgml$^{-1}$ respectively.

The amperometric data recorded from both PMA challenges demonstrated an immediate sharp increase in current response followed by a gradual and steady increase over the remainder of the time course. Treatment with 5 µgml$^{-1}$ PMA elicited a greater rate of current change (67 pA min$^{-1}$) from the macrophage cells than the lower 1 µgml$^{-1}$ challenge (42 pA min$^{-1}$).

Optical data also demonstrated a rapid increase in FI ratio corresponding to an increase in ROS generation within the cells. Although both the 5 and 1 µgml$^{-1}$ challenges elicited nearly a 2-fold initial increase in FI ratio, the 5 µgml$^{-1}$ challenge resulted in a sustained average ratio increase of approximately 0.944 (±0.041) whereas the 1 µgml$^{-1}$ challenge resulted in a sustained average ratio following the initial peak of 0.787 (±0.003).

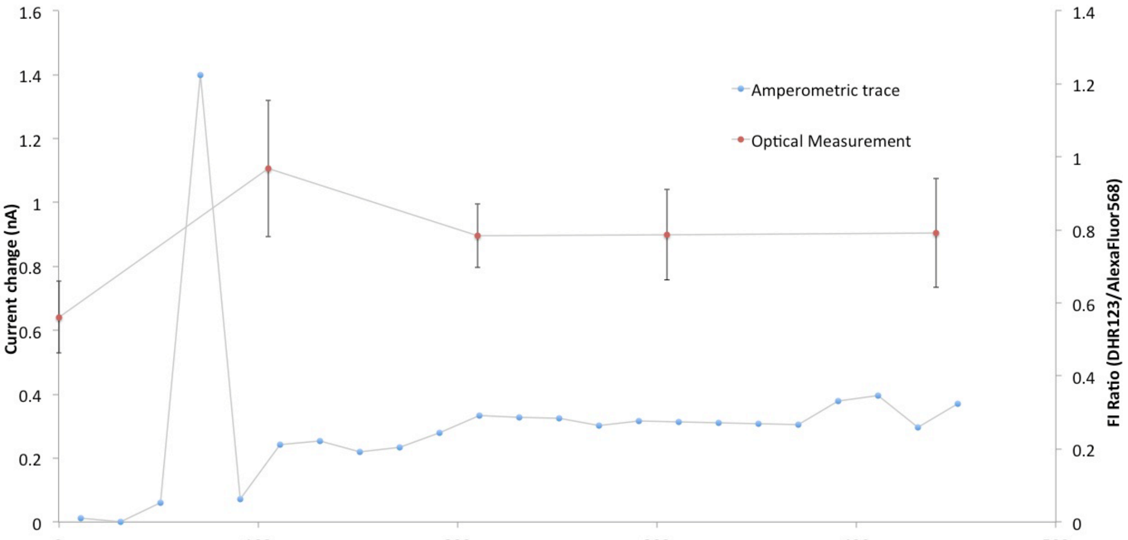

**Figure 7.13:** Simultaneous intra- and extracellular monitoring of ROS generation and flux from NR8383 cells during 1 µgml$^{-1}$ PMA treatment. Optical measurements were made periodically with a fluorescence microscope whilst amperometric monitoring ran continuously. The optical data is presented ± SEM, n=3, the amperometric trace is representative of the time period relative to the acquisition of optical data. The amperometric data plotted is representative of point averaging (±1 s) every 20 s.

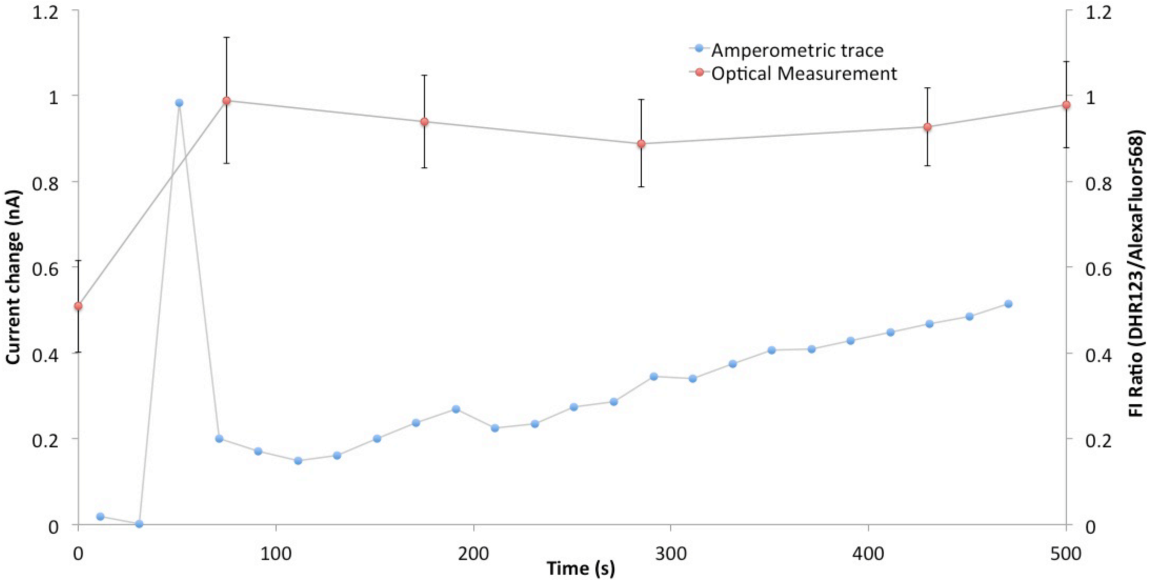

**Figure 7.14:** Simultaneous intra and extracellular monitoring of ROS generation and flux from NR8383 cells during 5 µgml$^{-1}$ PMA treatment. Optical measurements were made periodically with a fluorescence microscope whilst amperometric monitoring ran continuously throughout the entire experiment. The optical data is presented ± SEM, n=3, the amperometric trace is representative of the time period relative to the acquisition of optical data. The amperometric data plotted is representative of point averaging (±1 s) every 20 s.

## 7.4 Discussion

The overall aim for this PhD project was to integrate the optical nanosensor based monitoring system discussed in Chapters 3 and 4 with the amperometric superoxide sensors used in Chapters 5 and 6. The resulting platform allowed real-time monitoring of $O_2^-$ flux both within and released by PMA-stimulated rat macrophage cell line NR8383. This cell model was also used during the optimisation of the ROS sensitive nanosensors in Chapter 3 as the ROS generation capabilities of such phagocytes have been well reported (Craig *et al*. 2009; Henderson *et al*. 2009; Mukbel *et al*. 2007).

The gold disc electrodes used in Chapters 5 and 6 to monitor $O_2^-$ flux from isolated mitochondria were too large and spatially incompatible to be used in conjunction with the fluorescence microscope. A microscope slide-like cartridge of arrayed wells containing isolated ring electrodes at their bases had been proposed as a more compatible conformation. Over the course of the study, 2 different cartridges were tested; the first generation (G1) containing a 7-electrode array and the second generation (G2) containing a 3-electrode array. Unlike the G2 arrays, which have been integrated with optical measurement protocols, G1 arrays were presented as ready-to-use, fully assembled cartridges with the electrode containing and well forming slides assembled into a single unit. Unfortunately the gold surface was not cleaned following laser etching to define the electrodes nor protected from environmental contamination thereafter, which subsequently lead to difficulty covalently immobilising cytochrome *c* on the ring electrode surface. Attempts to clean the gold surface prior to functionalization lead to delamination and electrode damage. This resulted in the redesign and repackaging of the G2 electrodes to include protecting the newly fabricated electrodes with a layer of photoresist to prevent surface contamination and to reduce the risk of physical damage.

The G2 arrays contained only 3 electrodes in comparison to 7 in the G1 arrays, permitting an increase in well volume and electrode surface area. The width of the exposed ring electrode was increased from 200µm to 500µm, resulting in the electrode surface area becoming 3.14 times larger per well. The aperture size remained unchanged. Very small current changes were observed in response to enzymatically generated $O_2^-$ from the G1 electrodes that had survived UV-ozone cleaning and had been successfully functionalised. The signal to noise ratio of the observed traces was very low, masking subtle current changes elicited by relatively low $O_2^-$ generation. The larger surface area of the G2 electrodes was designed to improve trace clarity and increase sensitivity by increasing the signal to noise ratio by providing a greater surface area available for cytochrome *c* immobilisation.

Prior to full integration the G2 electrodes were calibrated using the same XOD/xanthine $O_2^-$ generating system described in Chapters 5 and 6 to ensure current changes could be observed from the arrays in response to $O_2^-$ generation. Following the successful amperometric monitoring of enzymatically generated $O_2^-$, rat alveolar macrophage cells were placed in the array wells and treated with PMA as described in Chapter 3. The $O_2^-$ burst elicited by PKC stimulation and subsequent progressive $O_2^-$ flux was recorded using the array electrodes. The optical properties of the array were also checked prior to integration. The nanosensors selected for monitoring ROS generation in the macrophage cells comprised the ROS sensitive dye DHR123 and stable reference dye AlexaFluor568 entrapped within a polyacrylamide matrix. These nanosensors were characterised and described at length in Chapter 3. Measurement of the FI of the internalised nanosensors was achieved using a fluorescence microscope with 2 filter blocks to independently image DHR123 and AlexaFluor568.

During the optical feasibility studies, it was discovered that the gold spluttered base slide was auto-fluorescent, meaning that the cells resting on the aperture could not be observed optically due to the high background FI of the array. The microscope used in this study was not inverted, as the array was originally designed for, and thus it was still possible to observe cells resting upon the electrodes surface. Monitoring the cells from above also presented another unforeseen artefact. When light was allowed to fall on the electrodes through either the B-2E/C or CY3 filter block, an instant large increase in current was observed which was sustained for the duration of exposure, then immediately returned to baseline upon closing the microscope shutter. The dynamics of the current increase were highly reproducible and thus could be subtracted from the trace as an artefact without skewing the $O_2^-$ current changes recorded. To investigate this anomaly further, both a functionalised and bare array was placed under the microscope, flooded with phosphate buffer and exposed to light through both the B-2E/C and CY3 filter. The functionalised array generated current changes as previously observed, however the bare array did not. The current change was repeatedly larger with B-2E/C exposure compared with CY3. B-2E/C filtered light exposure resulted in a current increase of 0.610nA (SEM=0.0772 nA, n=5), whilst CY3 filtered light exposure resulted in a change of 0.365nA (SEM=0.0769, n=5). This current change may be a consequence of photo-excited electrons within cytochrome *c* becoming mobilised due to the potential applied to the working electrode.

To avoid these problems in future investigations, an inverted microscope should be employed for optical measurements to avoid light falling directly on the immobilised cytochrome *c*. In order to use the arrays with an inverted microscope however the arrays must be reconfigured to incorporate a non-auto-fluorescent material such as glass to allow viewing of the cells through the electrode aperture. A glass base slide would also allow soldering of the gold contacts to the wires used to patch the array to the potentiostat. The silver doped epoxy resin was prone to breaking from the surface of the contact pad, making the arrays very fragile. Soldering would provide a stronger bond between electrode and wire, making the arrays more robust. Chang and co-workers reported successful fluorescence monitoring though polycarbonate-based electrode arrays using an inverted microscope (Chang *et al*. 2005), this material could also be used as an alternative electrode substrate.

The feasibility studies regarding nanosensor measurement from within the arrays displayed a much lower FI ratio values than the optical measurements taken during the simultaneous experiments. Retrospectively comparing the two sets of images showed that there was a higher amount of debris in the feasibility studies that increased the FI value calculated for AlexaFluor568. Cell debris was problematic while monitoring cells during the simultaneous measurements, resulting in higher SEM values than were expected. The arrays were too tall to permit using objectives of power higher than x10. The distance from the top of the array to the bottom of the wells is greater than the focal distance of the objective. This resulted in the acquisition of images over a large area of the electrodes rather than honing in on a discreet population of cells as was done in previously reported studies (Chang *et al*. 2005; Henderson *et al*. 2009). Despite the definition of very specific regions of interest, small auto-fluorescing particles of debris still had an impact on the FI measurements acquired for both dyes, especially AlexaFluor568. This could be avoided by using a confocal microscope to take discreet z-slice images of the nanosensor loaded cells, reducing the chance of measuring small particles of debris resting on the base of the well.

Despite these unforeseen difficulties and anomalies, integration of ROS-sensitive nanosensor technology with an amperometric $O_2^-$ monitoring system was still achieved. Amperometric traces achieved from the array electrodes demonstrated excellent sensitivity to enzymatically generated $O_2^-$ and displayed the characteristic shape of classic PMA stimulated $O_2^-$ flux as previously reported (Chang *et al*, 2005; Henderson *et al*, 2009). Only two different concentrations of PMA were tested using the integrated platform, however the preliminary data suggests that both generated current and FI ratio are both concentration dependent. An increase of 25 pAmin$^{-1}$ was observed in the rate of current change between cells treated with 1µgml$^{-1}$ and 5µgml$^{-1}$ PMA, whilst the observed sustained FI ratio post-PMA exposure was 20% higher in cells treated with 5µgml$^{-1}$ compared with 1µgml$^{-1}$.

The simultaneous measurements achieved from the arrays represent a very preliminary study regarding the integration of optical nanosensor technology and amperometric biosensing systems, however it is the first step of a continuing line of research. Although the arrays are not ideal for purpose, there is much work that still needs to be done to fully characterise them. Monitoring the cells over a longer time period and examining the responses observed to a wider range of stimuli concentration will give good insight regarding the monitoring capabilities of this particular array configuration before optimising the spatial conformation and manufacturing materials for the next generation of platforms for simultaneous intra- and extracellular monitoring.

## 7.5 References

Boulton, S., Anderson, A., Swalwell, H., Henderson, J.R., Manning, P., Birch-Machin, M.A., 2011. Implications of using the fluorescent probes, dihydrorhodamine 123 and 2',7'-dichlorodihydrofluorescein diacetate, for the detection of UVA-induced reactive oxygen species. Free Radical Research 45(2), 139-146.

Chang, S.C., Rodrigues, N.P., Zurgil, N., Henderson, J.R., Bedioui, F., McNeil, C.J., Deutsch, M., 2005. Simultaneous intra- and extracellular superoxide monitoring using an integrated optical and electrochemical sensor system. Biochemical & Biophysical Research Communications 327(4), 979-984.

Chen, X., Zhong, Z., Xu, Z., Chen, L., Wang, Y., 2010. 2',7'-Dichlorodihydrofluorescein as a fluorescent probe for reactive oxygen species measurement: Forty years of application and controversy. Free Radical Research 44(6), 587-604.

Clark, H.A., Hoyer, M., Philbert, M.A., Kopelman, R., 1999. Optical nanosensors for chemical analysis inside single living cells. 1. Fabrication, characterization, and methods for intracellular delivery of PEBBLE sensors. Analytical Chemistry 71(21), 4831-4836.

Cooper, J.M., Greenough, K.R., McNeil, C.J., 1993. Direct electron transfer reactions between immobilised cytochrome *c* and modified gold electrodes. Journal of Electroanalytical Chemistry 347(1-2), 267-275.

Craig, M., Slauch, J.M., Craig, M., Slauch, J.M., 2009. Phagocytic superoxide specifically damages an extracytoplasmic target to inhibit or kill Salmonella. PLoS ONE 4(3), e4975.

Di Matteo, V., Pierucci, M., Benigno, A., Crescimanno, G., Esposito, E., 2009. Involvement of nitric oxide in nigrostriatal dopaminergic system degeneration: a neurochemical study. Annals of the New York Academy of Sciences 1155, 309-315.

Henderson, J.R., Fulton, D.A., McNeil, C.J., Manning, P., Henderson, J.R., Fulton, D.A., McNeil, C.J., Manning, P., 2009. The development and *in vitro* characterisation of an intracellular nanosensor responsive to reactive oxygen species. Biosensors & Bioelectronics 24(12), 3608-3614.

Kundu, S., Bala, A., Ghosh, P., Mukhopadhyay, D., Mitra, A., Sarkar, A., Bauri, A.K., Ghosh, A., Chattopadhyay, S., Chatterjee, M., 2011. Attenuation of oxidative stress by allylpyrocatechol in synovial cellular infiltrate of patients with Rheumatoid Arthritis. Free Radical Research 45(5), 518-526.

Manning, P., McNeil, C.J., Cooper, J.M., Hillhouse, E.W., 1998. Direct, real-time sensing of free radical production by activated human glioblastoma cells. Free Radical Biology & Medicine 24(7-8), 1304-1309.

Mukbel, R.M., Patten, C., Jr., Gibson, K., Ghosh, M., Petersen, C., Jones, D.E., 2007. Macrophage killing of Leishmania amazonensis amastigotes requires both nitric oxide and superoxide. American Journal of Tropical Medicine & Hygiene 76(4), 669-675.

Olivetta, E., Mallozzi, C., Ruggieri, V., Pietraforte, D., Federico, M., Sanchez, M., 2009. HIV-1 Nef induces p47$^{phox}$ phosphorylation leading to a rapid superoxide anion release from the U937 human monoblastic cell line. Journal of Cellular Biochemistry 106(5), 812-822.

Panov, A., Kubalik, N., Zinchenko, N., Hemendinger, R., Dikalov, S., Bonkovsky, H.L., 2011. Respiration and ROS production in brain and spinal cord mitochondria of transgenic rats with mutant G93a Cu/Zn-superoxide dismutase gene. Neurobiology of Disease 44(1), 53-62.

# Chapter 8. General conclusions and future work

## 8.1 Conclusions

The ultimate aim of this PhD research was to develop a fully integrated ROS-sensing platform that allowed simultaneous interrogation of both the cytoplasm and extracellular environment of cell models of disease. The integration of the optical nanosensor and amperometric technologies has been achieved and preliminary simultaneous data have been recorded in terms of intra and extracellular ROS production by rat alveolar NR8383 macrophages. Although the data reported within this thesis is representative of very preliminary application of the integrated platform to only one model of ROS-responsive cellular systems, strong proof of concept has been obtained that future investigations can build upon this work.

In terms of the extracellular electrical monitoring system employed thoughout this research, important realisations regarding the proper implementation of such techniques were made. Initially all work was carried out using a 2 electrode system whereby the Ag/AgCl reference electrode functioned as both reference and counter electrodes. This was the standard chronoamperometric set up for $O_2^-$ analysis within the group when the research project began. Although it was possible to achieve some reliable data from the system (see chapter 5 and Henderson et al, 2009) many problems regarding the quality of data recorded using the 2-electrode system such as heavily drifting baselines, very low signal to noise ratios and inverse responses were observed. To avoid wasting time and consumables on an unreliable system, we moved to use a 3-electrode set up. This new conformation comprised an independent counter electrode in conjuction with the reference and working electrodes. Using this conformation of electrodes stabilised the circuit and protected the reference electrode from carrying any current, improving the clarity of the traces recorded, reducing noise and allowing the reproducible acquisition of meaningful data (See Chapter 6). This protocol is now the standard operating procedure for $O_2^-$ monitoring within the group.

Unforeseen difficulties regarding simultaneous intra- and extra-cellular measurement were encountered such as the auto-fluorescence of the electrode array apertures and the current enhancing affect of light upon the functionalised gold electrode however, there are simple changes to the data recording methodology and to the array fabrication procedures that could provide improved data resolution and accuracy. By using a glass substrate in place of the polyester slide the array electrodes were defined upon no auto-fluorescence would be observed from the array aperture. This would allow observation of nanosensor loaded cells with an inverted microscope which in turn prevents exposure of the functionalised side of the ring electrodes to excitation light, reducing the risk of amperometric data disturbance during acquisition. The data presented in Chapters 3, 4 and 7 of this thesis represent the first ratiometric measurements reported from polyacrylamide ‘PEBBLE’ nanosensors. Thus far, meaningful ratiometric measurements have not been reported from within cells, with only the change in the FI of the nanosensor sensing dye (Henderson *et al*. 2009) or simply monitoring fluorescence to record only the intracellular location of delivered nanosensors (Coupland *et al*. 2009) being reported. The use of NR8383 macrophage cells as a model of cellular ROS generation provided a well-characterised and reproducible vehicle to prove the viability of the both the nanosensors and the electrochemical array as components of the prospective final integrated platform. The model, however, was self-limiting since phagocytosis is a highly specialised process generally only observed in the macrophage, neutrophil and dendritic cells of the immune system. Characterisation of the platform with non-phagocytic cells in other disease models would add a great deal of value to the system by broadening the range of potential applications for example, simultaneous monitoring of intra and extracellular ROS generation in cardiac myocytes could provide a platform to investigate ROS flux during hypoxic reperfusion, allowing greater understanding of the mechanism of oxidative damage in the heart. The integrated optical-electrochemical platform, once more fully characterised, represents a unique opportunity for scaling-up to a high throughput, high content system for testing a range of chemicals of potential therapeutic benefit in terms of their real-time effects upon the flux of ROS both intra- and extracellularly. The work described in Chapter 4, although not directly related to ROS monitoring, demonstrated that optical nanosensors could be used to report intracellular changes in an analyte of interest from non-phagocytic cells. The integration of pH nanosensors with extracellular $O_2^-$ measurement could prove to be a useful tool for the investigation of age-related muscular deterioration where both acidosis and increased ROS generation are key to disease progression. In Diabetes Mellitus, oxidative stress has been implicated in the progression of disease state as ROS signalling activates a number of stress pathways activating serine/threonine kinase family and ultimately reducing insulin signalling (Rains and Jain, 2011). Lactic acidosis is a dangerous biomarker of a severe disease state, linked to metabolic stress within the muscle tissue. It has been proposed that tight control of hyperglycaemic episodes through diet may reduce the overproduction of ROS, reducing insulin resistance and promoting the clearing of lactic acid in muscle (Evans *et al*, 2003). One particularly interesting mechanism behind hyperglycaemia-induced ROS production is underpinned by a high volume of substrate entering the TCA during hyperglycaemic episodes. Once the membrane voltage limit is reached by the large number of electrons being donated to the mETC, electrons back up behind the rate limiting Complex III, in essence causing a similar flux of electrons as is observed through inhibition of the mETC by agents such as rotenone, antimycin and TaClo, leading to the uncontrolled production of $O_2^-$ (Brownlee, 2001). The integrated platform could be used to investigate on a cellular level the relationship between cell pH and ROS flux in a dynamic, real-time and meaningful manner. With this in mind, characterising the array using pH-sensitive nanosensors and extracellular ROS sensing electrodes could provide a platform to evaluate the effects of potential therapeutics for metabolic disorder upon muscle cell oxidative state and internal pH. A platform of this kind may also be of benefit to the identification and development of novel therapeutic agents by being utilised to preclude animal-based studies as this is one of the cornerstones of NC3Rs research initiatives throughout the UK and indeed Europe (see e.g. www.nc3rs.org.uk).

## 8.2 Future Work

Many avenues for future investigation were opened due to the application driven nature of this project and the diverse collaborations that allowed the reported studies to be achieved. Further characterisation of the polyacrylamide nanosensors both pH and ROS-sensitive will allow a robust method of intracellular monitoring to be routinely employed. Investigation of the temporal limits of nanosensor based analyte sensing could potentially allow multi-generational reporting of intracellular dynamics. It is currently unknown how long the nanosensors remain functionally useful following internalisation. If the encapsulated dyes are protected from intracellular degradation by the polyacrylamide matrix the nanosensor may remain ‘viable’ indefinitely, limited only by dye autooxidation, photolysis or a relative drop in intracellular nanosensor concentration as cells proliferate. Work regarding the characterisation of both ROS-responsive and pH-responsive intracellular nanosensors and the integrated optical-electrical sensing platform is currently ongoing. Further investigation regarding the optimisation of intracellular delivery of polyacrylamide nanosensors will also be carried out. It is hoped that future work will enable the facile employment of the technology as a robust and reliable sensing technique over a wide range of clinically relevant scenarios, providing unique insight into the intricate and ubiquitous roles of ROS in living organisms.

## 8.3 References

Brownlee, M., 2001. Biology and molecular cell biology of diabetic complications. Nature 414, 813-820.

Coupland, P.G., Briddon, S.J., Aylott, J.W., 2009. Using fluorescent pH-sensitive nanosensors to report their intracellular location after Tat-mediated delivery. Integrative Biology 1(4), 318-323.

Evans J.L., Goldfine I.D., Maddux B.A., Grodsky G.M., 2003 Are oxidative stress−activated signalling pathways mediators of insulin resistance and β-cell dysfunction? Diabetes 52(1)1-8.

Henderson, J.R., Fulton, D.A., McNeil, C.J., Manning, P., 2009. The development and *in vitro* characterisation of an intracellular nanosensor responsive to reactive oxygen species. Biosensors & Bioelectronics 24(12), 3608-3614.

Rains J.L., Jain, S.K., 2011. Oxidative stress, insulin signalling and diabetes. Free Radical Biology and Medicine 50(5)567-575.